공학박사학위논문

Numerical Analysis of Supersonic Inlet Buzz Characteristics under Various Throttling and Angle of Attack Conditions

다양한 출구조건과 받음각이 적용된 초음속 흡입구 공력불안정성 수치적 연구

2013 년 2 월

서울대학교 대학원
계산과학 협동과정
홍 우 람

Numerical Analysis of Supersonic Inlet Buzz Characteristics under Various Throttling and Angle of Attack Conditions

다양한 출구조건과 받음각이 적용된 초음속 흡입구 공력불안정성 수치적 연구

지도교수 김 종 암

이 논문을 공학박사학위 논문으로 제출함
2012 년 12 월

서울대학교 대학원
기계항공공학부
홍 우 람

홍우람의 공학박사학위 논문을 인준함
2012 년 12 월

위 원 장 : _____

부위원장 : _____

위 원 : _____

위 원 : _____

위 원 : _____

Abstract

The present study numerically investigates the flow instability around supersonic inlet, called inlet buzz. Though the flow conditions change linearly, behavior of inlet buzz alters hysteretically. In order to simulate the inlet buzz hysteretic character, computations are conducted with varying mass flow rate and angle of attack. The mass flow rate condition is controlled by an exit throttling plug which moves back and forth to change an exit area. For angle of attack study, three dimensional inviscid simulations are conducted.

Firstly, a set of simulation with mass flow control is presented. This simulation focuses on hysteretic buzz characteristics of supersonic inlet according to mass flow and the historic path of the mass flow change. Before the set of simulation, an inlet without a center-body is calculated to validate basic resonance mode results. In the next, an inlet buzz case with decreasing mass flow rate is simulated. In this process, the inlet buzz characteristic changes from the first mode of a low frequency regime to the second mode of a high frequency regime. Lastly, the effect of the increasing mass flow rate on the inlet buzz is examined. This case shows another kind of the buzz transition that the buzz frequency becomes higher in the third mode. The hysteretic inlet buzz has many similarities to the fundamentals of a pipe-type musical instrument such as self-excited feed-back mechanism and overblowing. Considering the similarities, the hysteretic characteristics of an inlet buzz is discussed in the instrumental acoustic point of view.

In the second step, an investigation of angle of attack effects on inlet pressure oscillation is carried out with three-dimensional inviscid simulation intended to examine a tendency of inlet buzz briefly. It is seen that the major physical

characteristic of the inlet pressure oscillation can be obtained by inviscid computations and the computed flow patterns inside and around the inlet are qualitatively consistent with the experimental observations. It is found that patterns of pressure oscillation histories and distortion due to asymmetric (or three-dimensional) shock structures are substantially affected by angle of attack. The dominant frequency of the existing inlet pressure oscillation does not change noticeably even in regards to a wide range of angle of attacks. However, the increasing angle of attack condition initiates a pressure oscillation from a steady state of inlet at low angle of attack.

Keywords: CFD, Supersonic inlet, Inlet buzz, Shock instability, Hysteretic characteristic, Throttling control, Angle of attack, Transition

Student number: 2007-30127

Name: Hong, Wooram

Table of Contents

List of Tables

List of Figure

Chapter I
Introduction

Air-breathing engines are widely regarded as efficient and advanced propulsive systems for the supersonic flow range of Mach 2 through 12. For the ramjet engine, one of the air-breathing engines, captured air is compressed and decelerated by inlet without any compressor. Owing to its geometric simplicity, the ramjet engine can be operated in a light and efficient manner. Despite such mechanical simplicity, however, complex flow phenomena usually occur inside the engine. Around the engine inlet, shock-shock and shock-boundary interaction may cause self-excited shock oscillations, leading to severe fluctuations in the inlet mass flow rate and chamber pressure. This sequence of an unsteady process is referred to as inlet buzz, a flow oscillation that provokes a number of efficiency problems. Inlet buzz frequently causes more serious problems, such as thrust loss, engine non-starting, and even structural damage to the propulsion system. From this perspective, supersonic inlet buzz should be minimized or eliminated; however, physical understanding on some characteristic behavior of inlet buzz still remains unclear.

In order to define and control the buzz mechanism, many researchers have conducted experimental studies. The inlet buzz was first observed and described by Oswatitsch [1]. Dailey [2] found that shock-boundary interaction triggers flow separation on the compression surface, thereby giving rise to an inlet buzz, known as the Dailey-type buzz. Ferri *et al*. [3] found that the shock-shock interaction also generates an inlet buzz by creating a shear layer known as the Ferri-type buzz. Nagashima *et al*. [4] conducted an inlet buzz experiment by

controlling the throttling ratio (T.R), *such as* the area ratio between exit and inlet. Through this experimental research, many sources and behaviors of inlet buzz were identified.

Based on the earlier experimental studies, some numerical simulations were also carried out in order to understand the onset mechanism of inlet buzz. Newsome [5] simulated an inlet buzz using Nagashima's geometry [4], and Lu and Jian [6] adopted Dailey's geometry [2] for numerical simulations. Such numerical studies showed extremely unstable flow separations at the inlet upstream and a kind of feed-back mechanism of the reflected pressure waves.

1.1 Inlet Buzz Transition under Varying Mass flow condition

From previous research, the inlet buzz has been understood as an acoustic phenomenon that accompanies nearby sounds. Because the ramjet engine and pipe-type musical instrument share many similarities in terms of configuration and sounding mechanism, some researchers tried to understand the inlet buzz by simplifying the engine shape into an organ pipe or a Helmholtz resonator. Dailey carried out an experiment with an organ pipe, and Lu and Jain used the same configuration to validate their numerical results. Also, Newsome applied the theoretical acoustic formula [7] to estimate the inlet buzz frequency of Nagashima's geometry. By applying the acoustic formula onto a simpler organ pipe configuration, the fundamental mode could be predicted, and the acoustic feedback mechanism was explained in the flow condition of the low frequency buzz. The flow regime creating high frequency buzz, however, has not been actively studied yet.

Depending on the mass flow through engine, the inlet buzz shows quite disparate behaviors in spite of gradual variation of the exit mass flow condition.

As the exit nozzle area narrows to reduce mass flow rate, the frequency of the inlet buzz suddenly changes from lower to higher, or the amplitude suddenly increases from smaller to bigger. Occasionally, the two different states are referred to as low and high buzz or small and big buzz, depending on which parameter is dominant, the frequency or the amplitude.

In general, the flow condition around the inlet is stable in order to induce the critical condition in which the exit mass flow rate is large enough at the designed Mach number. After the exit mass flow rate reduces, the flow regime evolves into the sub-critical condition where shock is expelled and begins to oscillate. When the mass flow rate further decreases, the pattern of shock oscillation changes significantly, and the so-called buzz transition occurs. In Trapier's experiment [8], the buzz transition pattern changed from high frequency and small amplitude to low frequency and big amplitude. Each of them was named "small buzz" and "big buzz," and it was concluded that the small buzz occurs because of a shock-induced shear layer, and the big buzz arises from flow separation at compression surface. On the other hand, Nagashima et al. [4] observed somewhat different phenomenon and named the two states :"low buzz" and "high buzz." In his experiment with a free stream Mach number of 2, the intersection of oblique shock and normal shock was far away from the cowl lip while it was close to the cowl tip in Trapier's experiment. As a result, a shear layer from the shock intersection moved along the cowl outer surface and led to no significant effect on inlet buzz. In addition, buzz frequency for low and high buzz was different, but buzz amplitude was almost the same. From this perspective, it appears that the Nagashima's result shows a different kind of buzz transition from Trapier's experiment. Dailey [2] observed that as mass flow increases from nil, the pitch of buzz suddenly becomes almost

two times higher in octave, while the frequency generally increases (or decreases) when the mass flow decreases (or increases). Dailey briefly mentioned this anomalous phenomenon without explanation.

From the previous experimental observations, it can be concluded that the buzz character can be altered by changing the configuration or flow condition, such as the inlet design, Mach number, mass flow rate, and, in particular, the historic path of mass flow rate. These factors may result in a different buzz transition process or some anomalous behavior, such as Dailey's experimental observation on buzz excitation. A buzz with a high frequency or a big amplitude is severely detrimental to engine stability, performance, and structural safety. The hysteretic buzz character and the relevant physical mechanism under a complete cycle of mass flow operation (zero throttling to full throttling and vice versa), therefore, have to be explored in detail to attain the stability of supersonic air-breathing engine. Unfortunately, very little research has focused on the hysteretic inlet buzz character, which includes the buzz transition. Keeping this in mind, the present research aims to provide an in-depth physical understanding on hysteretic buzz characteristics under a complete cycle of throttling ratio by combining reliable, computational analyses with instrumental acoustics analogy.

A set of inlet buzz simulations were conducted using Nagashima's experimental configuration to investigate the hysteretic buzz character by fully changing the exit mass flow rate condition. For each throttling case, an FFT (Fast-Fourier Transform) analysis was conducted, and pressure histories were compared to experimental data. Furthermore, the theoretical approach exploiting acoustics of musical instrument was extended to the range of high frequency buzz.

The present paper is organized as follows: first, some basic concepts of acoustics for musical instrument are mentioned, and numerical methods and grid systems are briefly described. Then three sets of computational results are presented. In the first set of simulations, only the cowl part without center-body is considered to validate the flow solver and to examine the effect of center-body. In the second set, inlet buzz simulations with a decreasing mass flow rate (from *T.R=2.4 to T.R=0.0*) are performed. In the third set, the effects of an increasing mass flow rate (from *T.R=0.0 to T.R=2.4*) on inlet buzz are examined in detail. Finally, the three computed results are compared and discussed from the view point of instrument acoustics to explain the physical mechanism of the hysteretic buzz character, including the Dailey's experimental observation on buzz excitation.

1.2 Asymmetry Behavior of Inlet Flow Oscillation at Attack Angled flow

The supersonic inlet of the air-breathing engine under operating conditions is exposed to various throttle and angle of attack conditions. In these conditions, it is required to keep a certain quantity of mass flow rate for stable combustion. Compression and deceleration of the incoming flow to a proper Mach number should be achieved without any compressors. Around the supersonic inlet, the shockwave structure is developed by an external inflow condition and internal back pressure from the combustion chamber. This shockwave structure determines the physical properties of the captured air. As the angle of attack increases, it becomes more asymmetric and complicated.

Today's supersonic, air-breathing engine is required to perform well at high angles of attack during tactical operations; however, the axisymmetric inlet

performance deteriorates rapidly as the angle of attack increases when unfavorable factors for combustion, such as asymmetric shock structures and non-uniform pressure distribution, are generated. It is known that a serious, subsonic diffuser flow separation problem, one of the unfavorable factors for combustion, occurs at a high angle of attack. This results in poor combustor performance, and eventually the combustor blows out because of this separation [20]; therefore, to predict engine performance at a nonzero angle of attack, both internal flow characteristics and shock structures should be monitored. Earlier researchers investigated the effects of internal flow characteristics on engine performance at a moderate angle (0° ~ 9°) of attack; nevertheless, a few investigations of axisymmetric inlet buzz under the attack angled flow condition have been conducted [4, 33-35]. Common results of these investigations are that the shock structure becomes more asymmetric as attack angle increases, but the pressure oscillation frequency is almost constant. In order to understand inlet buzz behavior at the attack angled flow, it is required to investigate asymmetric flow patterns and shock structures around inlet. Inlet buzz simulation is a tough problem because of its highly unsteady physics and long-time integration. It requires large number of grids for capturing broad-range moving shock in high resolution. Trapier et al. [8] tested and analyzed the mixed-compression inlet. For the 3-D rectangular inlet simulation, the researchers used 20 million grids applied to a DES turbulence model. These are the only 3-D calculations of buzz known to the author.

In this research, 3-D inviscid simulations were conducted. Because shockwave-shockwave interactions (SWI) and shockwave-boundary layer interactions (SWBLI) are widely known as typical phenomena of supersonic inlet, they are the reasons for self-excited shock oscillation, which leads to

high amplitude variations of the inlet mass flow rate and pressure. Though the interactions do not come up in inviscid simulation, flow oscillation, which mimics inlet buzz in the fundamental mode of frequency, could be generated by narrowing the exit area. In addition, moving shock structures and basic flow patterns are captured at the angle of attack flow. It is not the same condition in reality, but some of the proofs for understanding inlet buzz behavior at angle of attack are given by computation results.

1.3 Outline of Thesis

The present paper is organized as follows: first, the fundamental background for acoustics of musical instruments is introduced, and the numerical methods and grid systems are described briefly. Then three sets of computational results are presented. In the first set of the simulations, only the cowl part without a center body is considered to validate the flow solver and to examine the effect of the center-body. In the second set, an inlet buzz simulation for a decreasing mass flow rate is performed. For the last set, the effects of an increasing mass flow rate on inlet buzz are examined. These three results are compared and discussed from an acoustical point of view.

In this research, the axisymmetric inlet buzz is simulated under various throttle and angle of attack conditions. Inviscid simulations are conducted at zero angle of attack and validated with experiment [4] and turbulent flow simulation data [25]. These validations show that both inviscid and turbulent flow simulations have a similar tendency in that the dominant frequency of pressure oscillation reduces with the increased throttle area in spite of different local flow physics and the values of some variables. In the next step, the effects of different attack angles, from 0° to 10°, are analyzed by inviscid flow calculations. From

these results, flow characteristics, such as dominant frequency, asymmetric shock structure, and behavior of external/internal flow around the inlet are dealt with the main interest of inviscid primary flow physics.

Chapter II
Instrumental Acoustics

As mentioned above, there exist many similarities between inlet buzz phenomena and the acoustics of musical instruments. In the field of wave propagation research, which is a part of classical physics, formulas for acoustic waves of the internal pipe have already been established. In order to understand various applications in instrumental acoustics relevant to the present work, some background concepts are briefly discussed [9-11].

As a typical example of a wind instrument, an organ pipe can be considered. Most wind instruments have a common energy-converting mechanism, such as the energy of steady air flow into the vibrational energy of a wind instrument. As shown in Fig. 1, the overall process of an instrument that gives rise to a sound can be roughly described as follows: a) a jet of air from a mouth or a blowing device hits the edge of the pipe; b) by hitting the edge, the non-periodic flow disturbance generates a wave that propagates into the body of the resonator and is reflected at the end of the resonator, and c) the wave feeds back into the front jet flow to change the jet direction. By repeating these steps, the disturbance is reinforced, and a periodic wave is generated. There are three key-sequences to understanding the mechanism that makes a sound.

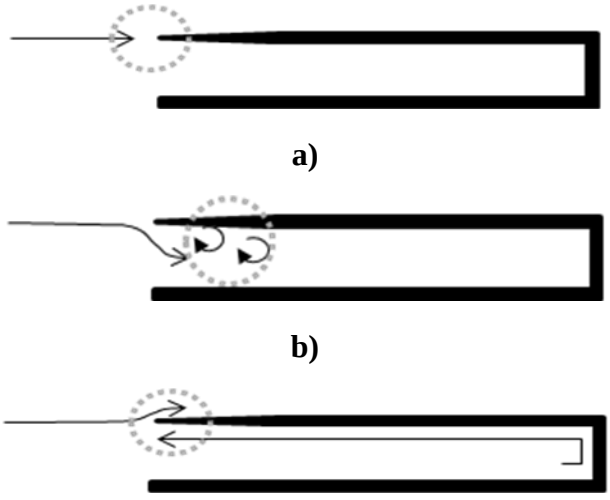

a)

b)

c)

Fig. 1 Sequence of pipe resonation. a) The front jet flow hits the edge of the pipe, b) vortices are generated around the edge, and c) the reflected wave feeds back into the jet.

2.1 Edge Tone

The source making the sound is a gap between the jet flow and the edge of the inlet, such as the flue or slit of an instrument. As the jet air blows through the pipe and the disturbance is reinforced, small vortices are formed in the air (see Fig. 2). Owing to the vortices, additional streams crossing the jet are generated at the gap, and the jet flow direction changes. The vortices induce the jet flow to run along the upper and lower surfaces of the edge repetitively in order to make a sound. It produces an extremely weak, unstable tone (or sound) whose frequency depends on the jet speed (v_j) and the length of gap(b). This tone is called an "edge tone."

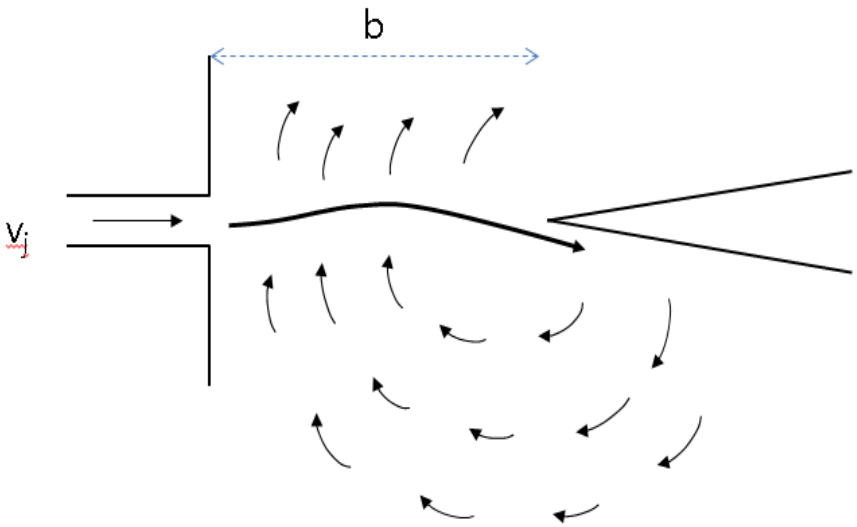

Fig. 2 Schema of edge tone mechanism

2.2 Positive feedback

The body of an instrument acts as a resonator, which amplifies certain acoustic waves (or frequencies) selectively among the wide frequency spectrum of the edge tone. The amplified frequency is determined by the body length and cross sectional area of the instrument. The edge-tone is then resonated whenever the amplified frequency closely matches the natural frequency of the resonator. For a successful resonance, a so-called positive feedback mechanism is required. For each period of a jet flow, the amplified acoustic wave is generated from the inlet edge; it travels to the closed end, reflects, and tries to push the jet back to the upstream. As a result, the reflected wave and the edge tone try synchronize in frequency. Through this process, the instrument responds more strongly to the edge tone and persuades the jet to drive at a particular frequency. Once it starts, a positive feedback mechanism is finally maintained with the particular

frequency. Although the edge tone is slightly out of tune (or frequency), the instrument still may set up a good regime of oscillations by playing a bit off its resonant peak..

2.3 Over-blowing

If the jet velocity ($v_{j)}$ is large enough or the gap (*b)* is small enough to make successive positive feedback loop, the acoustic wave becomes self-sustained and its frequency abruptly gets much higher. It can be in the second or third pipe mode. Then the jet switches its location between the above and the below of the edge more frequently, which results in a higher pitched sound. This process is called overblowing the pipe. Coltman [12] conducted organ pipe experiments, and the behavior of the blown pipe is shown in Fig. 3. In the graph, a solid straight line indicates the isolated edge tone frequency without a resonator for different jet velocities. Dash-dot straight lines show the modified edge tone when it interacts with the pipe (or the resonator). Solid curves are actual sound of the organ pipe triggered by the modified edge tone. Horizontal dot lines indicate the mode frequencies of the organ pipe (*N=1, 2, 3,…*). It makes best resonance at the intersections of the mode frequencies of the organ pipe and the modified edge tone line. At these intersections, resonance is ideal and becomes the strongest and most reliable. It is noted that the resonance frequency jumps into the next mode when the jet velocity is large enough. Also, there is an overlap zone (the gray-shaded area) in which the resonance frequency becomes double-valued for the same jet velocity. Coltman [12] observed these hysteretic double-valued characteristics experimentally and theoretically.

The mechanics described above explains the acoustic characteristics of wind instruments, such as an organ pipe.

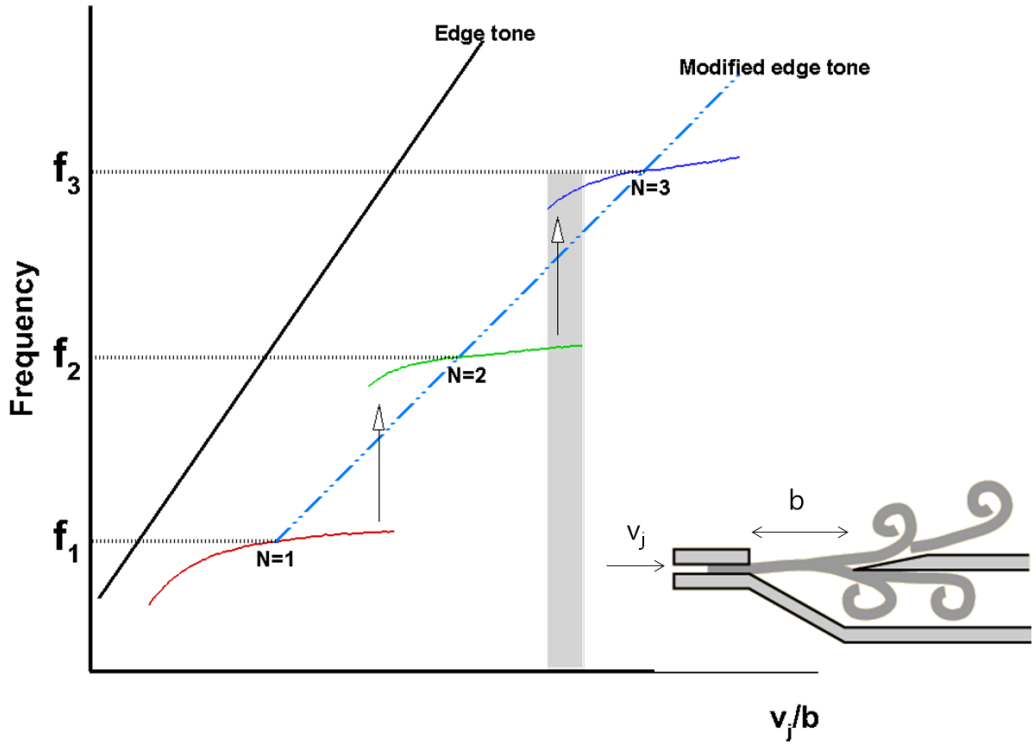

Fig. 3 Jet-edge resonant curve in organ pipe.[12]

Solid slop: Isolated edge tone frequency,

Dash-dot slop: Modified edge tone frequency coupled with organ pipe,

Horizontal dot line: Modes frequencies of the pipe alone,

Solid curves: Behaviors of blown pipe,

Gray zone: double-valued range

Chapter III
Numerical Approach

3.1 Governing Equations

The governing equation is the three-dimensional compressible Navier-Stokes equation, which can be written in a conservative law form as follows:

$$\frac{d\rho}{dt}+\frac{\partial}{\partial x_k}(\rho u_k)=0 \tag{3.1}$$

$$\frac{\partial}{\partial t}(\rho u_i)+\frac{\partial}{\partial x_j}(\rho u_j u_i)=-\frac{\partial p}{\partial x_i}+\frac{\partial \hat{\tau}_{ij}}{\partial x_j} \tag{3.2}$$

$$\frac{\partial \rho e_t}{\partial t}+\frac{\partial}{\partial x_j}(\rho u_i e_t)=-\frac{\partial p u_j}{\partial x_i}+\frac{\partial}{\partial x_j}\left[u_i\hat{\tau}_{ij}-q_j\right] \tag{3.3}$$

where e_t represents the total energy, and $\hat{\tau}_{ij}$ are composed of molecular and Reynolds stresses, defined as follows:

If the density of the flow is constant, Eq. (3.1) can be reduced to

$$\hat{\tau}_{ij}=2\mu(S_{ij}-\frac{1}{3}S_{kk}\delta_{ij})+\tau_{ij} \tag{3.4}$$

$$\tau_{ij}=2\mu_t(S_{ij}-\frac{1}{3}S_{kk}\delta_{ij})-\frac{2}{3}\rho k\delta_{ij} \tag{3.5}$$

$$S_{ij} = \frac{1}{2}\left(\frac{\partial u_i}{\partial x_j} + \frac{\partial u_j}{\partial x_i} \right) \tag{3.6}$$

where $\hat{\tau}_{ij}$ is the summation of laminar and turbulent stresses, and $\hat{\tau}_{ij}$ is the turbulent stress term. The velocity strain rate tensor is represented by S_{ij}, and k is the turbulent kinetic energy. The quantity μ is the molecular viscosity determined by the Sutherland law, and μ_t is the turbulent eddy viscosity. Note that the Boussinesq approximation is assumed to introduce Eq. 3.5. The total heat flux rate q_j is defined as

$$q_j = -\left(\frac{\gamma}{\gamma - 1} \right)\left(\frac{\mu}{\mathrm{Pr}} + \frac{\mu_t}{\mathrm{Pr}_t} \right)\frac{\partial T}{\partial x_j} \tag{3.7}$$

where γ is the ratio of specific heats, and the variables Pr and Pr_t are the laminar and turbulent Prandtl numbers, respectively.

The perfect gas equation of state is introduced to the pressure as follows:

$$p = \rho(\gamma - 1)\left(e - \frac{1}{2} u_i u_i \right) \tag{3.8}$$

The three-dimensional, compressible, Navier-Stokes equations are implemented on the flow solver by the non-dimensionalized and coordinate transformed equation. Flow variables are non-dimensionalized by freestream condition and the characteristic length as follows:

$$\rho^* = \frac{\rho}{\rho_\infty}, \quad u_i^* = \frac{u_i}{a_\infty}, \quad e_t^* = \frac{e_t}{e_{t\infty}}, \quad p^* = \frac{p}{\rho_\infty a^2},$$
$$x_i^* = \frac{x_i}{L}, \quad t^* = \frac{t}{L/a_\infty}, \quad T^* = \frac{T}{T_\infty} \tag{3.9}$$
$$\mu^* = \frac{\mu}{\mu_\infty}, \quad \mu_t^* = \frac{\mu_t}{\mu_\infty}$$

The compressible Navier-Stokes equations can be express in a general curvilinear coordinates of ξ, η, ζ as follows:

$$\frac{1}{J}\frac{\partial Q}{\partial t} = -\left(\frac{\partial}{\partial \xi}\left(\hat{E} - \hat{E}_v\right) - \frac{\partial}{\partial \eta}\left(\hat{F} - \hat{F}_v\right) - \frac{\partial}{\partial \zeta}\left(\hat{G} - \hat{G}_v\right)\right) \tag{3.10}$$

The Q vector represents the conservative variables, and E, F, G represent the flux vector of ξ-, η-, ζ-direction, respectively. The subscript v indicates the viscous flux. These vectors are composed as follows:

$$Q = \left[\rho, \rho u, \rho v, \rho w, \rho e_t\right]^T \tag{3.11}$$

$$\hat{E} = 1/J\left[\rho U, \rho u U + \xi_x p, \rho v U + \xi_y p, \rho w U + \xi_z p, (\rho e + p)U - \xi_t p\right]^T \tag{3.12}$$

$$\hat{F} = 1/J\left[\rho V, \rho u V + \eta_x p, \rho v V + \eta_y p, \rho w V + \eta_z p, (\rho e + p)V - \eta_t p\right]^T \tag{3.13}$$

$$\hat{G} = 1/J\left[\rho W, \rho u W + \zeta_x p, \rho v W + \zeta_y p, \rho w W + \zeta_z p, (\rho e + p)W - \zeta_t p\right]^T \tag{3.14}$$

$$\hat{E}_v = \frac{1}{J}\frac{M_\infty}{\mathrm{Re}}\begin{bmatrix} 0 \\ \xi_x\hat{\tau}_{xx} + \xi_y\hat{\tau}_{yx} + \xi_z\hat{\tau}_{zx} \\ \xi_x\hat{\tau}_{xy} + \xi_y\hat{\tau}_{yy} + \xi_z\hat{\tau}_{zy} \\ \xi_x\hat{\tau}_{xz} + \xi_y\hat{\tau}_{yz} + \xi_z\hat{\tau}_{zz} \\ \xi_x E_{v_5} + \xi_y F_{v_5} + \xi_z G_{v_5} \end{bmatrix} \tag{3.15}$$

$$\hat{F}_v = \frac{1}{J}\frac{M_\infty}{\mathrm{Re}}\begin{bmatrix} 0 \\ \eta_x\hat{\tau}_{xx} + \eta_y\hat{\tau}_{yx} + \eta_z\hat{\tau}_{zx} \\ \eta_x\hat{\tau}_{xy} + \eta_y\hat{\tau}_{yy} + \eta_z\hat{\tau}_{zy} \\ \eta_x\hat{\tau}_{xz} + \eta_y\hat{\tau}_{yz} + \eta_z\hat{\tau}_{zz} \\ \eta_x E_{v_5} + \eta_y F_{v_5} + \eta_z G_{v_5} \end{bmatrix} \tag{3.16}$$

$$\hat{G}_v = \frac{1}{J}\frac{M_\infty}{\mathrm{Re}}\begin{bmatrix} 0 \\ \zeta_x\hat{\tau}_{xx} + \zeta_y\hat{\tau}_{yx} + \zeta_z\hat{\tau}_{zx} \\ \zeta_x\hat{\tau}_{xy} + \zeta_y\hat{\tau}_{yy} + \zeta_z\hat{\tau}_{zy} \\ \zeta_x\hat{\tau}_{xz} + \zeta_y\hat{\tau}_{yz} + \zeta_z\hat{\tau}_{zz} \\ \zeta_x E_{v_5} + \zeta_y F_{v_5} + \zeta_z G_{v_5} \end{bmatrix} \tag{3.17}$$

where,

$$E_{v_5} = u\hat{\tau}_{xx} + v\hat{\tau}_{xy} + w\hat{\tau}_{xz} - q_x$$

$$F_{v_5} = u\hat{\tau}_{yx} + v\hat{\tau}_{yy} + w\hat{\tau}_{yz} - q_y$$

$$G_{v_5} = u\hat{\tau}_{zx} + v\hat{\tau}_{zy} + w\hat{\tau}_{zz} - q_z$$

and *U*, *V*, *W* represent contravariant velocity vector as

$$U = \xi_t + \xi_x u + \xi_y v + \xi_z w$$

$$V = \eta_t + \eta_x u + \eta_y v + \eta_z w$$

$$W = \zeta_t + \zeta_x u + \zeta_y v + \zeta_z w$$

For convenience, the superscript *, which means the non-dimensional value, is omitted from the equations.

If it is assumed the inviscid condition, all the viscous terms with subtitle *v* are ignored in Eq. 3.10. On the other hand and assuming *x*-axis symmetric condition, the equations from Eq.3.10 to Eq.3.16 are simplified as follows:

$$\frac{1}{J}\frac{\partial Q}{\partial t} = -\left(\frac{\partial}{\partial \xi}\left(\hat{E} - \hat{E}_v\right) - \frac{\partial}{\partial \eta}\left(\hat{F} - \hat{F}_v\right) - \frac{1}{y}\left(\hat{H} - \hat{H}_v\right) \right)$$

$$Q = \left[\rho, \rho u, \rho v, \rho e_t\right]^T$$

$$\hat{E} = {}^{1}\!/_{J}\left[\rho U, \rho u U + \xi_x p, \rho v U + \xi_y p, \left(\rho e + p\right)U - \xi_t p\right]^T$$

$$\hat{F} = {}^{1}\!/_{J}\left[\rho V, \rho u V + \eta_x p, \rho v V + \eta_y p, \left(\rho e + p\right)V - \eta_t p\right]^T$$

$$\hat{H} = {}^{1}\!/_{J}\left[\rho V, \rho U v + \zeta_x p, \rho V v + \zeta_y p, \rho H v\right]^T$$

$$\hat{E}_v = \frac{1}{J}\frac{M_\infty}{\mathrm{Re}}\begin{bmatrix} 0 \\ \xi_x\hat{\tau}_{xx} + \xi_y\hat{\tau}_{yx} \\ \xi_x\hat{\tau}_{xy} + \xi_y\hat{\tau}_{yy} \\ \xi_x E_{v_5} + \xi_y F_{v_5} \end{bmatrix}$$

$$\hat{F}_v = \frac{1}{J}\frac{M_\infty}{\mathrm{Re}}\begin{bmatrix} 0 \\ \eta_x\hat{\tau}_{xx} + \eta_y\hat{\tau}_{yx} \\ \eta_x\hat{\tau}_{xy} + \eta_y\hat{\tau}_{yy} \\ \eta_x E_{v_5} + \eta_y F_{v_5} \end{bmatrix}$$

$$\hat{H}_v = \frac{1}{J}H_v = \frac{1}{J}\begin{bmatrix} 0 \\ \tau_{xy} \\ \tau_{yy} - \tau_{\theta\theta} \\ u\tau_{xy} + v\tau_{yy} \end{bmatrix}$$

The H and $\hat{H}$ terms are axisymmetric sources.

3.2 Turbulence Model

For the adequate description of turbulent flow field within the framework of a Reynolds Averaged Navier-Stokes (RANS) formulation, Wilcox's original *k-ω* model [37, 38], the transformed the *k-ε* model [16], Menter's standard *k-ω* Shear Stress Transport (SST) model [16] and Menter's *k-ω* SST model developed in 2003 [39] are employed. These turbulence models are composed of two transport equations of the turbulent kinetic energy (*k)* and the dissipate rate (*ω)*.

3.2.1 The original *k-ω* model

The original *k-ω* model developed by Wilcox *et al.* is as follows:

$$\frac{\partial(\rho k)}{\partial t}+\frac{\partial(\rho k u_j)}{\partial x_j}=\tau_{ij}\frac{\partial u_i}{\partial x_j}-\beta^*\rho\omega k+\frac{\partial}{\partial x_j}\left[(\mu+\sigma_{k_1}\mu_t)\frac{\partial k}{\partial x_j}\right] \tag{3.18}$$

$$\frac{\partial(\rho\omega)}{\partial t}+\frac{\partial(\rho\omega u_j)}{\partial x_j}=\rho\frac{\gamma_1}{\mu_t}\tau_{ij}\frac{\partial u_i}{\partial x_j}-\beta_1\rho\omega^2+\frac{\partial}{\partial x_j}\left[(\mu+\sigma_{\omega_1}\mu_t)\frac{\partial \omega}{\partial x_j}\right] \tag{3.19}$$

with the coefficients of

$$\sigma_{k_1}=0.5,\ \sigma_{\omega_1}=0.5,\ \beta^*=0.09,\ \beta_1=0.075,\ \kappa=0.41$$
$$\gamma_1=\beta_1/\beta^*-\sigma_{\omega_1}\kappa^2/\sqrt{\beta^*}$$

The turbulent eddy viscosity μ_t is defined as the ratio of turbulent kinetic energy to the dissipation rate as

$$\mu_t=\rho k/\omega$$

3.2.2 The Transformed *k-ε* Model

The standard *k-ε* model is transformed into a *k-ω* formulation by using the relation of $\varepsilon=0.09\omega k$. Two differences exist between the transformed formulation and the original formulation. The first one is that a small additional diffusion term is neglected as an additional cross-diffusion term appears in the ω equation, and the other is the modeling parameters.

$$\frac{\partial(\rho k)}{\partial t}+\frac{\partial(\rho k u_j)}{\partial x_j}=\tau_{ij}\frac{\partial u_i}{\partial x_j}-\beta^*\rho\omega k+\frac{\partial}{\partial x_j}\left[(\mu+\sigma_{k_2}\mu_t)\frac{\partial k}{\partial x_j}\right] \tag{3.21}$$

$$\begin{aligned}\frac{\partial(\rho\omega)}{\partial t}+\frac{\partial(\rho\omega u_j)}{\partial x_j}&=\rho\frac{\gamma_2}{\mu_t}\tau_{ij}\frac{\partial u_i}{\partial x_j}-\beta_2\rho\omega^2\\&\quad+\frac{\partial}{\partial x_j}\left[(\mu+\sigma_{\omega_2}\mu_t)\frac{\partial\omega}{\partial x_j}\right]+2\rho\sigma_{\omega_2}\frac{1}{\omega}\frac{\partial k}{\partial x_j}\frac{\partial\omega}{\partial x_j}\end{aligned} \tag{3.22}$$

where

$$\sigma_{k_2}=1.0,\ \sigma_{\omega_2}=0.856,\ \beta^*=0.09,\ \beta_2=0.0828,\ \kappa=0.41$$
$$\gamma_2=\beta_2/\beta^*-\sigma_{\omega_2}\kappa^2/\sqrt{\beta^*}$$

3.2.3 The Standard Menter's *k-ω* Shear Stress Transport (SST) Model

The *k-ω* SST model is a hybrid turbulence model that combines the merits of *k-ω* and *k-ε* models by adopting an adequate blending function (F_1). On one hand, as it is well known, the *k-ω* model shows the excellent accuracy in the boundary layer even though the solution is sensitive to the freestream condition of *k* and *ω*. On the other hand,, the *k-ε* model can obtain a fair solution on the free shear layer and the outer region while the model is instable near the wall. Thus, these two models, the *k-ε* model and the *k-ω* model, are integrated to solve accurately and robustly the turbulence flow not only the near wall region but also the outer region. The blending function (F_1) is set to be one in the near wall region and to be zero at far away from the wall's surface. The combined equations are

$$\frac{\partial(\rho k)}{\partial t}+\frac{\partial(\rho k u_j)}{\partial x_j}=P-\beta^*\rho\omega k+\frac{\partial}{\partial x_j}\left[(\mu+\sigma_k\mu_t)\frac{\partial k}{\partial x_j}\right] \tag{3.23}$$

$$\frac{\partial(\rho\omega)}{\partial t}+\frac{\partial(\rho\omega u_j)}{\partial x_j}=\rho\frac{\gamma}{\mu_t}P-\beta\rho\omega^2+\frac{\partial}{\partial x_j}\left[(\mu+\sigma_\omega\mu_t)\frac{\partial\omega}{\partial x_j}\right] +2\rho(1-F_1)\sigma_{\omega_2}\frac{1}{\omega}\frac{\partial k}{\partial x_j}\frac{\partial\omega}{\partial x_j} \tag{3.24}$$

Each of the constants are defined by a blend of an inner constant of the k-ω model that is marked with the subscript 1 and outer constant of the k-ε model that is marked with the subscript 2, via:

$$\Phi=F_1\Phi_1+(1-F_1)\Phi_2 \tag{3.25}$$

where Φ represents the constant of Eqs. 3.18-19 and 3.21-22. Additional functions and limiters are given by

$$P=\tau_{ij}\frac{\partial u_i}{\partial x_j} \tag{3.26}$$

$$F_1=\tanh\left(\arg_1^4\right) \tag{3.27}$$

$$\arg_1=\min\left[\max\left(\frac{\sqrt{k}}{\beta^*\omega d},\frac{500\nu}{\omega d^2}\right),\frac{4\rho\sigma_{\omega_2}k}{CD_{k\omega}d^2}\right] \tag{3.28}$$

$$CD_{k\omega} = \max\left[2\rho\sigma_{\omega_2} \frac{1}{\omega}\frac{\partial k}{\partial x_j}\frac{\partial \omega}{\partial x_j}, 10^{-20} \right] \tag{3.29}$$

$$\mu_t = \frac{\rho a_1 k}{\max\left[a_1\omega, \Omega F_2\right]} \tag{3.30}$$

$$F_2 = \tanh\left(\arg_2^2\right) \tag{3.31}$$

$$\arg_2 = \max\left(2\frac{\sqrt{k}}{\beta^*\omega d}, \frac{500\nu}{\omega d^2} \right) \tag{3.32}$$

where d be the distance to the cell center point from the nearest wall, and Ω is the vorticity magnitude. The summary of the constants is

$$\gamma_1 = \beta_1/\beta^* - \sigma_{\omega_1}\kappa^2/\sqrt{\beta^*}, \quad \gamma_2 = \beta_2/\beta^* - \sigma_{\omega_2}\kappa^2/\sqrt{\beta^*}$$
$$\sigma_{k_1} = 0.85, \quad \sigma_{k_2} = 1.0, \quad \sigma_{\omega_1} = 0.5, \quad \sigma_{\omega_2} = 0.856$$
$$\beta^* = 0.09, \quad \beta_1 = 0.075, \quad \beta_2 = 0.0828, \quad \kappa = 0.41$$
$$a_1 = 0.31$$

Note that it is generally recommended to employ the production limiter, which replaces the term of P in the k-equation (Eq. 2-23) by

$$P = \min\left(P, 20\beta^*\rho\omega k\right) \tag{3.33}$$

The boundary conditions and freestream values are given as follows:

$$\frac{U_\infty^2}{10^5\,\mathrm{Re}_L} < k_{farfield} < \frac{U_\infty^2}{10\,\mathrm{Re}_L} \tag{3.33}$$

$$\frac{U_\infty}{L_{farfield}} < \omega_{farfield} < \frac{10U_\infty}{L_{farfield}} \tag{3.34}$$

$$k_{wall} = 0 \tag{3.35}$$

$$\omega_{wall} = \frac{60\mu}{\beta_1 \rho (\Delta d)^2} \tag{3.36}$$

The $L_{farfield}$ is the approximate length of the computational farfield domain from the wall, and a freestream turbulent viscosity μ_t has the value between 10^{-5} and 10^{-2} times freestream laminar viscosity.

3.2.4 The Menter's *k*-ω SST Model from 2003 (*k*-ω SST-2003)

The *k*-ω SST-2003 has several relatively minor variation from the original SST developed in 1994. The model enhancements cover a modified near wall treatment of the equations, which allows a more flexible grid form. This advantage reduces the problem of grid induced separation for industrial flow simulations. The changes are in the definition of eddy viscosity and in the production limiter of Eq. 2.30. The magnitude of vorticity in the eddy viscosity is changed to the strain invariant (*S*) in its definition as follows:

$$\mu_t = \frac{\rho a_1 k}{\max\left[a_1\omega, SF_2\right]} \tag{3.38}$$

where

$$S = \sqrt{2S_{ij}S_{ij}}$$

The production limiter is adopted for the *k*-equation in the original SST model, but this limiter is expanded to both *k*- and ω-equations. The limiting constant is also changed from 20 to 10.

$$P = \min\left(P, 10\beta^{*}\rho\omega k\right) \tag{3.39}$$

Another limiter in the definition of $CD_{k\omega}$ is slightly different in that it uses 10^{-10} rather than 10^{-20} for its second term.

$$CD_{k\omega} = \max\left[2\rho\sigma_{\omega_2}\frac{1}{\omega}\frac{\partial k}{\partial x_j}\frac{\partial \omega}{\partial x_j}, 10^{-10}\right] \tag{3.40}$$

The changed coefficients are

$$\gamma_1 = 5/9, \quad \gamma_2 = 0.44$$

3.3 Spatial Discretization

As shown in Eq. 2-10, the governing equations can be decomposed to the inviscid flux term and the viscous flux term. The inviscid flux terms in the ξ-, η-, and ζ-directions are discretized with a finite volume method based on the cell-centered approach. The local flux balance of each cell is

$$\left(\frac{\partial E}{\partial \xi}+\frac{\partial F}{\partial \eta}+\frac{\partial G}{\partial \zeta}\right)_{i,j,k} = \tilde{E}_{i+\frac{1}{2},j,k}-\tilde{E}_{i-\frac{1}{2},j,k} + \tilde{F}_{i,j+\frac{1}{2},k}-\tilde{F}_{i,j-\frac{1}{2},k} + \tilde{G}_{i,j,k+\frac{1}{2}}-\tilde{G}_{i,j,k-\frac{1}{2}} \tag{3.41}$$

Because Eq. 3.41 is in a central-differenced form and is non-dissipative by itself, the inviscid fluxes should be modified to the cell surface fluxes by explicitly adding the numerical dissipation term as follows:

$$\tilde{E}_{i+\frac{1}{2},j,k}=\frac{1}{2}\left[\hat{E}(Q_i)+\hat{E}(Q_{i+1})-\left|\hat{A}(Q_i,Q_{i+1})\right|(Q_{i+1}-Q_i)\right] \tag{3.42}$$

where the matrix $\hat{A}(Q_i,Q_{i+1})$ is the flux Jacobian matrix, and the inviscid flux is upwind-differenced. In this work, two types of flux schemes of Roe's FDS and RoeM are usually used for the spatial discretization.

The grid points are located in the red color vertex, the variables are posed in the cell-center indicated with green color, and the fluxes are calculated at the blue edge.

3.3.1 Roe's Flux Difference Splitting

Roe's Flux Difference Splitting (FDS) scheme is based on the approximate solution of Riemann problem [40]. Instead of solving the exact Riemann problem iteratively, Roe linearized the Jacobian matrix to satisfy the following properties:

(1) $\hat{A}$ is a linear mapping to $\hat{E}$ in a vector space Q

(2) $\hat{A}$ satisfies consistency condition, so $\hat{A}(Q,Q)=\hat{A}(Q)$

(3) $\hat{A}$ has linearly independent eigenvectors and real eigenvalues.

(4) $\hat{A}(Q_i,Q_{i+1})(Q_{i+1}-Q_i)=\hat{E}_{i+1}-\hat{E}_i$ for any $Q_i,\ Q_{i+1}$

From this condition (4), the linearized flux Jacobian $\hat{A}$ can be expressed in terms of Roe-averaged properties $\bar{\rho}$ and $\overline{Q}$ as:

$$\bar{\rho}=\sqrt{\rho_i\rho_{i+1}} \tag{3.43}$$

$$\overline{Q}=\frac{Q_i\sqrt{\rho_i}+Q_{i+1}\sqrt{\rho_{i+1}}}{\sqrt{\rho_i}+\sqrt{\rho_{i+1}}} \tag{3.44}$$

From the eigen matrix $\hat{X}$ of $\hat{A}$, the diagonal matrix Λ is composed of eigen values, and the condition 2, and the third term on the right-hand side of Eq. 3.42 is replaced into the vector calculation as:

$$\left|\hat{A}(Q)\right|(Q_{i+1}-Q_i)=\left(\hat{X}\left|\Lambda\right|\hat{X}^{-1}\right)\hat{X}\hat{\alpha}=\hat{X}\left|\Lambda\right|\hat{\alpha}=\hat{\alpha}_k\left|\lambda_k\right|\hat{e}_k \tag{3.45}$$

By using these Roe-averaged properties noted with the superscript of -, the flux can be calculated as follows:

$$\tilde{E}_{i+1/2}=\frac{1}{2}\left[\hat{E}(Q_i)+\hat{E}(Q_{i+1})-\hat{\alpha}_k\left|\lambda_k\right|\hat{e}_k\right] \tag{3.46}$$

$$\hat{\alpha}_k\left|\lambda_k\right|\hat{e}_k=\begin{bmatrix}\alpha_4\\ \bar{u}\alpha_4+\hat{\xi}_x\alpha_5+\alpha_6\\ \bar{v}\alpha_4+\hat{\xi}_y\alpha_5+\alpha_7\\ \bar{w}\alpha_4+\hat{\xi}_z\alpha_5+\alpha_8\\ \bar{H}\alpha_4+\left(\bar{U}-\xi_t\right)\alpha_5+\bar{u}\alpha_6+\bar{v}\alpha_7+\bar{w}\alpha_8-\dfrac{\bar{a}^2}{\gamma-1}\alpha_1\\ \alpha_9\\ \alpha_{10}\end{bmatrix} \tag{3.47}$$

The coefficients of α are

$$\alpha_1=\left|\lambda_1\right|\left(\Delta\rho-\frac{\Delta p}{\bar{a}^2}\right),\qquad \alpha_2=\left|\lambda_4\right|\left(\frac{\Delta p+\bar{\rho}\bar{a}\Delta U}{2\bar{a}^2}\right)$$

$$\alpha_3=\left|\lambda_5\right|\left(\frac{\Delta p-\bar{\rho}\bar{a}\Delta U}{2\bar{a}^2}\right),\qquad \alpha_4=\alpha_1+\alpha_2+\alpha_3$$

$$\alpha_5=\bar{a}\left(\alpha_2-\alpha_3\right),\qquad \alpha_6=\left|\lambda_1\right|\left(\bar{\rho}\Delta u-\hat{\xi}_x\bar{\rho}\bar{U}\right)$$

$$\alpha_7=\left|\lambda_1\right|\left(\bar{\rho}\Delta v-\hat{\xi}_y\bar{\rho}\bar{U}\right),\quad \alpha_8=\left|\lambda_1\right|\left(\bar{\rho}\Delta w-\hat{\xi}_z\bar{\rho}\bar{U}\right)$$

$$\alpha_9=\left|\lambda_1\right|\bar{\rho}\Delta k,\qquad \alpha_{10}=\left|\lambda_1\right|\bar{\rho}\Delta w$$

where

$$\lambda_1 = \lambda_2 = \lambda_3 = \frac{|\nabla\xi|}{J}\bar{U}, \qquad \lambda_{4,5} = \frac{|\nabla\xi|}{J}\left(\bar{U} \pm \bar{a}\right)$$

$$\bar{U} = \hat{\xi}_t + \hat{\xi}_x\bar{u} + \hat{\xi}_y\bar{v} + \hat{\xi}_z\bar{w}, \quad \hat{\xi}_{t,x,y,z} = \frac{\xi_{t,x,y,z}}{|\nabla\xi|} = \frac{\xi_{t,x,y,z}}{\sqrt{\xi_x + \xi_y + \xi_z}}$$

$$H = \left(e_t + p\right)\Big/\rho$$

The flux vectors $\tilde{F}_{j+1/2}$ and $\tilde{G}_{j+1/2}$ respectively on the η- and ζ-directions can be determined with a similar flux calculation.

3.3.2 RoeM Scheme

Although the Roe scheme shows remarkable accuracy, it is hard to distinguish a shock and an expansion discontinuity because the entropy condition is violated. The carbuncle phenomena also suffer the robustness of the original Roe scheme. In order to overcome these problems, Kim et al. [41] proposed an improved Roe scheme that is free from the shock instability and preserves the accuracy and efficiency of the original Roe scheme.

The flux can be calculated by the following:

$$\begin{aligned}\tilde{E}_{i+1/2} = {} & \frac{b_1 \times \hat{E}\left(Q_i\right) + b_2 \times \hat{E}\left(Q_{i+1}\right)}{b_1 - b_2} + \frac{b_1 \times b_2}{b_1 - b_2}\Delta Q^* \\ & - g\,\frac{b_1 \times b_2}{b_1 - b_2} \times \frac{1}{1 + \left|\bar{M}\right|} B\Delta Q\end{aligned} \tag{3.48}$$

$$B\Delta Q=\left(\Delta\rho-f\frac{\Delta p}{\hat{c}^2}\right)\begin{pmatrix}1\\ \bar{u}\\ \bar{v}\\ \bar{w}\\ \bar{H}\end{pmatrix}+\bar{\rho}\begin{pmatrix}0\\ \Delta u-\xi_x\Delta U\\ \Delta v-\xi_y\Delta U\\ \Delta w-\xi_z\Delta U\\ \Delta H\end{pmatrix} \tag{3.49}$$

where

$$\bar{M}=\bar{U}\big/\bar{a},\quad b_1=\max\left(0,\bar{U}+\bar{a},U_{i+1}+\bar{a}\right),\quad b_2=\max\left(0,\bar{U}-\bar{a},U_{i-1}+\bar{a}\right)$$

and the functions f and g can be expressed by:

$$f=\begin{cases}1 & ,\bar{u}^2+\bar{v}^2+\bar{w}^2=0\\ \left|\bar{M}\right|^h & ,elsewhere\end{cases},$$
$$h=1-\min\begin{pmatrix}P_{i+1/2,j,k},P_{i,j+1/2,k},P_{i,j-1/2,k},P_{i,j,k+1/2},P_{i,j,k-1/2},\\ P_{i+1,j+1/2,k},P_{i+1,j-1/2,k},P_{i+1,j,k+1/2},P_{i+1,j,k-1/2}\end{pmatrix} \tag{3.50}$$

$$g=\begin{cases}\left|\bar{M}\right|^{1-\min\left(\frac{p_{i,j}}{p_{i+1,j}},\frac{p_{i+1,j}}{p_{i,j}}\right)} & ,\bar{M}=0\\ 1 & ,\bar{M}\neq 0\end{cases} \tag{3.51}$$

The differentiation of the flux function becomes more complicated than the original Roe scheme because of the function *f*, which considers 10 cells around the interface.

3.3.3 AUSMPW+

The AUSMPW+ flux scheme was designed to remove the non-monotonic pressure oscillations of the AUSM-type schemes near a wall or behind shock waves by introducing pressure-based weighting functions at a cell's interface. The weight function ($F_{1/2}$) is introduced to treat the oscillations near a wall, and w to remove the oscillation across a strong shock. The flux vector at a cell's interface can be represented as

$$\hat{F}_{1/2} = \bar{M}_L^{+} c_{1/2} \hat{\Phi}_L + \bar{M}_R^{-} c_{1/2} \hat{\Phi}_R + (P_L^{+} \hat{p}_L + P_R^{-} \hat{p}_R) \tag{3.52}$$

where

$$\hat{\Phi} = (\rho \;\; \rho u \;\; \rho v \;\; \rho w \;\; \rho H)^T, \quad \hat{p} = (0 \;\; \bar{n}_x p \;\; \bar{n}_y p \;\; \bar{n}_z p \;\; 0)^T$$

To obtain Mach numbers on the left and right side of the cell's interface, the Mach number at the cell's interface is first defined by

$$m_{1/2} = M_L^{+} + M_R^{-} \tag{3.53}$$

and Mach numbers on the left and right side are expressed by Eqs. 2.18and 2.19, respectively

if $m_{1/2} \geq 0$,

$$\begin{aligned}\bar{M}_L^{+} &= M_L^{+} + M_R^{-}\cdot[(1-w)\cdot(1+f_R)-f_L] \\ \bar{M}_R^{-} &= M_R^{-}\cdot w\cdot(1+f_R)\end{aligned} \tag{3.54}$$

if $m_{1/2}<0$,

$$\begin{aligned}\bar{M}_L^{+} &= M_L^{+}\cdot w\cdot(1+f_L) \\ \bar{M}_R^{-} &= M_R^{-} + M_L^{+}\cdot[(1-w)\cdot(1+f_L)-f_R]\end{aligned} \tag{3.55}$$

To compute Eqs. 2.18 and 2.19, pressure based weight function ($f_{L,R}$)and w are defined as

$$f_{L,R} = \begin{cases} \left(\frac{p_{L,R}}{p_s}-1\right)\times\min\left(1,\frac{\min(p_{1,L},p_{1,R},p_{2,L},p_{2,R})}{\min(p_L,p_R)}\right)^2 & if\ p_s\neq 0\ , \\ 0 & if\ p_s = 0 \end{cases} \tag{3.56}$$

where $p_s = P_L^{+}p_L + P_R^{-}p_R$ and $p_{1,*}, p_{2,*}$ are the pressure values at each edge of a cel'sl interface.

Equations 2.18 to 2.21 use the split Mach number and pressure across a cell's interface as the input values. These values are introduces as

$$M^{\pm} = \begin{cases} \pm\frac{1}{4}(M\pm 1)^2, & |\mathrm{M}|\le 1 \\ \frac{1}{2}(M\pm|\mathrm{M}|), & |\mathrm{M}|>1 \end{cases} \tag{3.58}$$

$$p^{\pm} = \begin{cases} \frac{1}{4}(M \pm 1)^2 \cdot (2 \mp M), & |\mathrm{M}| \le 1 \\ \frac{1}{2}(1 \pm \mathrm{sign}(\mathrm{M})), & |\mathrm{M}| > 1 \end{cases} \tag{3.59}$$

In Eqs. 2.22 and 2.23, the Mach number on each side is defined as follows:

$$M_{L,R} = \frac{U_{L,R}}{c_{1/2}}$$

Here, $c_{1/2}$ is the speed of sound at a cell interface and computed as

$$c_{1/2} = \min\left[\frac{a^{*2}}{\max(|U_L|, a^*)}, \frac{a^{*2}}{\max(|U_R|, a^*)} \right] \tag{3.60}$$

where the critical speed of sound a^* is defined to satisfy the isoenergetic condition,

$$a^* = \sqrt{\frac{2(\gamma - 1)}{(\gamma + 1)} H}$$

with H as the total enthalpy and U as the velocity component normal to a cell's interface.

3.3.3 Higher order spatial accuracy

Monotone Upstream-centered Schemes for Conservation Laws (MUSCL) can provide highly accurate numerical solution for a given system. Even in cases where the solutions exhibit shocks, discontinuities occurs [14]. The MUSCL scheme is adopted as the following:

$$\begin{aligned} q_{i+1/2}^{Left} &= q_i + \frac{1}{4}\left[(1-\kappa)\phi_{i-1/2}^{+}(q_i - q_{i-1}) + (1+\kappa)\phi_{i+1/2}^{-}(q_{i+1} - q_i)\right] \\ q_{i+1/2}^{Right} &= q_{i+1} + \frac{1}{4}\left[(1+\kappa)\phi_{i+1/2}^{-}(q_{i+1} - q_i) + (1-\kappa)\phi_{i+3/2}^{+}(q_{i+2} - q_{i+1})\right] \end{aligned} \tag{3.61}$$

where q denotes the primitive variables. With the constant κ=1/3, the order of spatial accuracy is one third, and the second order of accuracy is achieved with κ=-1, 0, 1. Especially at κ=1, it becomes a central, different scheme of the second order. Values of the primitive variables at the cell's interface are modified by extrapolation, which causes an oscillation near the physical discontinuities. To suppress this overshoot phenomenon of the solution, several limiters can be applied by using a function ϕ.

Because the MUSCL scheme is developed in the one-dimensional approach, it is insufficient to control oscillation near the shock discontinuity in two- or three-dimensions. To overcome this limitation, the Multi-dimensional Limiting Process (MLP) [42] is also adopted. By expressing the vertex point value in terms of variations across the cell's interface and by adopting the multi-dimensional restriction coefficient α, the MLP derives the multi-dimensional limiting function. The MLP scheme is

$$
\begin{aligned}
q_{i+1/2}^{Left} &= q_i + \frac{1}{2}\phi\left(r_{Left}\right)\Delta q_{i-1/2} \\
q_{i+1/2}^{Right} &= q_{i+1} - \frac{1}{2}\phi\left(r_{Right}\right)\Delta q_{i+3/2}
\end{aligned}
\tag{3.62}
$$

where

$$
\begin{aligned}
& r_{Left} = \frac{\Delta q_{i+1/2}}{\Delta q_{i-1/2}}, \quad r_{Right} = \frac{\Delta q_{i+1/2}}{\Delta q_{i+3/2}} \\
& \phi(r) = \max\left(0, \min\left(\alpha, \alpha r, \beta\right)\right) \\
& 1 \le \alpha \le \min\left[2, \frac{2\max\left(1, r_{Left,j}\right)\left(1+\max\left(0, \tan\bar{\theta}_{j+1}/r_{Right,j+1}\right)\right)}{\left(1+\tan\tilde{\theta}_j\right)}\right] \\
& \tan\tilde{\theta}_j = \Delta q_x^+ \Big/ \Delta q_y^+, \quad \tan\bar{\theta}_j = \Delta q_{i+1/2,j} \Big/ \Delta q_{i,j+1/2}
\end{aligned}
$$

and $\Delta q_{x,y}^{\pm}$ is a variation from center point to the cell's interface. The coefficient β is the local slope evaluated by a higher order polynomial interpolation, which is determined by the third-order polynomial interpolation as follows:

$$
\beta_{Left} = \frac{1+2r_{Left,i}}{3} \quad \beta_{Right} = \frac{1+2r_{Right,i+1}}{3} \tag{3.63}
$$

or the fifth-order polynomial interpolation

$$\beta_{Left} = \frac{-2/r_{Left,i} + 11 + 24r_{Left,i} - 3r_{Left,i}r_{Left,i+1}}{30}$$
$$\beta_{Right} = \frac{-2/r_{Right,i+2} + 11 + 24r_{Right,i+1} - 3r_{Right,i+1}r_{Right,i}}{30} \tag{3.64}$$

3.3.4 Compact Scheme for Viscous Fluxes

In order to discretize the viscous flux terms, a second order of central differencing is adopted. The 9 components for three-dimensional case are

$$\begin{aligned}
&\frac{\partial}{\partial\xi}\left(\alpha\frac{\partial q}{\partial\xi}\right), \quad \frac{\partial}{\partial\xi}\left(\alpha\frac{\partial q}{\partial\eta}\right), \quad \frac{\partial}{\partial\xi}\left(\alpha\frac{\partial q}{\partial\zeta}\right),\\
&\frac{\partial}{\partial\eta}\left(\alpha\frac{\partial q}{\partial\xi}\right), \quad \frac{\partial}{\partial\eta}\left(\alpha\frac{\partial q}{\partial\eta}\right), \quad \frac{\partial}{\partial\eta}\left(\alpha\frac{\partial q}{\partial\zeta}\right),\\
&\frac{\partial}{\partial\zeta}\left(\alpha\frac{\partial q}{\partial\xi}\right), \quad \frac{\partial}{\partial\zeta}\left(\alpha\frac{\partial q}{\partial\eta}\right), \quad \frac{\partial}{\partial\zeta}\left(\alpha\frac{\partial q}{\partial\zeta}\right)
\end{aligned} \tag{3.65}$$

where α contains the molecular and turbulent viscosity and the Jacobian, and metrics of the transformation, and q denotes the primitive variables.

For instance, the non-cross derivative components are differenced by using a compact three-point formula, such as the following:

$$\begin{aligned}
\frac{\partial}{\partial\xi}\left(\alpha\frac{\partial q}{\partial\xi}\right)_{i,j,k} &= \frac{\alpha_{i+1,j,k} + \alpha_{i,j,k}}{2}\left(q_{i+1,j,k} - q_{i,j,k}\right)\\
&\quad - \frac{\alpha_{i,j,k} + \alpha_{i-1,j,k}}{2}\left(q_{i,j,k} - q_{i-1,j,k}\right)
\end{aligned} \tag{3.66}$$

The cross derivative components are differenced by using the following nine-point formula:

$$\frac{\partial}{\partial\xi}\left(\alpha\frac{\partial q}{\partial\eta}\right)_{i,j,k} = \frac{\alpha_{i+1,j,k}+\alpha_{i,j,k}}{8}\left[\left(q_{i+1,j+1,k}-q_{i,j+1,k}\right)-\left(q_{i+1,j-1,k}-q_{i,j-1,k}\right)\right] - \frac{\alpha_{i,j,k}+\alpha_{i-1,j,k}}{8}\left[\left(q_{i,j+1,k}-q_{i-1,j+1,k}\right)-\left(q_{i,j-1,k}-q_{i-1,j-1,k}\right)\right] \tag{3.67}$$

Likewise, the other components can be differenced by the same formula.

3.4 Time Integration Method

In this chapter, by replacing t with τ, the implicit methods of solving the pseudo-time equation, Eq. 3.10, is represented with the vector of the residual $R(Q)$ in order to consider the time integrating formulation easily as

$$\frac{1}{J}\frac{\partial Q}{\partial\tau} = -R(Q) \tag{3.68}$$

A first-order Euler implicit formula is used for pseudo-time derivative to form the matrix equation. The next consideration is the formation of the Jacobian matrix of the residual vector of the flux terms required for the implicit side of the resulting equation. However, the exact Jacobian of the flux vectors is quite costly to form. Instead, an approximate Jacobian of the residual vector can be used with different levels of approximation. Then, the matrix equation is solved using LU symmetric Gauss-Seidel (SGS) relaxation scheme.

3.4.1 Pseudo-Time Discretization

From Eq. 3.10 in the previous chapter, the system of governing equations can be rewritten as the following:

$$\frac{1}{J}\frac{\partial Q^{n+1}}{\partial \tau}+\left[\frac{\partial}{\partial \xi}\left(\hat{E}-\hat{E}_v\right)+\frac{\partial}{\partial \eta}\left(\hat{F}-\hat{F}_v\right)+\frac{\partial}{\partial \zeta}\left(\hat{G}-\hat{G}_v\right)\right]+\hat{S}=0 \tag{3.69}$$

Consider a Taylor series expansion about the time level *n* as follows:

$$E^{n+1}=E^n+\left[\frac{\partial E}{\partial Q}\right]\Delta Q+O(\Delta t^2)\cong E^n+A\Delta Q \tag{3.70}$$

In a similar fashion, the other flux vectors can be linearized as

$$\begin{aligned} F^{n+1}&\cong F^n+B\Delta Q \\ G^{n+1}&\cong G^n+C\Delta Q \end{aligned} \tag{3.71}$$

The viscous flux Jacobian in the implicit part is neglected, for it does not influence the solution's accuracy; therefore, the viscous flux vectors are approximated as follows:

$$\begin{aligned} E_v^{n+1}&\cong E^n \\ F_v^{n+1}&\cong F^n \\ G_v^{n+1}&\cong G^n \end{aligned} \tag{3.72}$$

by substituting the above linearizations in Eq. 3.69 to obtain

$$\frac{1}{J}\frac{\partial Q^{n+1}}{\partial \tau}+\left[\frac{\partial}{\partial \xi}\left(\hat{E}+A\Delta Q\right)+\frac{\partial}{\partial \eta}\left(\hat{F}+B\Delta Q\right)+\frac{\partial}{\partial \zeta}\left(\hat{G}+C\Delta Q\right)\right] \\ -\left(\frac{\partial E_v}{\partial \xi}+\frac{\partial F_v}{\partial \eta}+\frac{\partial G_v}{\partial \zeta}\right)+\hat{S}=0 \tag{3.73}$$

and by rewriting the Eq. 3.73

$$\frac{1}{J}\frac{\partial Q^{n+1}}{\partial \tau}+\frac{\partial}{\partial \xi}\left(A\Delta Q\right)+\frac{\partial}{\partial \eta}\left(B\Delta Q\right)+\frac{\partial}{\partial \zeta}\left(C\Delta Q\right) \\ =-\left(\frac{\partial}{\partial \xi}\left(\hat{E}+E_v\right)+\frac{\partial}{\partial \eta}\left(\hat{F}+F_v\right)+\frac{\partial}{\partial \zeta}\left(\hat{G}+G_v\right)\right)^n-\hat{S} \tag{3.74}$$

and is factored as

$$\left(\frac{1}{J\Delta \tau}+\frac{\partial A}{\partial \xi}+\frac{\partial B}{\partial \eta}+\frac{\partial C}{\partial \zeta}\right)\Delta Q \\ =-\left(\frac{\partial}{\partial \xi}\left(\hat{E}+E_v\right)+\frac{\partial}{\partial \eta}\left(\hat{F}+F_v\right)+\frac{\partial}{\partial \zeta}\left(\hat{G}+\hat{G}_v\right)\right)^n-\hat{S}=-R^n \tag{3.75}$$

where I is the identity matrix, and R stand for the residual vector including viscous and turbulence terms. The flux Jacobian matrices are split according to the signs of the eigenvalues of the flux Jacobian matrices as

$$\left(\frac{1}{J\Delta\tau}+\delta_\xi^+A^+ +\delta_\xi^-A^- +\delta_\eta^+B^+ +\delta_\eta^-B^- +\delta_\zeta^+C^+ +\delta_\zeta^-C^-\right)\Delta Q=-R^n \tag{3.76}$$

where δ denotes a finite difference operator in each direction.

3.4.2 LU-SGS Scheme

Yoon et al. [15] introduced an implicit algorithm based on a lower-upper factorization and Gauss-Seidel relaxation. Rewriting Eq.(3.76 in detail yields

$$\begin{aligned}&\left[\frac{1}{J\Delta\tau}+A_i^+ -A_{i-1}^+ +A_{i+1}^- -A_i^- +B_j^+ -B_{j-1}^+ +B_{j+1}^- -B_j^-\right.\\&\left.+C_k^+ -C_{k-1}^+ +C_{k+1}^- -C_k^-\right]\Delta Q=-R_{i,j,k}^n\end{aligned} \tag{3.77}$$

and Eq. 3.76 can be rewritten in a compact form as

$$\begin{aligned}&\left[\left(\frac{1}{J\Delta\tau}+\rho(A)+\rho(B)+\rho(C)\right)I-A_{i-1}^+ +A_{i+1}^- -B_{j-1}^+ +B_{j+1}^- -C_{k-1}^+ +C_{k+1}^-\right]\Delta Q\\&=-R_{i,j,k}^n\end{aligned} \tag{3.78}$$

and the flux Jacobian matrices are split approximately to yield diagonal dominance as

$$\begin{aligned}&A^\pm=\frac{1}{2}\left(A+\rho(A)\right),B^\pm=\frac{1}{2}\left(B+\rho(B)\right),C^\pm=\frac{1}{2}\left(C+\rho(C)\right)\\&\rho(A)=A_i^+ -A_i^-,\rho(B)=B_i^+ -B_i^-,\rho(C)=C_i^+ -C_i^-\end{aligned} \tag{3.79}$$

where $\rho(A) = \kappa|\lambda(A)|$ and k denotes a constant that is between 1.01 and 1.5. In the present work, k is given 1.1 for incompressible problems. Rewriting Eq. 3.78 yields

$$r_{i,j,k} I\Delta Q - A^{+}_{i-1}\Delta Q + A^{-}_{i+1}\Delta Q - B^{+}_{j-1}\Delta Q + B^{-}_{j+1}\Delta Q - C^{+}_{k-1}\Delta Q + C^{-}_{k+1}\Delta Q = -R^{n}_{i,j,k} \quad (3.80)$$

where

$$r_{i,j,k} = \frac{1}{J\Delta\tau} + \rho(A) + \rho(B) + \rho(C) \quad (3.81)$$

The above factored equation is solved as a series of following lower and upper sweeps.

Lower Sweep:

$$\begin{aligned} r_{i,j,k} I\Delta\hat{Q}^{*}_{i,j,k} &= \hat{R}^{n}_{i,j,k} + \hat{A}^{+}_{i-1,j,k}\Delta\hat{Q}^{*}_{i-1,j,k} + \hat{B}^{+}_{i,j-1,k}\Delta\hat{Q}^{*}_{i,j-1,k} + \hat{C}^{+}_{i,j,k-1}\Delta\hat{Q}^{*}_{i,j,k-1} \\ &\quad - \hat{A}^{-}_{i+1,j,k}\Delta\hat{Q}^{*}_{i+1,j,k} - \hat{B}^{-}_{i,j+1,k}\Delta\hat{Q}^{*}_{i,j+1,k} - \hat{C}^{-}_{i,j,k+1}\Delta\hat{Q}^{*}_{i,j,k+1} \\ &\approx \hat{R}^{n}_{i,j,k} + \hat{A}^{+}_{i-1,j,k}\Delta\hat{Q}^{*}_{i-1,j,k} + \hat{B}^{+}_{i,j-1,k}\Delta\hat{Q}^{*}_{i,j-1,k} + \hat{C}^{+}_{i,j,k-1}\Delta\hat{Q}^{*}_{i,j,k-1} \\ &= DCV_{i,j,k} \end{aligned} \quad (3.82)$$

Upper Sweep:

$$
\begin{aligned}
r_{i,j,k} I\Delta\hat{Q}_{i,j,k}^{n+1} &= \hat{R}_{i,j,k}^{n} + \hat{A}_{i-1,j,k}^{+}\Delta\hat{Q}_{i-1,j,k}^{n+1} + \hat{B}_{i,j-1,k}^{+}\Delta\hat{Q}_{i,j-1,k}^{n+1} + \hat{C}_{i,j,k-1}^{+}\Delta\hat{Q}_{i,j,k-1}^{n+1} \\
&\quad - \hat{A}_{i+1,j,k}^{-}\Delta\hat{Q}_{i+1,j,k}^{n+1} - \hat{B}_{i,j+1,k}^{-}\Delta\hat{Q}_{i,j+1,k}^{n+1} - \hat{C}_{i,j,k+1}^{-}\Delta\hat{Q}_{i,j,k+1}^{n+1} \\
&\approx \hat{R}_{i,j,k}^{n} + \hat{A}_{i-1,j,k}^{+}\Delta\hat{Q}_{i-1,j,k}^{*} + \hat{B}_{i,j-1,k}^{+}\Delta\hat{Q}_{i,j-1,k}^{*} + \hat{C}_{i,j,k-1}^{+}\Delta\hat{Q}_{i,j,k-1}^{*} \\
&\quad - \hat{A}_{i+1,j,k}^{-}\Delta\hat{Q}_{i+1,j,k}^{n+1} - \hat{B}_{i,j+1,k}^{-}\Delta\hat{Q}_{i,j+1,k}^{n+1} - \hat{C}_{i,j,k+1}^{-}\Delta\hat{Q}_{i,j,k+1}^{n+1} \\
&= DCV_{i,j,k} - \hat{A}_{i+1,j,k}^{-}\Delta\hat{Q}_{i+1,j,k}^{n+1} - \hat{B}_{i,j+1,k}^{-}\Delta\hat{Q}_{i,j+1,k}^{n+1} - \hat{C}_{i,j,k+1}^{-}\Delta\hat{Q}_{i,j,k+1}^{n+1}
\end{aligned}
\tag{3.83}
$$

Consequently, the LU-SGS scheme can be written in the following form:

$$
LD^{-1}U\Delta Q = R^{n} \tag{3.84}
$$

3.4.3 Dual Time Stepping

For time-accurate. unsteady problems, a pseudo-time, sub-iteration strategy is adopted to solve the unsteady, incompressible systems of Eq. 3.69 given by

$$
\frac{1}{J}\frac{\partial\hat{Q}}{\partial t} = -\hat{R} \quad . \tag{3.85}
$$

The time derivative term is differenced using a backward, second-order, three-point, implicit formula and moved to the right-hand side of the equation:

$$
0 = -\frac{1.5\mathrm{Q}^{n+1} - 2Q^{n} + 0.5Q^{n-1}}{J\Delta t} - \hat{R}^{n+1} \quad . \tag{3.86}
$$

A pseudo-time derivative of Q is added on the left-hand side of Eq. 3.86:

$$\frac{1}{J}\frac{\partial Q^{n+1}}{\partial \tau} = -\hat{R}^{n+1} - \frac{1.5Q^{n+1} - 2Q^{n} + 0.5Q^{n-1}}{J\Delta t} = -\hat{R}^{n+1} - \hat{S}^{n+1} \quad . \tag{3.87}$$

Because the first-order discretization in general has better convergence properties than the higher-order, the pseudo-time derivative term is discretized using the first-order Euler implicit formula:

$$\frac{1}{J}\frac{Q^{n+1,m+1} - Q^{n+1,m}}{\Delta \tau} = -\hat{R}^{n+1,m+1} - \hat{S}^{n+1,m+1} \quad . \tag{3.88}$$

where a superscript m denotes the pseudo-time iteration level. The time accuracy of the solution is necessary in terms of the physical time, but not in terms of the pseudo-time. The dual time stepping method adopted here, therefore, has second-order time accuracy. Now, Eq. 3.88 can be rewritten as the following:

$$\frac{1}{J\Delta \tau} + \left[\frac{\partial \hat{R}}{\partial Q} + \frac{\partial \hat{S}}{\partial Q}\right]^{n+1,m} \Delta Q^{n+1,m} = -\hat{R}^{n+1,m} - \hat{S}^{n+1,m} \tag{3.89}$$

For steady-state calculations, the source-like term S is dropped from the equation because Δt is set to infinity. Then Eq. 3.89 is simplified for the steady-state calculation as

$$\frac{1}{J\Delta \tau} + \left[\frac{\partial \hat{R}}{\partial Q}\right]^{m} \Delta Q^{m} = -\hat{R}^{m}. \tag{3.90}$$

3.5 Geometric Modeling and Boundary Condition

3.5.1 Axisymmetric Inlet Modeling for Viscous Computation

The axisymmetric inlet model [4] of Nagashima's experiment is used for the current computational study. As shown in Fig. 4, the model is composed of a center body, cowl, and plug components. The plug attached at the rear part of the model moves back and forth to control the throttling ratio. As mentioned previously, the throttling ratio (T.R) is defined as the area ratio between the exit and inlet as seen in Fig. 4. Pressure data are measured at seven positions as shown in Fig. 5 which are the same as in the experiment. P1, P2, and P3 sensors are on the compression ramp, and P4 to P7 sensors are on the internal cowl surface. The pressure histories at P1, P2, and P3 sensors show whether the shock passes the sensor location or not. Passing these sensor locations, the terminal shock induces separation vortices, which are one of the important sources of shock instability or inlet buzz. P3 also provides properties of flow variables, such as pressure, Mach number, and mass flow rate at the inlet throat area. P4 is in the middle of the diffuser, and P5 is at the end of the diffuser. The diffuser area gradually increases along the downstream direction, and P4 and P5 indicate the pressure variation and wave propagation in diffusing process. P6 is at the entrance surface of the combustion chamber. P6 indicates back pressure, which is controlled by the throttling plug. Last, the pressure of the emission flow just before the exit nozzle is measured by P7. All the sensors from P3 to P7 at the internal surface of the engine are located on the boundaries between the engine's components or the changing points of the internal area. By analyzing the recorded pressure histories at seven sensors, we can investigate inlet buzz

characteristics by capturing wave propagation at each sensor position (or engine component).

The pressure history of each sensor shows the inlet characteristics at each throttling ratio. Using the FFT analysis, the dominant frequency of the inlet buzz is obtained. Figure 6 depicts the grid topology. The grid system consists of 11 blocks with approximately 40,000 meshes, with each block having 51 axial points and 71 radial points. Figure 6b depicts mesh points around the compression ramp of the center body. These meshes are clustered around the cowl tip to obtain accurate results. On the internal and external surface of the inlet, the non-dimensional size of the first grid point off the wall is approximately y^{+}=1, and there are 20 grid points with a stretching ratio of 1.25 to resolve boundary layer. The free stream Mach number is 2, and the Reynolds number is 10^{7} with respect to the characteristic length of the inlet diameter ($L^{*}=D=60mm$). The inflow stagnation speed of sound is 330.2 *m/s*. Supersonic inflow and outflow conditions are applied at the boundaries.

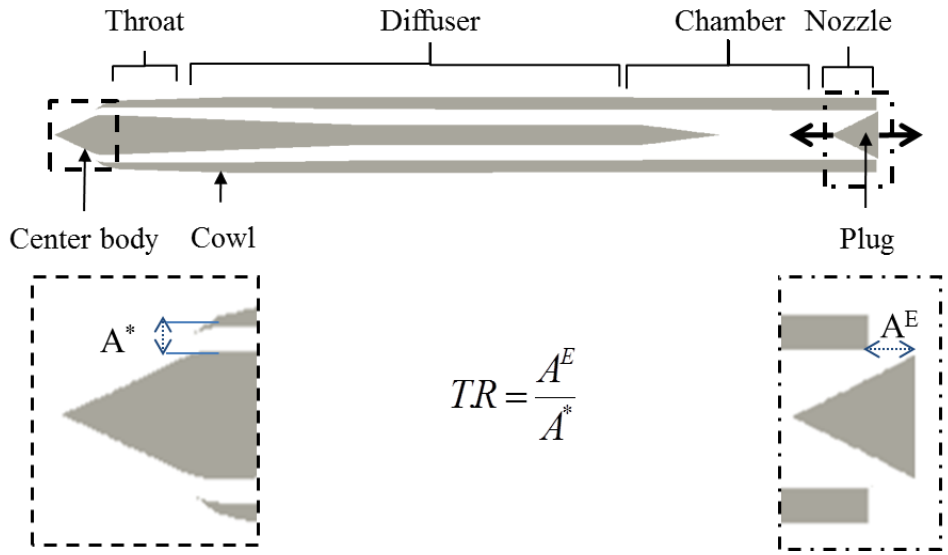

Fig. 4 Configuration of inlet model and definition of throttling ratio.

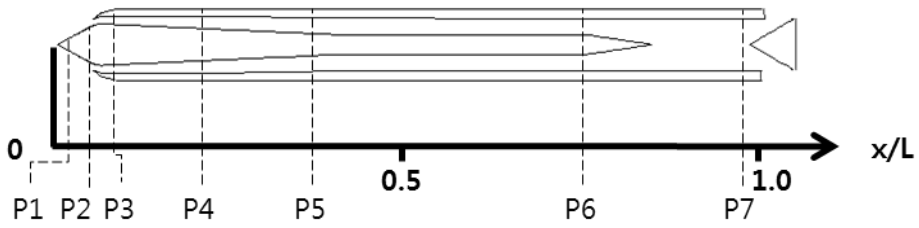

Fig. 5 Location of pressure sensors.

3.5.2 Modeling of Varying Exit Area for Mass Flow Control

To consider the movement of the plug that controls the exit area, a sliding mesh system and a patched grid method [17] are applied to the internal grids of the chamber and the exit nozzle as depicted in Figs. 6c,d,e, and f. As the exit nozzle moves, additional grid points are generated and move backward as shown in Fig. 6c. Figures 6d,e, and f show the procedure to increase the exit-area. When the internal grids move backward, the interface between the internal and external block increases accordingly (or the throttling ratio increases). In order to maintain a high level of grid density near the plug wall and the interface, two patched grid blocks are introduced as shown in the red and blue parts of Figs. 6d,e,and f. Each block has a dimension of 301 grid points in the sliding direction and 11 grid points in the other direction. With the sliding/patched grid system, the throttling area from the complete closed (Fig. 6d) to the complete open condition (Fig. 6f) can be realized. This grid system is applied to all cases

of the present inlet computations. It is noted that once the two patched grids are included, the total number of grid point is increased by nearly 6,000.

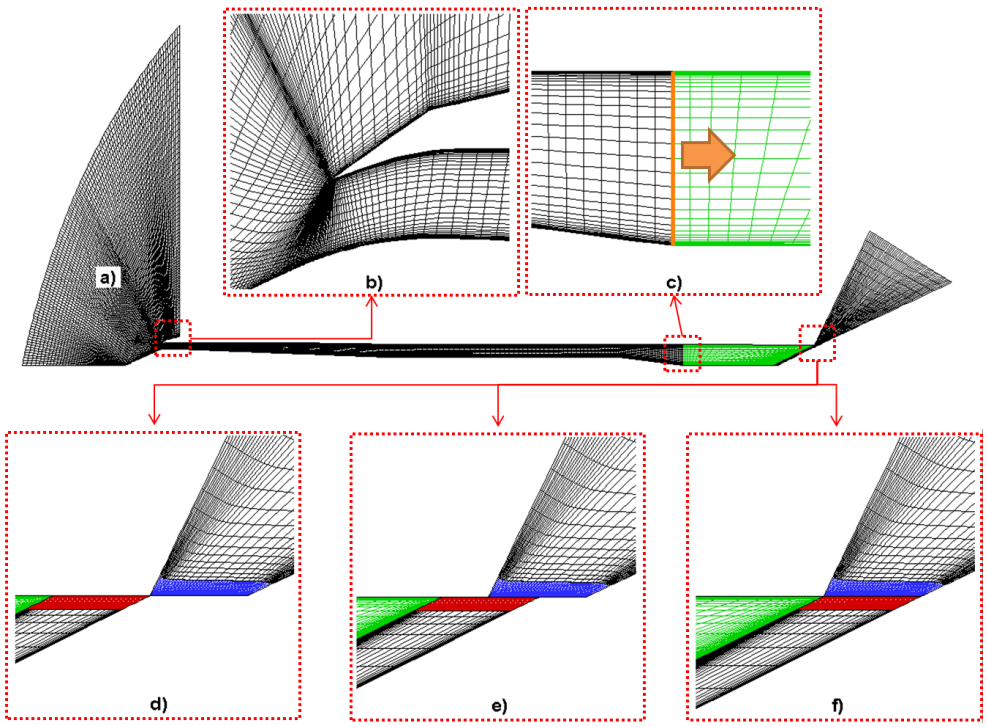

Fig. 6 Grid topology and exit grid moving with patched grid interface.

3.5.3 Three-dimensional Inlet Modeling for Inviscid Computation

An axisymmetric engine configuration [4] is used in the current study. As shown in Fig. 4, the engine has a center-body, cowl, and plug components. The plug attached at the rear part of the engine moves back and forth to control the throttling ratio (T.R). The definition of throttling ratio is explained in Fig. 4. Figure 6-1a depicts the grid topology and boundary conditions. The three-dimensional grid system consists of 80 blocks and approximately 0.7 million meshes. Half of the meshes are for the interior domain, and the dimension is 250 axial points, 35 interior radial points, and 40 axis rotational points with referring

to Newsome's grid [5] for turbulent flow simulation (190 of axial points 30 of interior radial points). Meshes around the compression ramp of the center body and the cowl lip section are properly clustered to obtain accurate results.

The free stream Mach number is 2 and the atmospheric condition is referred to the standard sea level air [4]. The unit length is 60mm (diameter of the inlet), and the stagnation speed of sound is 330.2m/s. The computational domain is shown in Fig. 6-1b. For efficient calculations, the exterior domain is limited to two essential parts, which are near the inlet and exit. Boundary conditions for the exterior domain near the inlet are straightforward because the velocity across the outer boundary surfaces is supersonic. Mach 2 inflow conditions and simple extrapolation are applied for this part. For the other exterior domain, the pressure or mass flow rate makes boundary conditions easy. Without the exterior domain, the pressure or mass flow rate has to be given at the exit of the chamber, which might be occasionally arbitrary. Because the exterior domain includes the diverging nozzle area, the flow is accelerated, and the velocity across the outer surfaces of the attached domain is supersonic . Thus, similar to the exterior domain near the inlet, the simple inflow condition (blue dashed line) and the extrapolation (orange dashed line) can be applied as shown in Fig. 6-1b.

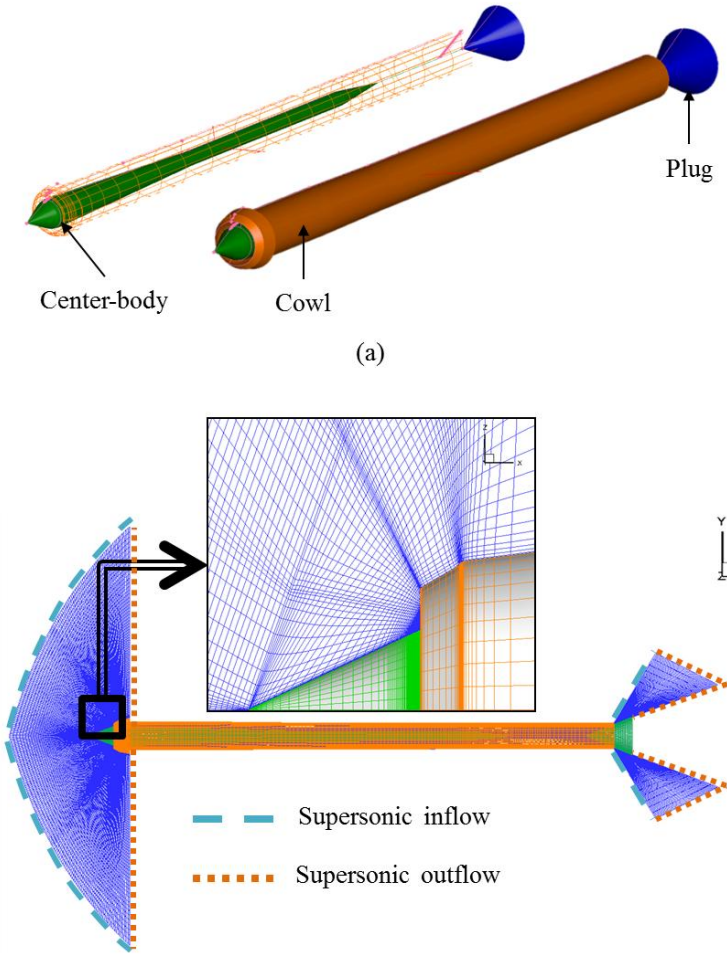

Fig. 6-1. Engine geometry and elements (a), grid topology and boundary conditions (b)

Chapter IV
Inlet Buzz Simulation with Throttling Ratio Control

As mentioned above, there are three groups of inlet buzz simulations with throttling ratio control. At first, Case 1 of the inlet without a center body is simulated. Next, the inlet with the center body under mass flow decreasing process is considered for Case 2, and lastly, the same geometry with mass flow increasing process is applied for Case 3. Depending on normal shock position, there are three flow regimes for supersonic inlet: supercritical, critical, and subcritical regimes. In subcritical condition, normal shock is located out of inlet, and inlet buzz is readily generated. By simulating inlet buzz in Case 2 and Case 3, subcritical conditions are mainly dealt with.

4.1 Case1 - Validation by Inlet Configuration without Center Body

The flow solver is validated by simulating Nagashima's experiment configuration with the center body removed. The results will be also used later for discussing the effects of the center body. The pipe theory for instrument acoustics can be applied to this problem because the exit is closed and the cross sectional area along the axial direction is nearly constant. Following Shang and Hankey's proposition [7], the *N*-th mode of natural frequency with an open and close end pipes can be given as in references 5 and 8. They assumed that a

downstream travelling wave propagates at speed $c+v$ until it reaches a reflection surface at distance (L). c is the speed of sound, and v is the speed of downstream flow. Next, it returns at the speed of c-v until it reaches the origin and repeats the cycle. The time period for this process is

$$\Delta t = \frac{L}{c+v} + \frac{L}{c-v} \tag{4.1}$$

The frequency and harmonics mode N of the oscillation are given by

$$f_N = \frac{N}{\Delta t} = \frac{N}{L(\frac{1}{c+v} + \frac{1}{c-v})} \tag{4.2}$$

which can be written as

$$f_N = \frac{N(c - \frac{v^2}{c})}{2L} = \frac{Nc(1-M^2)}{2L} \quad , \; M = \frac{v}{c} \tag{}$$

N is replaced with $(2N\text{-}1)$ and $2L$ is replaced with $4L$ for open-close end pipe as follows:

$$f_N = \frac{c}{4L}(1-M^2)(2N-1), N = 1,2,3,\ldots \tag{4.4}$$

Here, L is the inlet length, M is the averaged Mach number inside the inlet, and N is the mode number. These values are presented in Table 1. In Case 1, c is

the stagnation speed of sound, for the exit is blocked. and the net mass flow rate through the inlet is zero. With Eq. 4.4, the first mode of natural frequency is estimated as 130Hz, while Nagashima's experimental frequency is 140Hz.

Table 1 Input variables for inlet simulations

Mach number (M_∞)	2.0
Reynolds number (Re)	10^7
Stagnation speed of sound (C_0)	330.2 *m/s*
Inlet diameter ($D = L^*$) and length (L)	0.06m /0.635m

Time step sensitivity and grid refinement test are carried out to determine a proper time step size and grid density for efficient and accurate unsteady computations. Four different grid densities and five time step sizes are examined as presented in Table 2.

Table 2 Grid refinement and time step sensitivity test.

Case	Grid number ($i \times j \times$ block)	Time step size
G1	27511 (41×61×11)	2.5×10^{-5}
G2	39831 (51×71×11)	2.5×10^{-5}
G3	57706 (61×86×11)	2.5×10^{-5}
G4	78881 (71×101×11)	2.5×10^{-5}
T1	39831 (51×71×11)	1.0×10^{-4}
T2	39831 (51×71×11)	5.0×10^{-5}
T3	39831 (51×71×11)	3.75×10^{-5}
T4	39831 (51×71×11)	2.5×10^{-5}
T5	39831 (51×71×11)	1.25×10^{-5}

The number of grid points increases about 35~45% as the grid level goes up by one from G1 to G4, while the grid points near wall are the same for capturing the boundary layer. For a time step size of $\Delta t = 2.5\times10^{-5}$ second, which corresponds to the non-dimensional time step ($\Delta t^* \equiv \Delta t\, U_\infty / L^*$) of 0.1, G2, G3 and G4 grid systems, which yield the dominant frequency of 141.66 ± 0.37Hz, as shown in Fig. 7. Thus, the G2 grid system is chosen, and time step sensitivity is carried out. Unsteady calculations with the G2 grid system are conducted for $\Delta t = 1.25\times10^{-5}$, 2.5×10^{-5}, 5.0×10^{-5} and 1.0×10^{-4} in order to capture the fundamental mode of frequency (130 Hz from Eq. 4.4 or 140 Hz from experiment) with sufficient temporal accuracy. There are 100 to 600 steps in one period of 130Hz with the given time steps. As shown in Fig. 7b, T3, T4, and T5 cases predict the frequency around 140 Hz. For computational efficiency and numerical accuracy, the G2 grid system with 2.5×10^{-5} time step size (T4) is used.

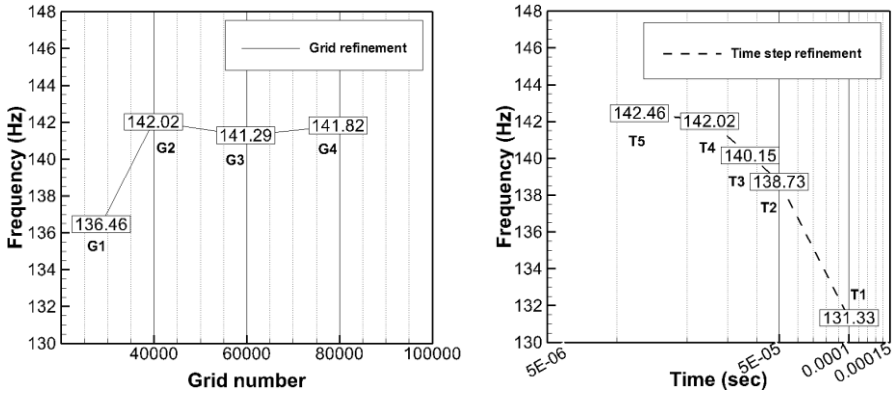

a) **b)**

Fig. 7 Grid refinement and time step sensitivity results (Case 1).

Both inviscid and viscous computations are conducted, and the results are summarized in Table 3. The first mode frequency obtained from front (P4) and rear (P7) positions is 134Hz and 142Hz in inviscid and viscous calculation,

respectively. These are close to the theoretical value (130Hz) and the experimental result (140Hz). Amplitude of pressure oscillation in the inviscid case is four times larger than the viscous case because viscosity induces pressure loss (or damping). This is also related to the 4% lower total pressure recovery in the viscous case. As shown in Figs. 8 and 9, the temporal pressure rise and drop repeatedly appears. In the viscous case, the captured flow is less compressed because of viscous loss; therefore, pressure peaks are less conspicuous. Eventually, a period of pressure fluctuations becomes shortened, and the dominant frequency gets 10Hz higher.

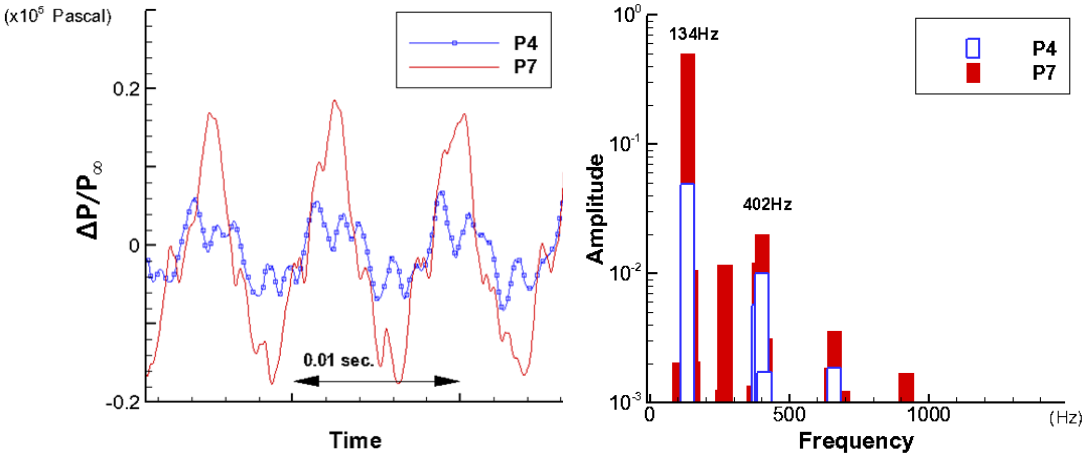

a) **b)**

Fig. 8 Pressure history and FFT analysis in inviscid simulation (Case 1).

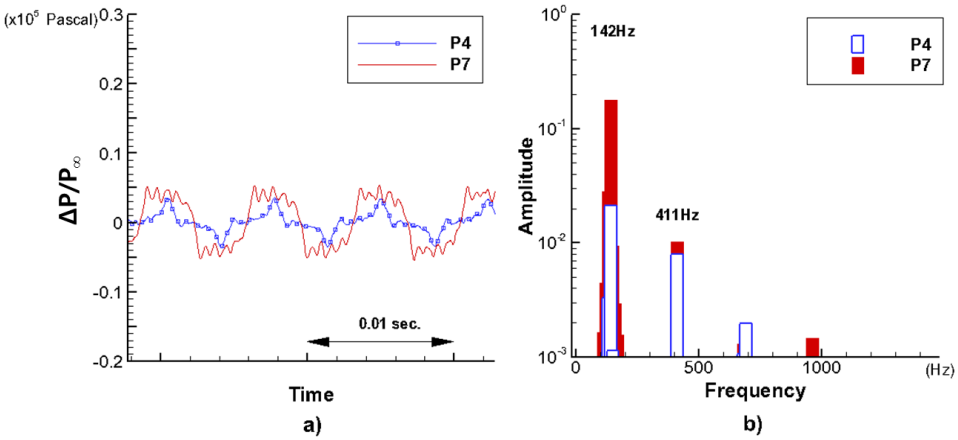

Fig. 9 Pressure history and FFT analysis in viscous simulation (Case 1).

Table 3 Summary of computed results (without-center body inlet case).

	Euler	Navier-Stokes
Dominant frequency (f, Hz)	134	142
Amplitude at P7 ($\Delta P/P_\infty$)	0.4	0.1
Averaged static pressure at P7 ($P_{avg.}/P_\infty$)	5.67	5.59
Averaged total pressure recovery at P7 (η)	0.74	0.71
Shock travel distance ($\Delta x_{s.t}/L^*$)	0.02	0.005

To check the center body effect on the pressure oscillation of inlet, Case 1 results are compared to the experimental data of which configuration includes the center body. Magnitude of the pressure amplitude and the shock-travel distance of Case 1 (or $\Delta P/P_\infty$ and $\Delta x_{s.t}/L^*$ in Table 3) are found to be 10% of the experimental results. In other words, Case 1 results are much more stable than the experimental results with the center body. This indicates that flow instability is triggered or amplified by the center body, and the flow physics around the

center body play an important role. There is a bow shock in front of the cowl tip as shown in Figs. 10a and b, and the non-dimensionalized shock traveling distance in the *x*-direction ($\Delta x_{s,t}^{*}$) is relatively short, 0.005 or 0.02. Furthermore, the state of the cowl tip vortex in Fig. 10 c, known as one of the buzz triggering factors, does not change much in time. This tells that, under without-center-body configuration, pressure oscillation is not excited enough to destabilize the shock. The relation between vortex behavior and inlet buzz triggering mechanism will be detailed in Section 4.5.

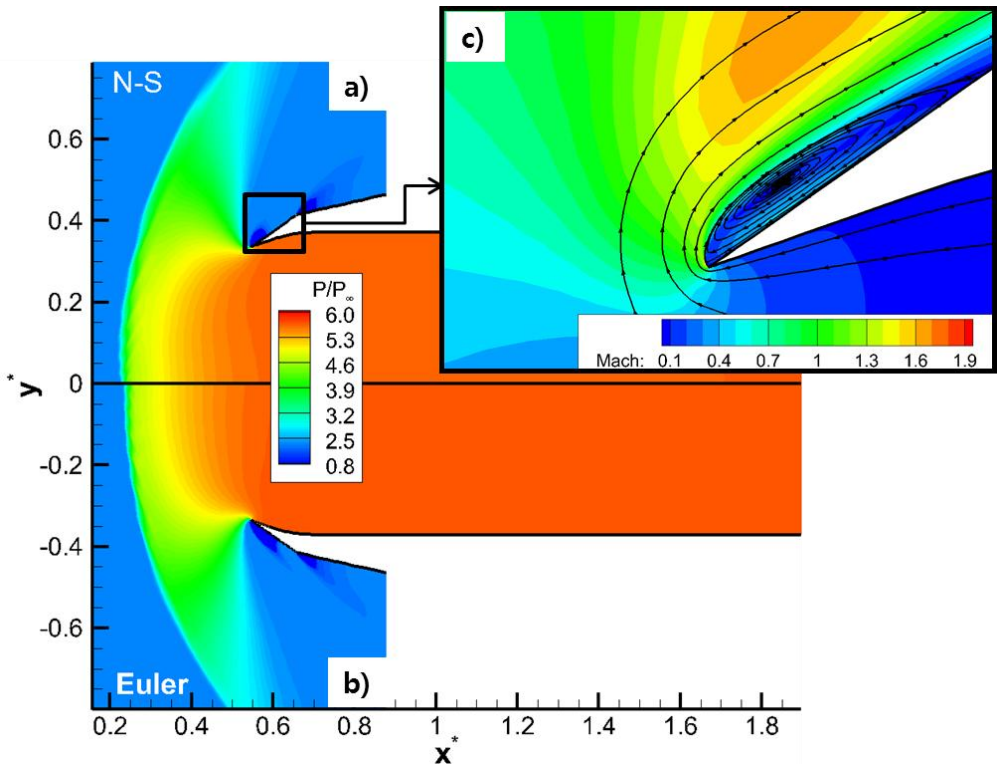

Fig. 10 Pressure contour (a), b)), Mach contour (c)) and streamline pattern of viscous simulation (Case 1).

4.2 Case2 - Inlet under Decreasing Mass Flow (T.R) Condition

In order to examine mass flow rate or throttling ratio effects on inlet buzz characteristics, simulations are conducted at eleven throttling ratios for inlet geometry with the center-body. Throttling ratios given in Table 4 are the same as Nagashima's experiment. Simulation starts from the throttling ratio (T.R) of 2.41 at which inlet buzz does not appear. The throttle area is then reduced at a constant rate. When T.R reaches the next smaller value, such as from the initial starting value of 2.41 to the next smaller value of 1.62, it is maintained for more than ten periodic flow cycles. Likewise, it repeats the same process until throttle area is closed completely (T.R = 0). As shown in Table 4, the throttling ratios are classified in three ranges: large, medium, and small. . Experimentally, inlet buzz does not appear at large throttling ratios, a low frequency buzz arises at medium throttling ratios, and a high frequency buzz occurs at small throttling ratios.

Table 4 Throttling ratios for inlet buzz simulations.

Small throttling ratio					Medium throttling ratio			Large throttling ratio		
0	0.21	0.35	0.55	0.67	0.79	0.97	1.14	1.42	1.62	2.41

4.2.1 Large Throttling Ratio (2.41 ~ 1.42)

The computed flow field is steady at the throttling ratio of 2.41, but the flow regime is subcritical condition. Moreover, inlet buzz occurs at the other two ratios. These results are somewhat different from the experimental observation. To explain the difference, a three-dimensional Navier-Stokes computation is conducted at the throttling ratio of 2.41 using the same numerical scheme with

nearly four million grids. Three parameters (the axial position of the terminal shock, static pressure at P2 sensor after oblique shock, and the mass flow rate at exit area) are then compared with the axisymmetric case. As shown in Fig. 11, overall pressure distributions are similar but, critically, the position of the terminal shock is different. It is a subcritical condition in axisymmetric modeling while, in three-dimensional computation, it is supercritical condition as in experimental observation. Further comparisons are summarized in Table 5. Because of the three-dimensional flow effect, the axisymmetric case yields a 5% smaller mass flow rate. These differences can be understood by examining the vortical structure at inlet throat. Figure 11b depicts the streamline pattern of the 3-D helical vortex along the circumferential direction. Because of the three-dimensional flow effect, the 3-D vortex becomes noticeably smaller than the axisymmetric case (Fig. 11a), which gives a larger effective throat area. Conversely, the axisymmetric vortex is larger than the 3-D case to give a smaller effective throat area, which leads to the difference in Table 5.

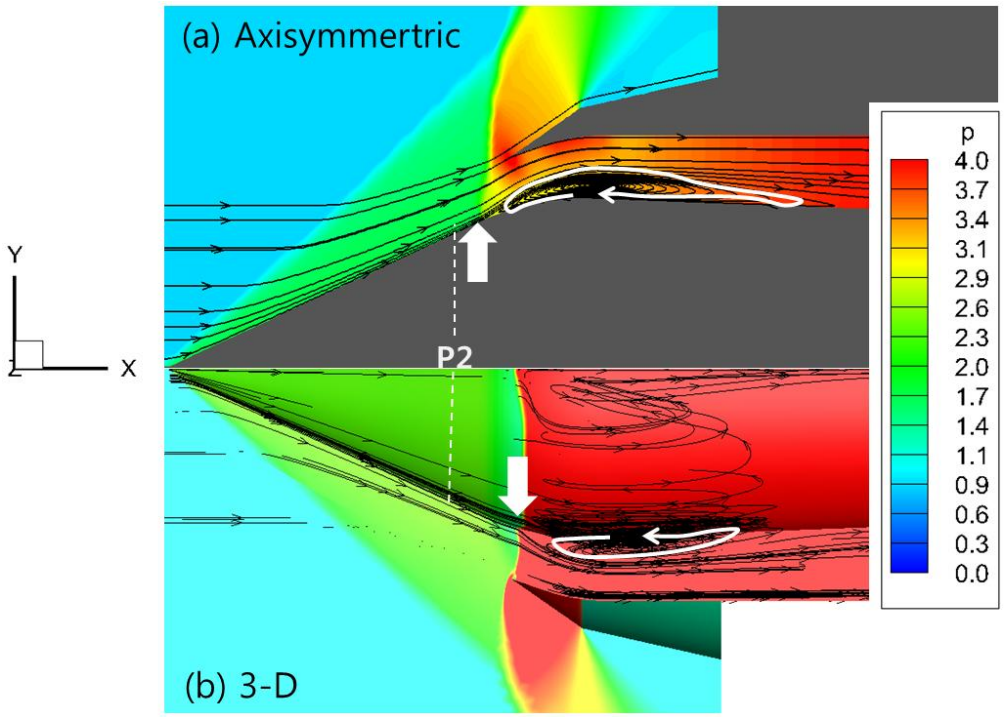

Fig. 11 Pressure contour and streamline pattern of axisymmetric computation (a) and 3-D computation (b).

Table 5 Comparison between axisymmetric and 3-D computation results.

	$x^*_{t.s}$ $(=x_{t.s}/L^*)$	P_{2s}/P_∞	$\dot{m}^*_e$
Axisymmetric	0.517 (sub-critical)	2.31	0.696
3-D	0.551 (super-critical)	2.31	0.731

However, this does not mean that the axisymmetric computed results are not reliable. It does mean that the throttling ratio becomes effectively smaller in the axisymmetric case than the actual experiment, and thus inlet buzz is triggered a bit earlier. Though the 3-D effect distributes a little in vortex size, it yields the difference of subcritical and supercritical condition because the flow regime is very sensitive at T.R=2.41 and near critical condition. As the throttling ratio

decreases, the size of shock induced vortex becomes larger because of the stronger shock that the portion of 3-D effect is lessened and after all, ignorable at small throttling ratio. To be more precise, by shifting the effect of changing the throttling ratio a little bit (the axisymmetric shifting effect), all the axisymmetric computed results match well the experimental data and the observations as shown at small throttling ratio. Additional validation will be given later. Because of the axisymmetric shifting effect in the throttling ratio, the results of medium and small throttling ratios are presented in the next.

Table 6 Dominant frequencies at large throttling ratios in the decreasing T.R process.

T.R	Dominant frequency (Hz)	
	Computation	Experiment
2.41	0	0
1.62	100	0
1.42	108	0

4.2.2 Medium Throttling Ratio (1.14 ~ 0.79)

In the medium throttling ratio of 1.14 to 0.79, experimentally observed inlet buzz starts at T.R = 1.14, with the low frequency buzz around 100 Hz. As mentioned previously, the starting buzz throttling ratio obtained from the axisymmetric computations is a bit shifted to a higher value because of the axisymmetric shifting effect. As a result, inlet buzz is initiated at the throttling ratio of 1.62. Tables 6 and 7 show that the inlet buzz frequency gradually increases as the throttling ratio decreases, and this tendency agrees well with the reference data (Nagashima's experimental data). Figure 12 shows pressure histories and FFT analyses results at the throttling ratio of 1.14. The dominant frequency and higher harmonics are 110, 335, and 560 Hz

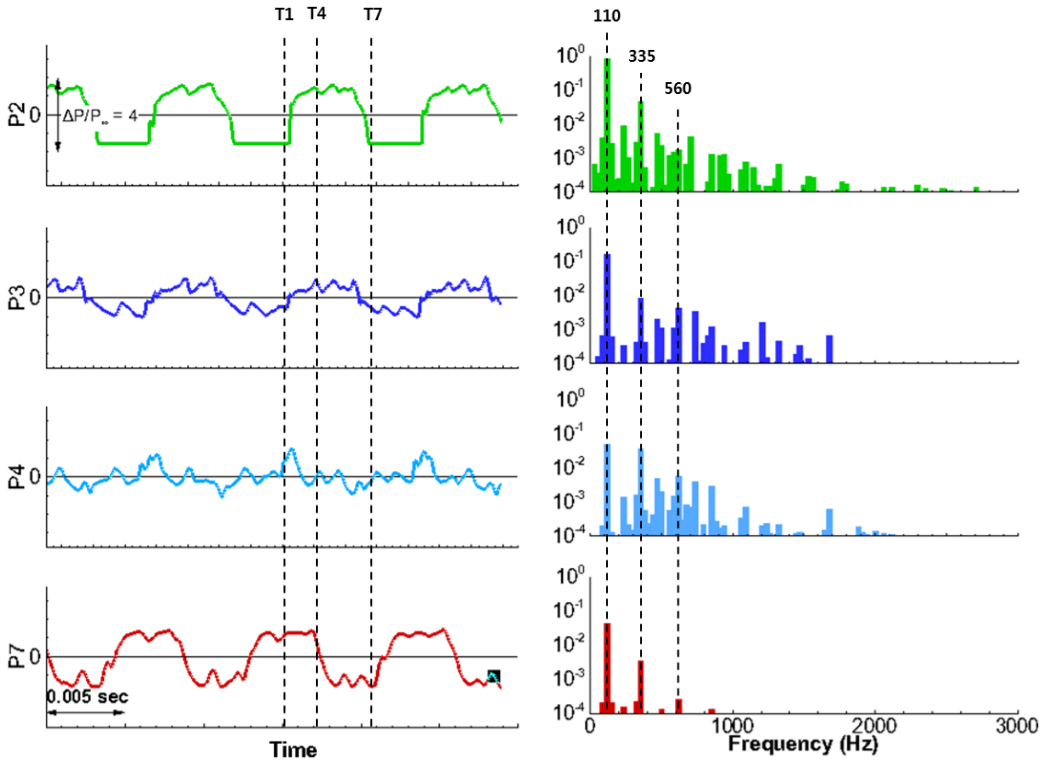

Fig. 12 Pressure history and FFT analysis at T.R = 1.14.

Table 7. Dominant frequencies at medium throttling ratios in decreasing process.

T.R	Dominant frequency(Hz)		
	Computation	T.R shifting	Experiment
1.14	110	→	88
0.97	121	→	109
0.79	360	→	138
0.67	367	→	360

Figure 13 depicts snapshots of the Mach number distributions with stream lines in a cycle of inlet buzz. It shows the successive shock movement and the associated vortex evolution. First, generated at throat area, the throat vortex repeats growth and decay in a buzz cycle. Frames T_1 to T_4 show a forwarding-shock process while frames T_5 to T_9 indicate a retreating-shock process. Each frame of the process has been taken at an equal time interval, and the instants of T_1, T_4, and T_7 are shown in Fig. 12a.

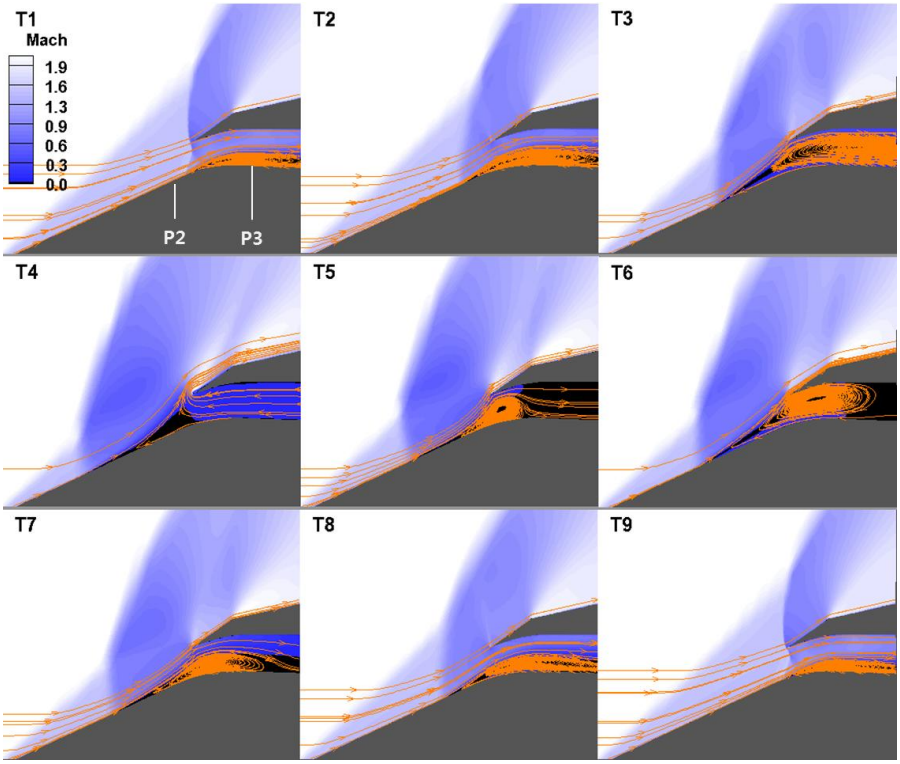

Fig. 13 Snap shots of inlet buzz sequence with Mach contour and flow pattern at T.R = 1.14.

Figure 14 shows the results at the throttling ratio of 0.97. Overall characteristics are similar to the case of T.R = 1.14, and the dominant frequency has a little bit higher value of 121Hz. Amplitude of normalized pressure

fluctuation is depicted in Fig. 15. It is noted from Table 7 that both computations with/without the axisymmetric shifting effect and experiment belong to the low frequency buzz range. Thus, computed pressure amplitudes of inlet buzz at seven sensors should agree very well with the reference data, as shown Fig. 15.

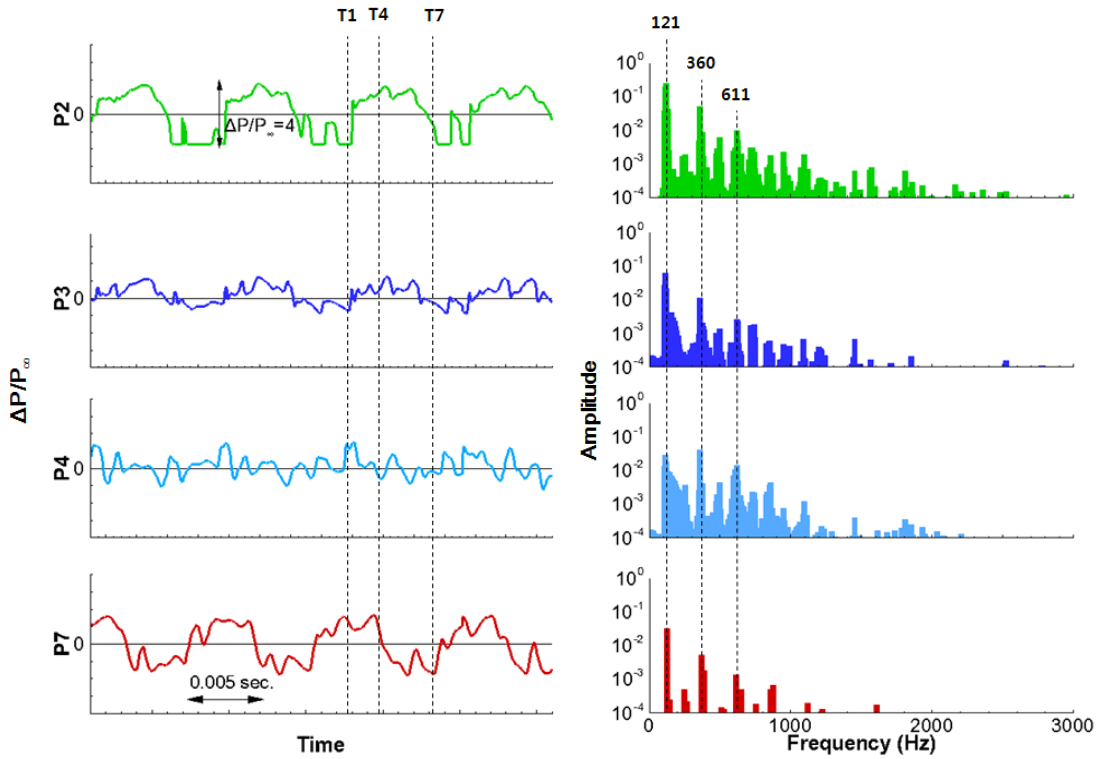

a) b)

Fig. 14 Pressure history and FFT analysis at T.R = 0.97.

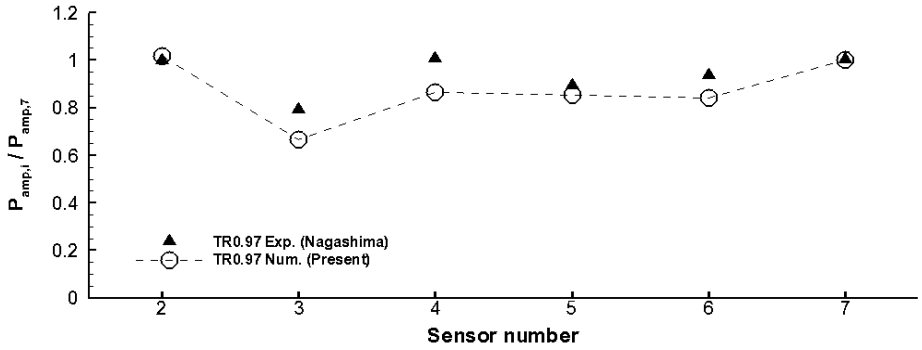

Fig. 15 Pressure amplitude of inlet buzz normalized by P7 value at T.R = 0.97.

On the other hand, at the throttling ratio of 0.79, the dominant frequency suddenly jumps from 121 to 360Hz, while the reference data remain at 133Hz. Again, this is caused by the transition from low to high buzz which occurred earlier because of the axisymmetric shifting effect. Experimentally, a similar buzz transition occurs at the throttle ratio of 0.67 from 138 to 360Hz. Table 7 summarizes the dominant frequencies at medium throttling ratios.

4.2.3 Small Throttling Ratio (0.67 ~ 0)

With a small throttling ratio from 0.67 to 0, inlet buzz rises in high frequency. Computational results show that the dominant frequency abruptly increased approximately three times higher when the throttling ratio passes through 0.97 to 0.79. This transition occurs at larger throttling ratio than the experiment in which the frequency jumps up at 0.79 to 0.67. At this range of throttling ratio, it undergoes a transition phase with random and oscillatory pressure history curves. When it reaches at 0.67, the oscillation is established in periodic pattern. As it shown in Fig. 16, the dominant frequency is 367Hz, and this value is near the second mode from the estimation by using Eq. 4.4. This high frequency buzz is captured by both of the computational and experimental

method. The frames T_4 and T_5 in Fig. 17 show new type of vortex that was not observed in Fig. 13. It is expected that the vortex adds more acoustic wave to the oscillating flow. The effect of the vortexes on inlet buzz is detailed in latter discussion. Figure 18 shows the results from two methods. The upper half images are the computational results, and the other half of the black-and-white figures are experimental Schlieren images. The number in each figure means the frame number and the speed is 5800 frames per a second. From the critical condition of frame 22 in Fig. 18, computational frames are in sync with the same interval of experimental frames. Bow shock positions and the overall flow pattern predicted by numerical results agree well with the experimental Schieren images. Nagashima observed this transition phenomenon but did not suggest a clear explanation for it. Not only dominant frequency but also harmonic series are shifted in higher modes.

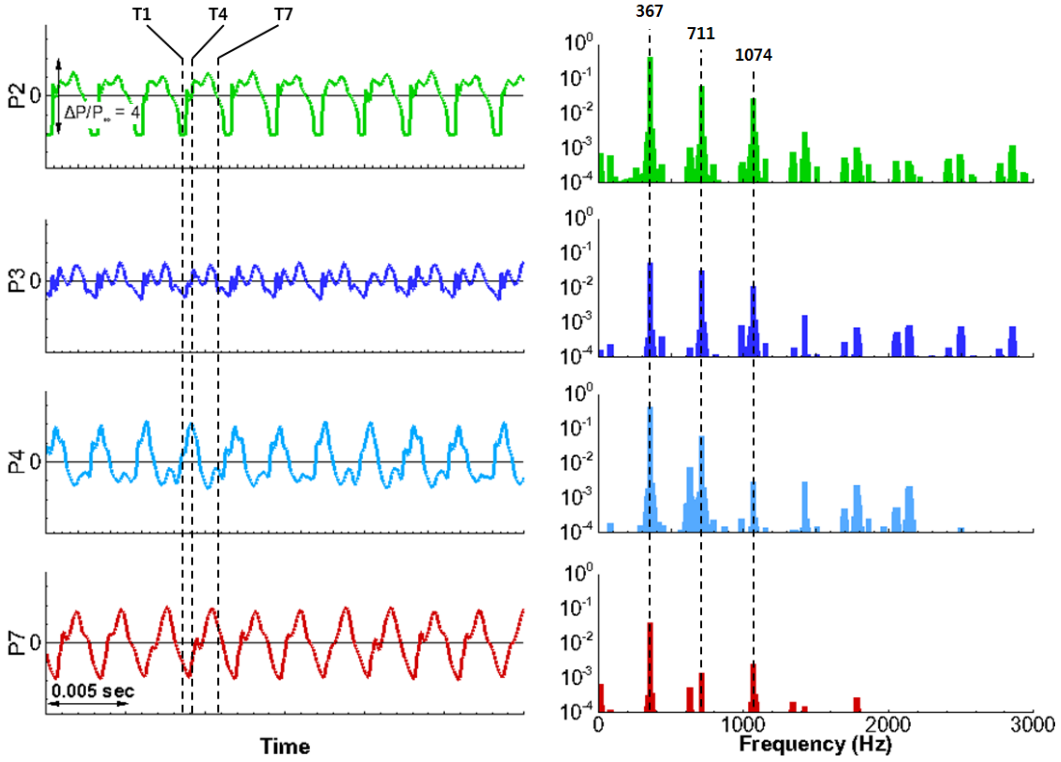

Fig. 16 Pressure history and FFT analysis at T.R = 0.67.

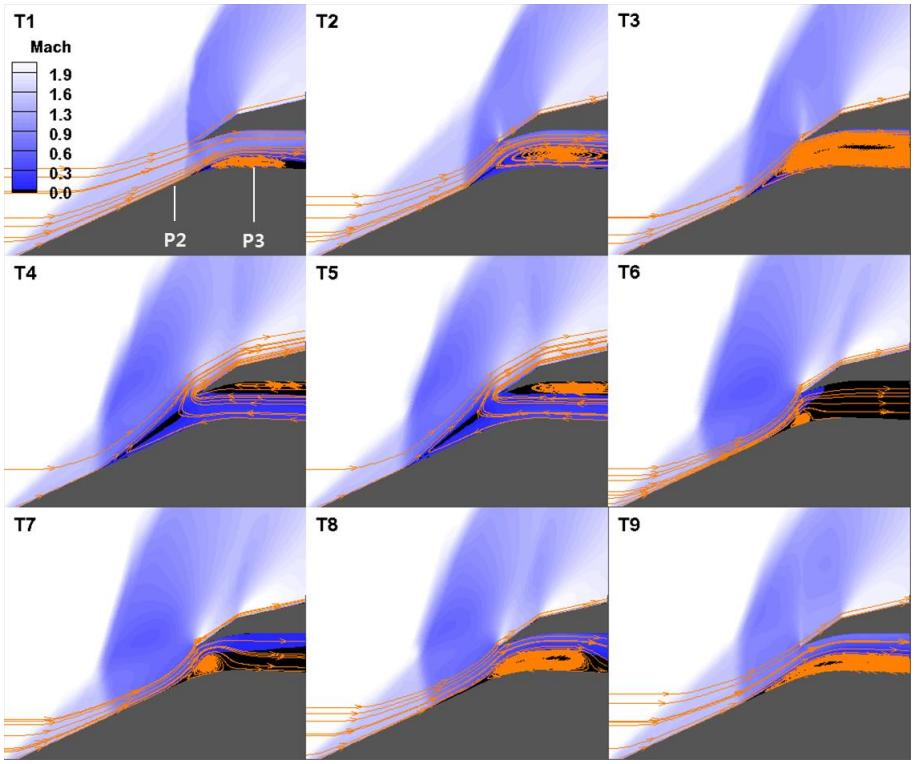

Fig. 17 Pressure history and FFT analysis at T.R = 0.67.

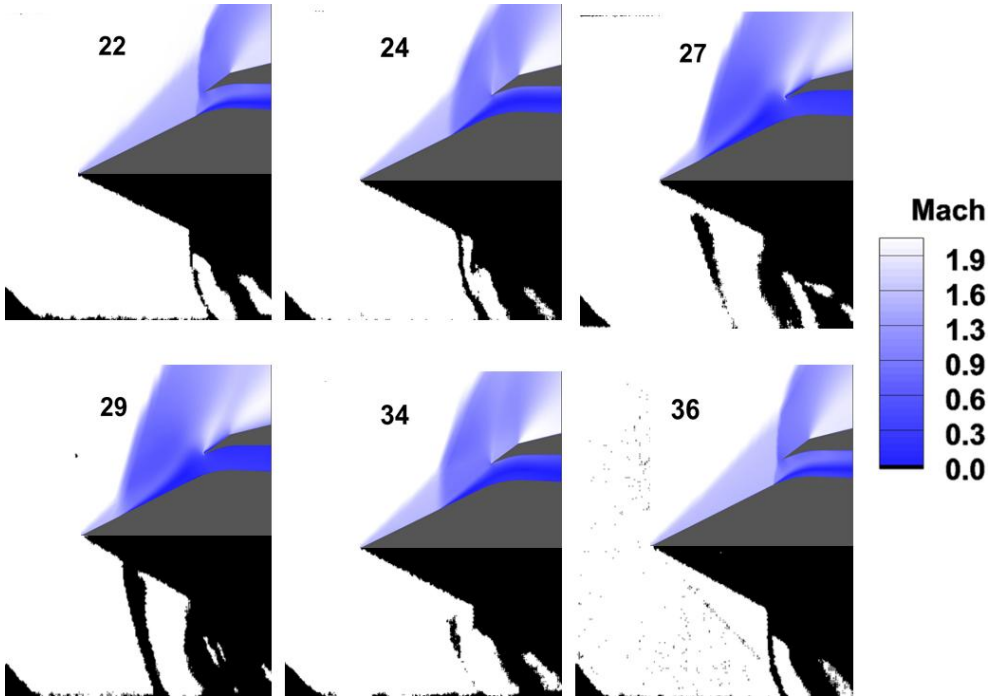

Fig. 18 Mach number distribution (upper half) and Shclieren image [4] (lower half) at T.R=0.67.

When the throttle area closes completely (T.R=0), then the pressure fluctuations are becoming more oscillatory as shown in Fig. 19a. a). Remarkably, the secondary peak of frequency is so excited that its amplitude is almost same as the dominant one in Fig. 19b. It seems a precursor of another inlet buzz transition. As it is different from the throttling ratio of 0.67, four kinds of vortexes are generated. Throat vortexes are shown in Fig. 20, T_1. The inner cowl vortex is in T_2, the compression surface vortex is in T4, and the outer vortex is shown in T5. Interestingly two different kind of vortex exists at same moment in T3, T5, and T6. In T3 and T6, even dual core vortexes are observed. In short, the state of inlet flow is extremely unsteady. As a result, many types of vortexes are created and vanish frequently because normal shock is expelled farther

upstream where the shock is extremely unstable. As the normal shock expels farther, the inlet flow is becoming more unstable.

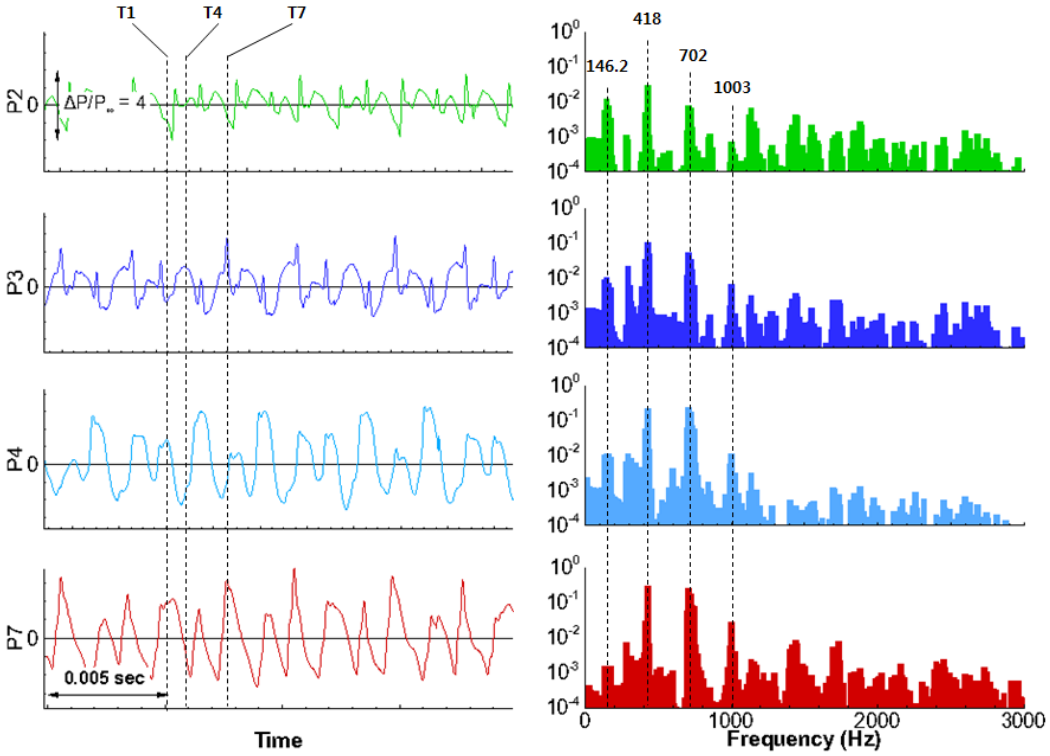

a) b)

Fig. 19 Pressure history and FFT analysis at T.R = 0.00.

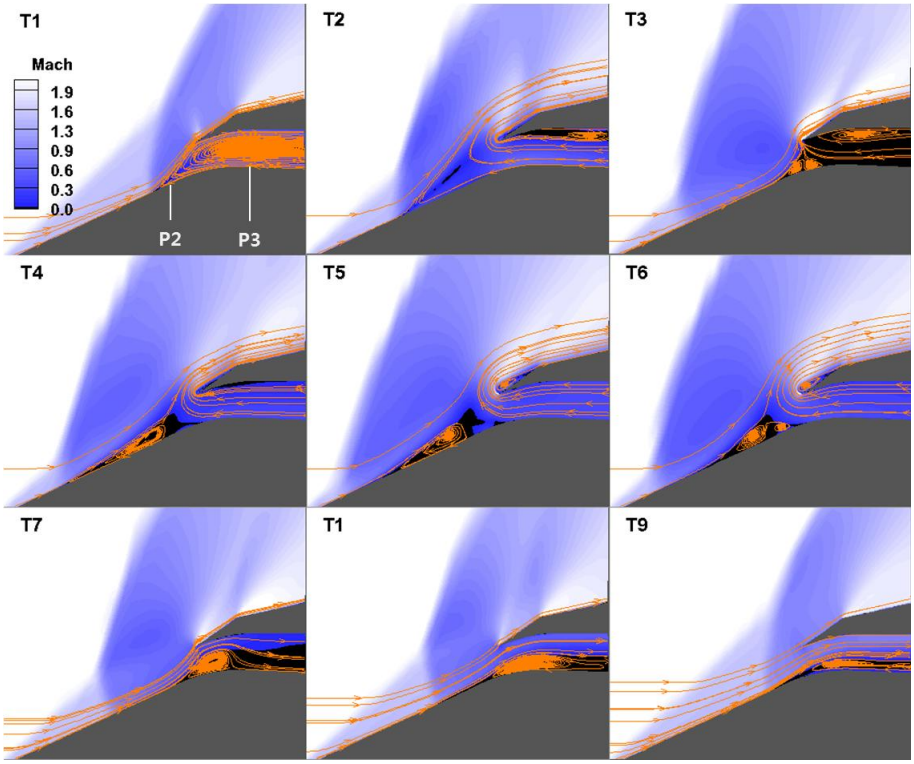

Fig. 20 Snap shots of inlet buzz sequence with Mach contour and flow pattern at T.R = 0.00.

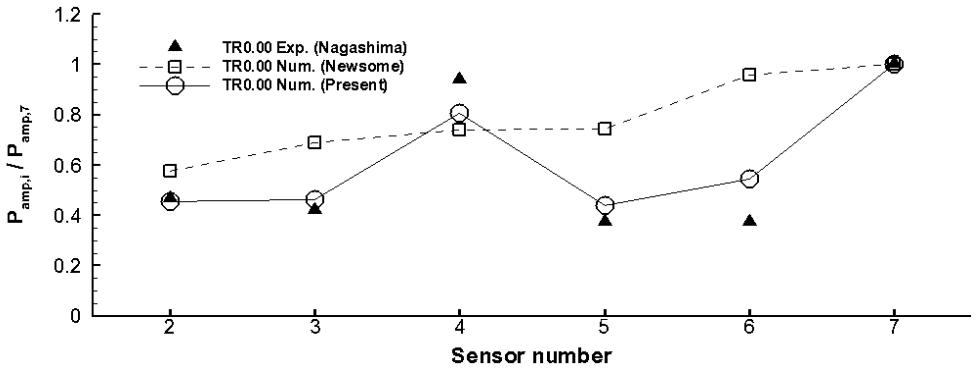

Fig. 21 Pressure amplitude of inlet buzz normalized by P7 value at T.R = 0.00.

Figure 21 depicts pressure amplitude of inlet buzz at each sensor. In this figure, the present computation result is validated with experimental data, and it

shows better agreement than Newsome's computation. The results at the small throttling ratios are summarized in Table 8

Table 8. Dominant frequencies at small throttling ratios in the decreasing T.R process.

T.R	Dominant frequency (Hz)	
	Computation	Experiment
0.67	367	360
0.55	376	376
0.35	390	386
0	418	391

In this set of computations, Case 2, several characteristics of inlet buzz that were observed in Nagashima's experiment are reproduced. In spite of the narrower effect of the exit, the dominant frequency is fairly predicted, including the harmonic series. Also, the increasing tendency of buzz frequency at the decreasing throttling ratio is observed. Moreover, amplitudes of pressure oscillation agree well with the experiment, and hysteretic transition of inlet buzz is reproduced by the present computation. From the next chapter, the counter path of throttling control is applied to observe inlet buzz behavior change under increasing mass flow rate condition.

4.3 Case3 - Inlet under Increasing Mass Flow (T.R) Con dition

The throttling ratio is increasing from the closed exit area (T.R = 0) to T.R = 2.41 in Case 3. The initial condition starts from the end state of Case 2 by exactly taking the reverse path of Case 2. As in Case 2, it is maintained for more than ten periodic flow cycles at every throttling ratio in Table 4.

Table 9. Dominant frequencies at throttling ratios in the increasing T.R process.

T.R	Computed dominant frequency (Hz)
0	418
0.21	700
0.35	624
0.55	619
0.67	617
0.79	611
0.97	606
1.14	120
1.42	115
1.62	104
2.41	0

Table 9 summarizes the computed dominant frequencies by increasing the throttling ratio. As the table reveals, the frequency jump is observed when the throttling exit is open to reach T.R = 0.21. Quite unexpectedly, the excited inlet buzz frequency almost maintains until the throttling ratio reaches T.R = 0.97. For example, as depicted in Fig. 22, the excited mode originated from T.R = 0.0 + is still consistent at T.R = 0.67, with the dominant frequency higher than 600 Hz. As a result, the overall inlet buzz in Case 3 behaves quite differently from that in Case 2. According to researchers' knowledge, there is no experimental and/or computational report on this type of buzz transition except for Dailey’s brief comment. Interestingly, Dailey conducted an experiment on a supersonic engine and an organ pipe with a similar throttling control to the present research and

observed that a sound with a higher pitch is suddenly generated when the exit is partially opened from the closed one. He reported, “The second mode of a closed end organ pipe 1.89 feet long is 460 cycles per second. This note was clearly audible. As the mass flow was increased (below the buzz range) the note suddenly increase pitch by a little less than an octave.” [2] Figure 23 shows the Mach contour and flow pattern at the throttling ratio of 0.67. Though the dominant frequency is high, only two types of vortices, the throat vortex and inner cowl vortex, are observed. This is closely related to the shock travel distance. In Fig. 24, the range between the maximum subcritical position by the expelled shock and the minimum subcritical position by the retreat shock is shown. From the large throttling ratio, the shock travel distance becomes longer as the throttling ratio decreases in Case 2. On the contrary, the shock travel distance in Case 3 becomes much shorter. This is able to maintain the high buzz frequency that originated from the opening phase of the closed exit, in spite of large throttling ratio and a lower back pressure. In other words, when the throttling ratio starts to increase from the closed end, the inlet buzz behavior is converted into a higher frequency mode with a shorter shock travel distance.

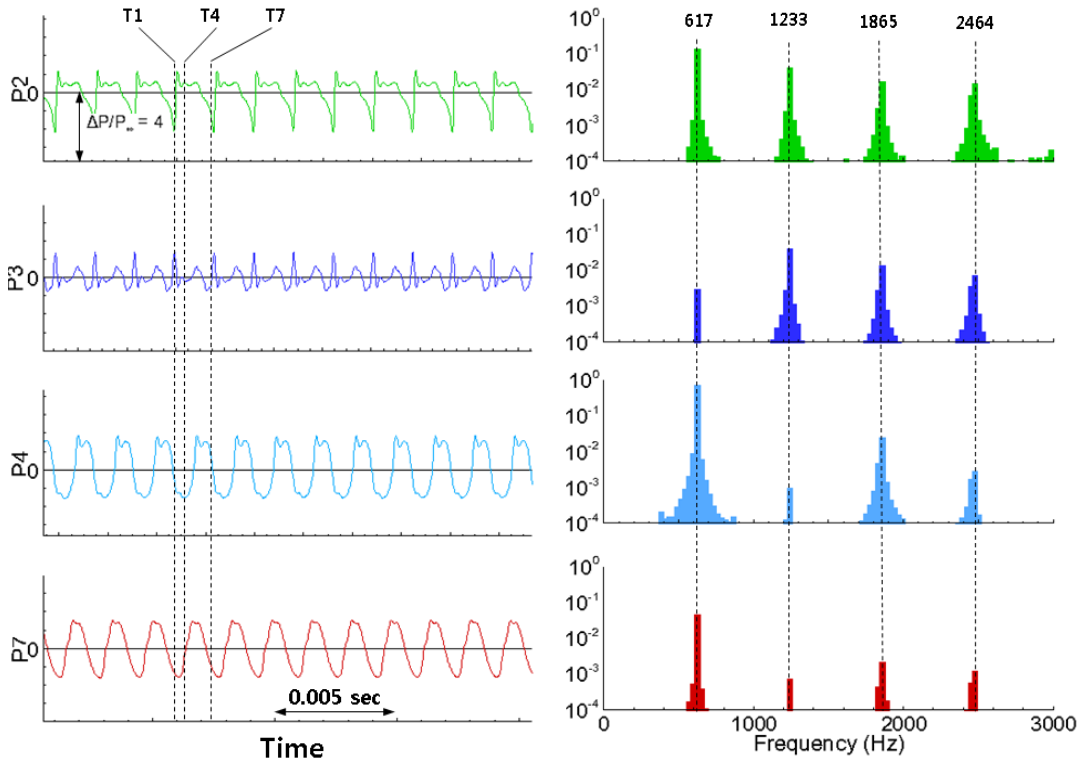

Fig. 22 Pressure history and FFT analysis at T.R = 0.67 in the increasing T.R process.

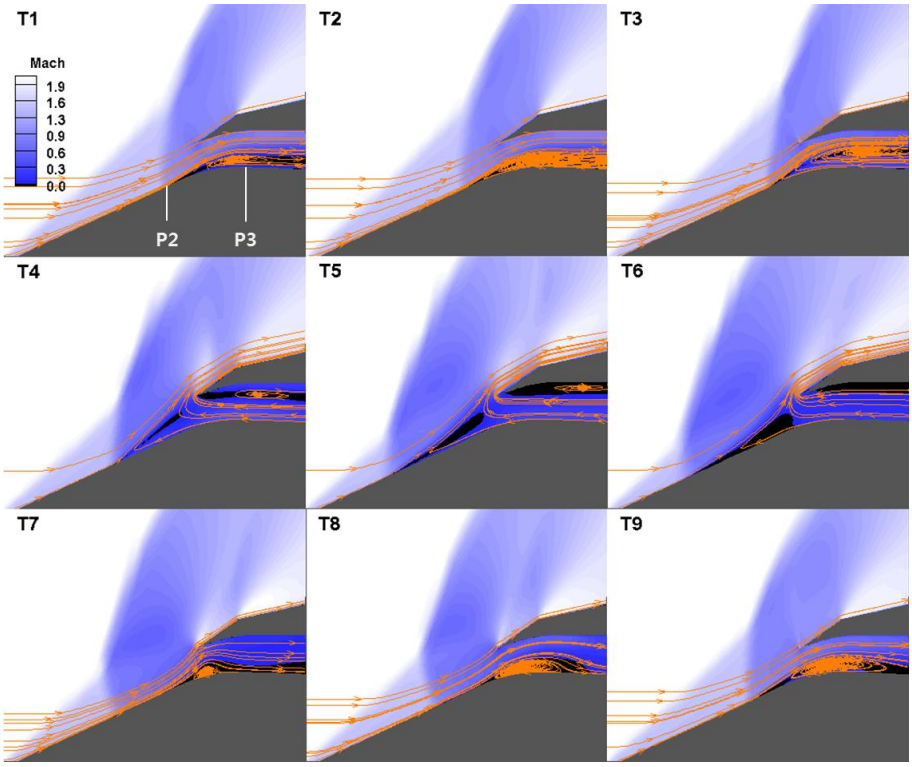

Fig. 23 Snap shots of inlet buzz sequence with Mach contour and flow patter n at T.R = 0.67 in the increasing T.R process.

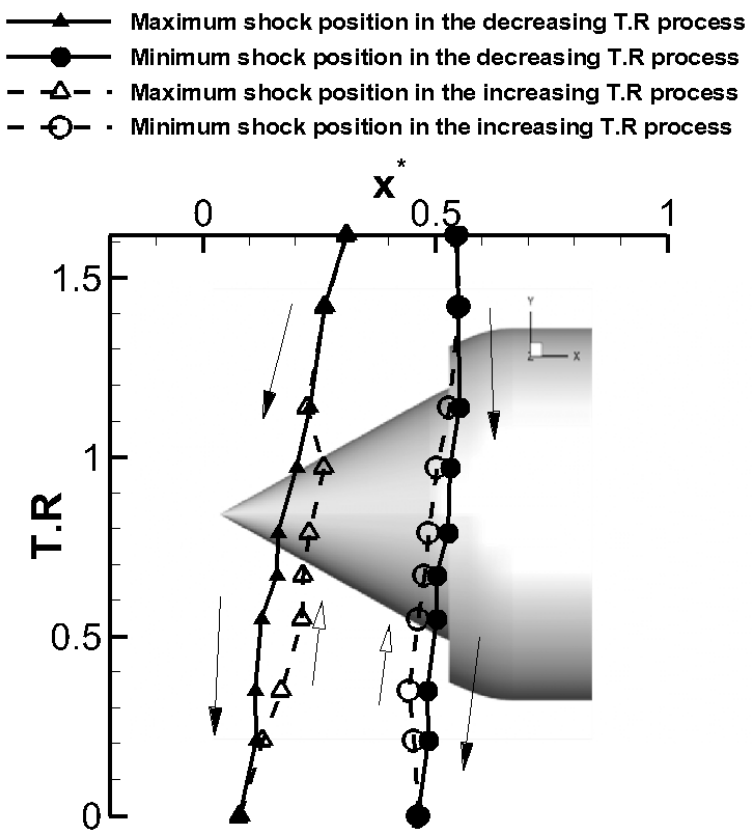

Fig. 24 Range of shock porition during an inlet buzz cycle (solid line : T.R decreasing process, dashed line : T.R increasing process, triangle : maximum shock position, circle : minimum shock position).

Figure 25 compares the pressure histories at the P2 sensor in Case 2 and Case 3. In the horizontal direction, the left end of the graph is the throttling ratio of 2.41 and the right end of T.R = 0.0. In the T.R decreasing process (Case 2), it goes left to right while it goes reversely in the T.R increasing process (Case 3). As shown in Figs. 25a and b, each history of Case 2 and Case 3 is clearly distinguishable from the other. Figure 26 shows more clearly the difference in buzz transition process. In Case 2, the buzz transition from the fundamental

mode ($N = 1$) to $N = 2$ occurs in T.R = 0.97 ~ 0.79, while the buzz transition from $N = 2$ to $N = 3$ occurs in T.R = 0.97 ~ 1.14 in Case 3. In other words, supersonic inlet buzz under a complete cycle of mass flow rate exhibits hysteretic characters accompanying a jump transition from the first to higher modes of the dominant frequency.

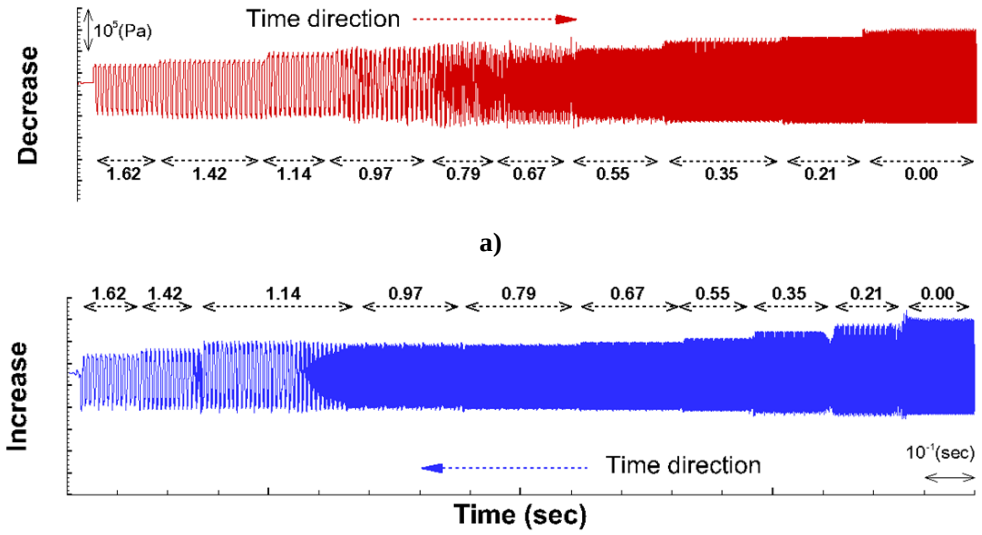

Fig. 25 Pressure history at P2 in the decreasing and increasing T.R process.

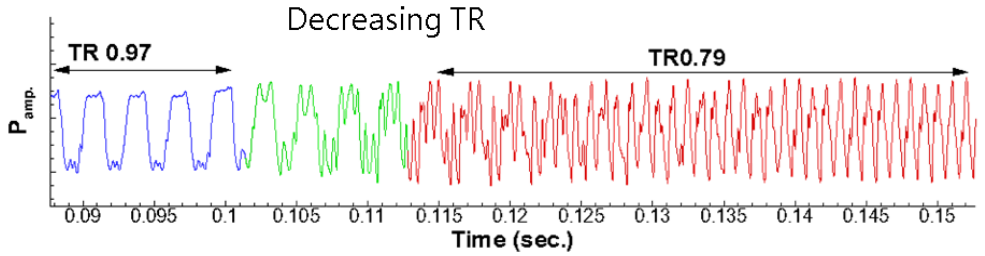

a)

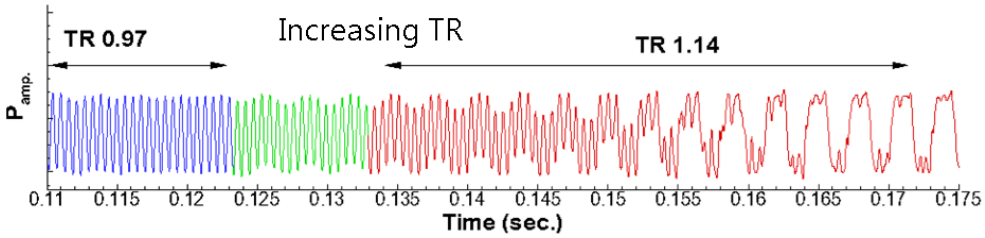

b)

Fig. 26 Pressure history of buzz transition in the decreasing and increasing T.R process.

4.4 Summary of Inlet Buzz Simulation Results with Mass flow control

The trajectory of the dominant frequency according to the complete history of the throttling ratio is summarized in Fig. 27. The dominant frequency can be classified into three groups: mode 1, mode 2, and mode 3. The number *N* in the figure indicates the mode number of Eq. 4.4 in Section IV. Depending on the behavior of the mass flow rate, three kinds of buzz transition exist. The first arises in the decreasing mass flow rate process of Case 2 and the others in the increasing mass flow rate process of Case 3.

Starting from the initiation of the fundamental mode, the dominant frequency slightly increases as the throttling ratio decreases. For T.R = 0.97 ~ 0.79, the first transition from the mode 1 to the mode 2 occurs, and the dominant frequency for mode 2 is more than three times higher than the fundamental mode

(mode 1) as shown in Fig. 27. Because of the axisymmetric shifting effect, there is a slight difference in the first transition between computational prediction and experimental observation.

From T.R = 0.79 to 0, the dominant frequency increases slightly with maintaining the mode 2. If the exit is blocked and the throttling ratio becomes zero, the process moves from Case 2 to Case 3. When the throttling exit starts to open, the dominant frequency jump appears again with the second buzz transition. After that, it maintains high frequency until T.R reaches 0.97. During the throttling ratio of 0.97 to 1.14, the third buzz transition occurs with the dominant frequency down to the mode 1. Consequently, inlet buzz shows hysteretic characteristics along its historic path as shown in Fig. 27.

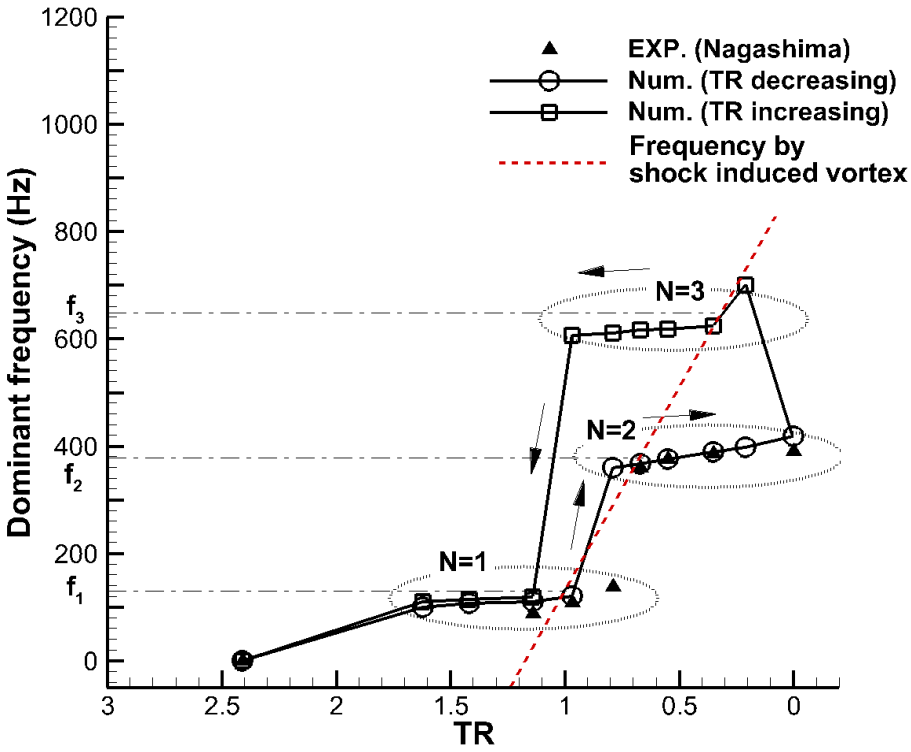

Fig. 27 Trajectory of the dominant frequency under a complete historic path.

The dashed inclined line is the frequency of wave caused by the shock induced vortex. This line connects the modes of frequency point (f_1, f_2, f_3) on the inlet buzz frequency trajectory. Just like the modified vortex line in Fig. 3, the line means that the shock induced vortex is more excited as the throttling ratio decreases and triggers the buzz transition. Unlike the edge tone of instrument, it is impossible to consider that the isolated front parts (cowl and compressor part of center body) of the inlet that generate the vortex successively because the vortex generation depends on the downstream condition of the inlet diffuser part or resonator. It is not certain that the dashed line of frequency caused by shock induced vortex in Fig. 27 is the first slope or higher order of curve, but it is certain that the frequency of the vortex is in a reversed proportion to the throttling ratio.

Several evidences that the inlet buzz phenomena come from acoustic sources are found from these results. The fundamental frequency of inlet buzz is estimated by Eq. 4.4, which is from the flow oscillation of the closed pipe theory. The FFT analysis results show that the harmonic series and the vortices are visualized in the front part of the inlet that has been known as the sounding source of wind instruments. By this acoustical basis, the hysteretic characteristics can be approached in acoustical point of view.

4.5 Hysteretic Behavior of inlet buzz with Varying Mass Flow Rate

As summarized before, inlet buzz characteristics change hysteretically under varying mass flow rates. Though, this phenomenon was observed in many of precedent researches, there is not a clear understanding or explanation for it. Dailey and Nagashima commented that it may have a relation with acoustic

fundamentals. In this chapter, a hypothesis is confirmed using similarities between inlet buzz and musical instrument and some of evidences found to support The hypothesis. The target phenomena to explain are two as follows:

The first transition that the dominant frequency jumps from the mode 1 to the mode 2 at the decreasing process of throttling ratio.

The second transition that the frequency jumps from the mode 2 to the mode 3 turns out at the beginning of opening the blocked exit.

The hypothesis for these buzz transitions is the following:

The inlet buzz transition is one of the overblowing phenomena caused by self-sustained vortex induced vibration.

In the followings, the basis for the hypothesis is suggested, and the inlet buzz characteristics around transition point are detailed.

4.5.1 Required factors for overblowing

In order to have overblowing in musical instrument, three conditions are needed: acoustic disturbance, a resonator, and positive feedback interaction. By comparing the instrumental sounding mechanism with Fig. 3 in Section 2.2 to the hysteretic inlet buzz transition behavior with Fig. 27 in Section 4.4, one may find a one-to-one correspondence.

Various vortices, which are generated at inlet front, play a role as an edge tone. They constantly serve disturbance acoustic waves to the inlet diffuser, or in

terms of instrumental acoustics, the resonator. The inlet diffuser resonates with the disturbance waves from the vortices. Similarly, the throttling ratio acts as the jet velocity. By assuming these matching roles, the resonant mechanism of inlet buzz can be explained as following steps. At the first step, the decrement of the throttling ratio brings more flow instability as the stronger jet velocity does to musical instrument. As the flow field gets more unstable, more vortices are generated by stronger shock oscillations. Four types of vortices (throat vortex, inner cowl vortex, compression surface vortex, and outer cowl vortex) observed in Case 2 and Case 3 are schematically presented in Fig. 28. The vortex types are named after the location where they are originated.

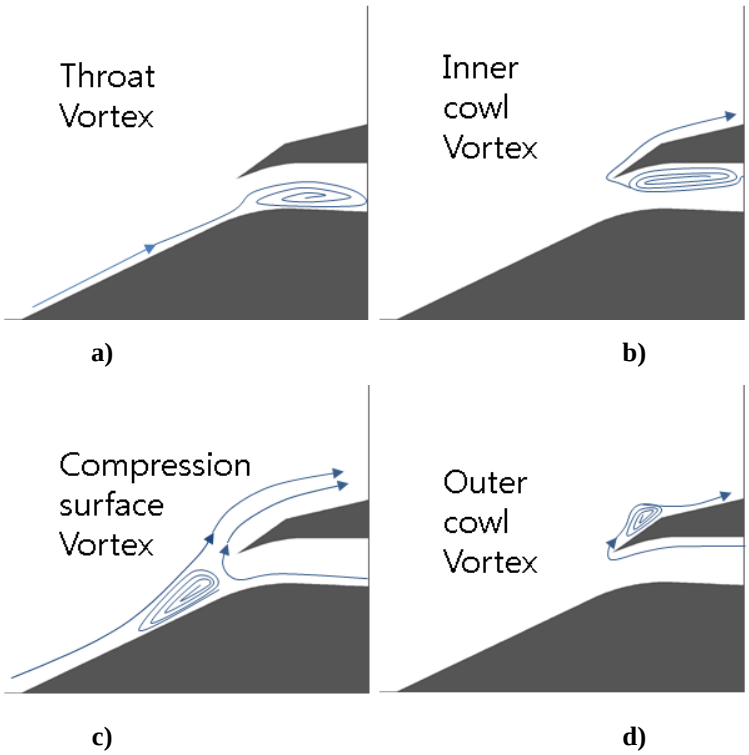

Fig. 28 Schema of the four shock-induced vortices.

1) A throat vortex is created at the inlet throat area when the local flow is under inflow condition. The normal shock in front of the inlet causes the boundary layer at the compression surface to become thicker. The decelerated flow in the boundary layer passing the inlet throat is eventually separated to generate vortex at throat area. The throat vortex reduces the effective throat area and provides acoustic disturbance

2) The inner cowl vortex is generated under a reverse flow condition that is formed by the high pressure field inside the inlet. From the view point of the reverse flow, the inner cowl surface is concave, and the curved cowl lip acts as a compression ramp; therefore, the local flow near the inner cowl surface is trapped to form a vortex. The inner cowl vortex vanishes at the end phase of the reverse flow.

3) The compression surface vortex is observed in the high frequency buzz process. As the throttling ratio decreases, the back pressure goes up, and the normal shock is expelled on the upstream compression surface. From the shock leg on the compression surface, a separation vortex grows up to form compression surface vortex. It is maintained until the normal shock retreats.

4) The vortex at the outer cowl surface near the cowl lip turns up just after the reverse flow starts. At the beginning of the reverse flow, a strongly emitted stream from the inlet and a subsequent strong suction on the outer cowl surface produces a separated flow to form outer cowl vortex. This vortex exists for a short time and does not contribute much to the buzz excitation, but its occurrence indicates that the buzz is quite intensive in high frequency range.

All four vortices interact with the flow conditions or unsteady shock motions and generate acoustic disturbances [2, 6]. The vortices generate pressure wave by moving shock position and by being an acoustic wave source

itself. As shown in pressure histories and shock position in Figs. 12, 14, 16, 19, and 22, a large pressure amplitude ($\Delta P/P_\infty > 4$) is produced by shock moving. The throat vortex and the compression surface vortex, which are generated after the terminal shock leg, therefore, are directly involved in shock instability. The terminal shock is moved upstream by the throat vortex or the compression surface vortex. Next, the changed captured ratio results in varying mass flow rate, pressure, and Mach number. On the other hand, the outer cowl vortex and the inner cowl vortex hinder the retreating motion of the terminal shock during the reversed flow phase. By this behavior, pressure fluctuation is also generated. Consequently, the four vortices generate the pressure wave; especially, the throat vortex and the compression surface vortex are mainly engaged in moving the terminal shock.

4.5.2 Vortex role for resonation and relation with throttling ratio

If the frequent interaction between vortex and inlet results in a positive feedback mechanism as in the case of instrumental acoustics in Section II, it leads to inlet buzz resonation. It is noted that the dash-dot straight line in Fig. 3 obtained by connecting the mode frequencies of the organ pipe is quite similar to the frequency line obtained by connecting the modes of the dominant inlet buzz frequency. Judging from the fact that the mode of the dominant inlet buzz frequency can be estimated from the equation Eq. 4.4 of the mode frequency for open and closed pipes and the fact that the four vortices generated from the shock-boundary interaction provides the same acoustic disturbance as an edge tone in Fig. 3, the two straight lines in Fig. 3 and Fig. 27 are the results of vortices providing acoustic disturbances (Fig. 3 for edge tone vortex and Fig. 27

for the four vortices). Thus, the overblowing mechanism can be applied to explain buzz transition process and hysteretic inlet buzz phenomena.

Figures 13, 17 and 20 show a set of sequential frames of an inlet cycle at the throttling ratio of 1.14, 0.67 and 0. As the throttling ratio decreases, a different type of vortex is added, and the frequency of the vortex generation becomes shorter. At the large throttling ratio, just one type of vortex, the throat vortex, is generated in a whole buzz cycle as shown in Fig. 13. At T.R = 0.0, however, all four types of vortices appear and vanish frequently as in Fig. 20. Without a center body inlet as in Case 1, the vortex is not generated, and pressure oscillation is not evolved into the second mode but stays in the first mode. It tells that the vortex frequency is in reversely proportion to the throttling ratio, and the formation and evolution of vortex plays a significant role in inlet buzz resonation. Based on the observations, the inlet buzz transition can be regarded as an overblowing phenomenon triggered by shock-induced vortices.

In order to check sound generation characteristic depending on the mode of the dominant frequency, the SPL trajectory is compared in Fig. 29.

$$SPL(dB) = 20\log_{10}(\frac{P_{rms}}{2\times10^{5}}),\ p_{rms} = \sqrt{\frac{\sum(p - p_{mean})^2}{N}} \tag{3.85}$$

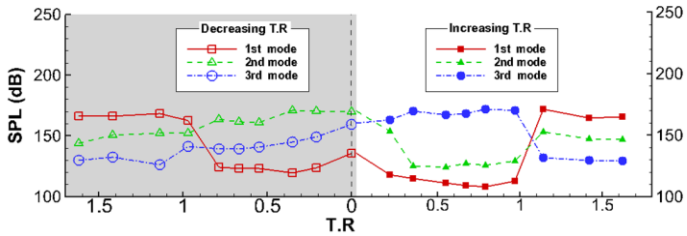

Fig. 29 Trajectory of sound pressure level of three frequency modes under varying throttling ratios.

The first mode of the dominant frequency is in range of 100~150Hz, the second mode is in 350~400Hz, and the third mode is in 600~700Hz. The SPL behavior in the second buzz transition (T.R = 0.0+) shows that the dominant frequency changes from the second mode to the third mode as shown in Fig. 29. This change is consistent to Dailey's experimental result that a highly pitched sound could be observed at this point. The hysteretic character affects the total pressure recovery as shown in Fig. 30 because more frequent flow oscillation incurs more viscous induced loss. For example, the total pressure of the mode 3 is less than that of the mod2. A hysteretic inlet buzz is a kind of vortex-resonator interaction shares many common characteristics with instrumental acoustic phenomenon. By adopting an instrumental acoustic point of view, fresh tactics to avoid inlet buzz can be considered.

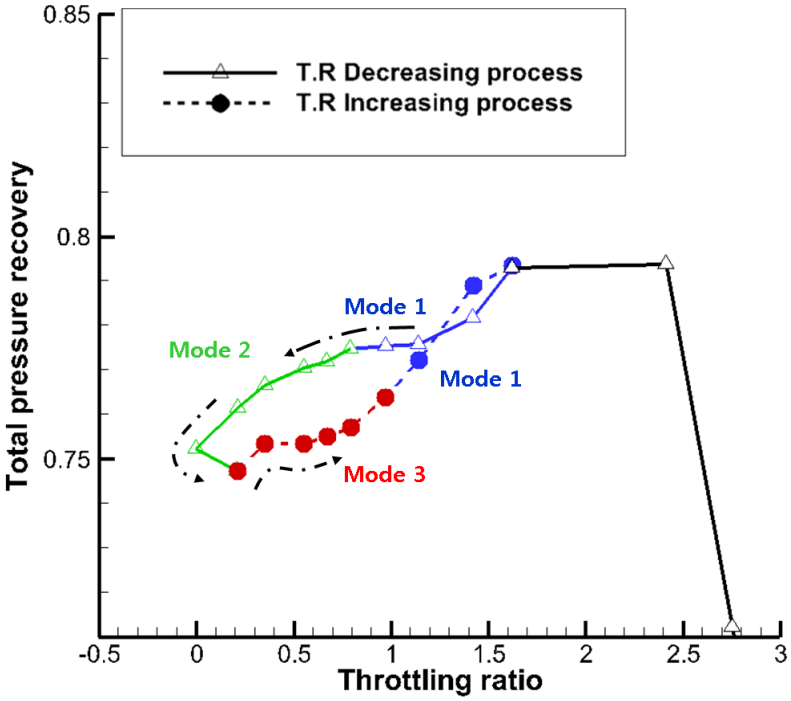

Fig. 30 Trajectory of mean total pressure recovery during an inlet buzz cycle under varying throttling ratios.

Chapter V
Inlet Buzz Simulation at Angles of Attack

Nagashima's configuration is designed for Mach number 4.0 and the pressure distribution of computation at the design Mach number is shown in Fig. 31 a). The oblique shock heats the cowl lip and deflects into the internal inlet, resulting in a couple of reflections at the inner cowl and the center body surfaces. On the other hand, the experimental Mach number is 2.0, and the computational result is shown in Fig.31 b).

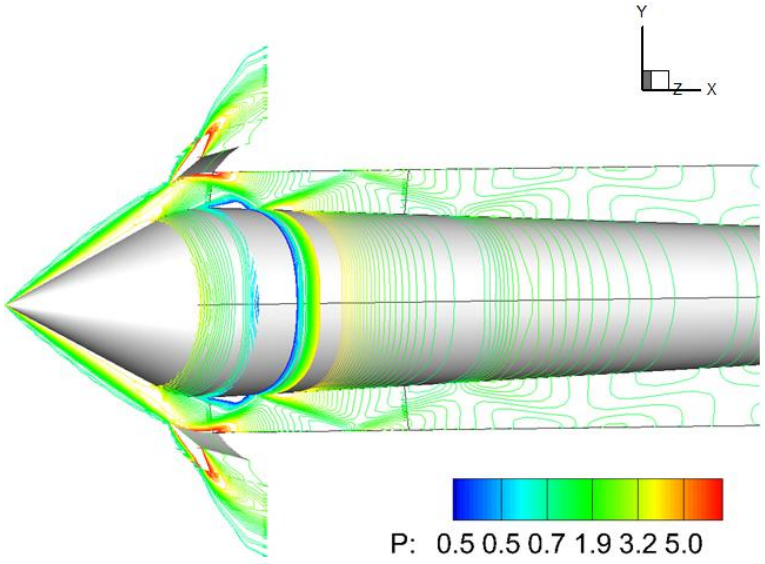

a) Pressure distribution at Mach 4.0, T.R = 2.41, AOA = 0°

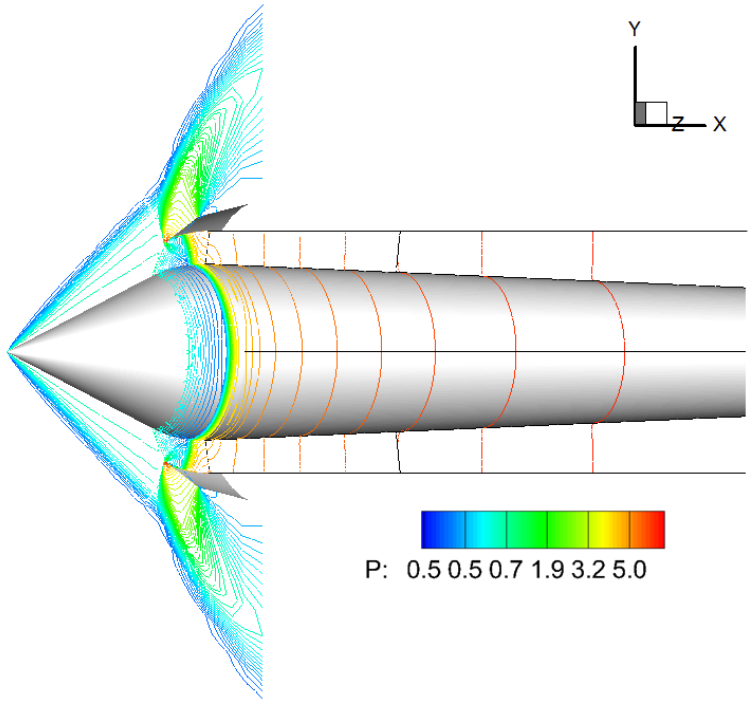

b) Pressure distribution at Mach 2.0, T.R = 2.41, AOA = 0˚

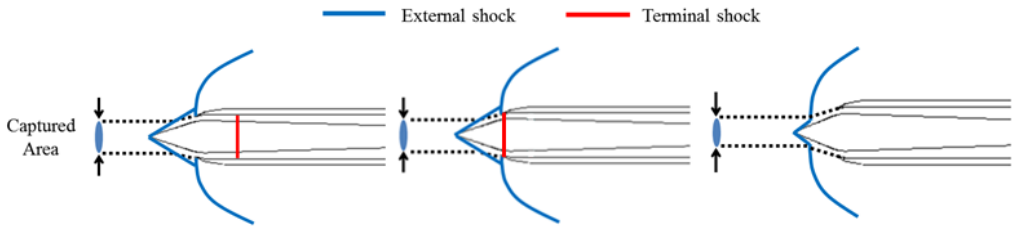

c) Supercritical **d) Critical** **e) Subcritical**

Fig. 31 Pressure distribution and schematic images at each flow condition of supersonic inlet.

At Mach number 2.0, the oblique shock angle is so large that the shock passes the front of the cowl lip, as depicted in Fig.31b. From the basic formation of the shock structure, the normal shock moves forward or backward, for the back pressure condition is varied. Depending on the terminal shock position, the

flow regime of the supersonic inlet can be clearly distinguished, as shown in Fig. 31c,d, and e. In general, when the terminal shock is on the cowl lip, it is called critical condition, and when the terminal shock is more toward downstream than cowl lip, it is called supercritical condition. If the terminal shock is out of the inlet, as shown in Fig. 31e, the flow regime is called subcritical condition. Because the inflow Mach number is 2.0 in this study, the basic shock structure of all the simulations is like the one in Fig. 31b.

5.1 Steady State Simulation at T.R 2.41

For the steady state case, both inviscid and viscous simulations are conducted. The same numerical methods explained in the previous section are adopted to solve the three dimensional Navier-Stokes equations, and the total number of mesh is increased to nearly four million to satisfy wall resolution criteria. Internal grid dimension is 250(axial) by 70(radial) by 80(axis-rotational), and the turbulent non-dimensional first step size adjacent to the wall is typically y^+=1. In addition, k-ω SST model [16] is used to take into account the turbulence effect. Fig. 32 compares inviscid and turbulent flow simulation results for the Mach 2.0 and throttling ratio 2.41 condition. In this case, the throttling ratio is large enough to pass all of the captured air through the engine internally; therefore, pressure oscillation does not occur. The curves in Fig. 32 indicate static pressure at the center-body surface along longitudinal direction. It demonstrates that different recovery behavior appears at the throat area. Afterwards, the difference is maintained to the end of the center-body. Consequently, static pressure at the plenum chamber has different quantity between inviscid and viscous simulations as listed in Table 10.

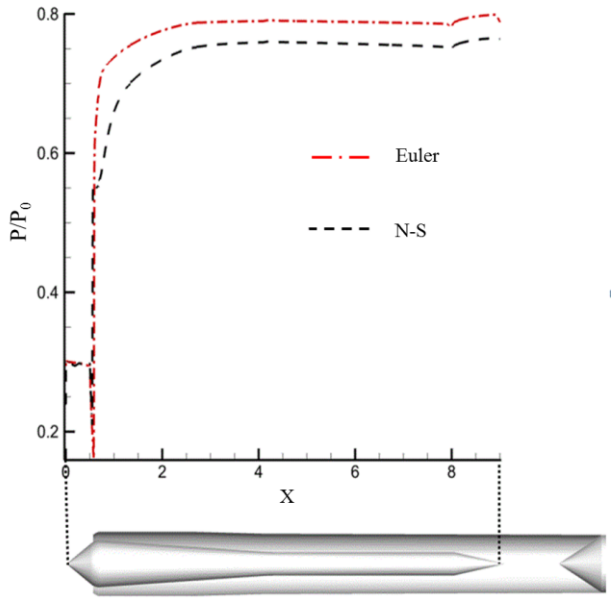

Fig. 32 Static pressure recovery curve on the center-body surface along the longitudinal direction (Mach 2.0, T.R = 2.41, AOA = 0°)

Table 10. Plenum chamber pressure at P7 ($P_{P.C}$: static pressure in plenum chamber, P_0 : total pressure in settling chamber[4]).

Method	Experiment [4]	Computation (N-S)	Computation (Euler)
$P_{P.C}/P_0$	0.30	0.33	0.37

This table shows that even the viscous simulation is different from the experimental quantity because the grilled type exit of the plenum chamber in the experiment is simplified as a continuous radial band type with maintaining an area for simulation [4]. Pressure contours are shown in Fig. 33.

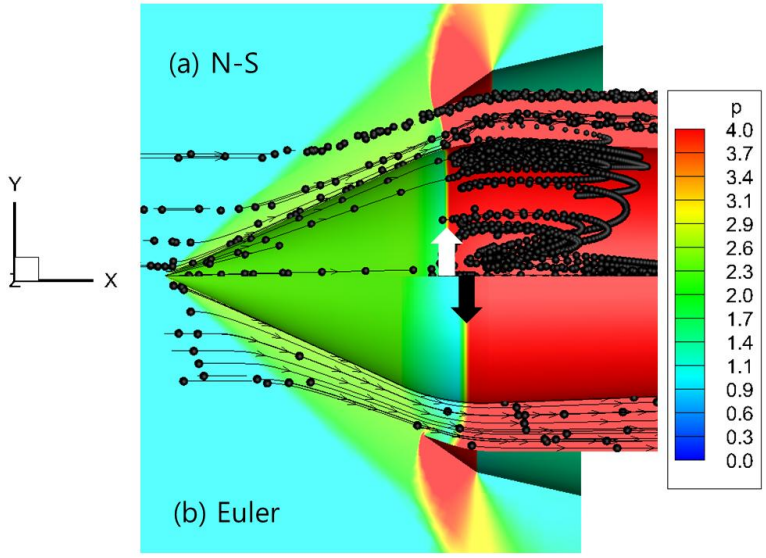

Fig. 33 Comparison of Mach number distribution around throat area

The viscous simulation result clearly shows the SWBLI induced vortex at the throat. This vortex is the main source for the pressure loss, and eventually creates a discrepancy between inviscid and viscous results. In addition, this vortex narrows the throat area and causes throat chocking earlier. The terminal shock near the cowl lip moves upstream because the throat area is decreased because of the vortex. Because of viscous effect, the viscous simulation shows the vortex near the cowl lip, 6% lower pressure recovery, while all the simulations have the same external shock structure and common trend of pressure recovery as shown in Figs. 32 and 33.

5.2 Inlet Pressure Oscillation Simulation with Zero Angle of Attack

To examine inlet the pressure oscillation behavior according to the throttling ratio, the simulation was conducted with zero angle of attack. From the result of the zero throttle-area case (T.R=0), an FFT analysis was carried out using pressure history data in each sensor. The dominant frequency is 133.108Hz when the physical time step of the simulation is 25μsec. The physical time step is gradually controlled from the initial value of 25μsec to the final value of 100μsec. The dominant frequencies are distributed in a span of 133.031±0.032Hz. Because it is short enough to predict a dominant frequency, 25μsec is adopted for the physical time step to capture instantaneous frames clearly in the high frequency pressure oscillation cycle. Figure 34 shows shock movement and the pressure fluctuation at P1 and P3 sensors for the throttling ratio of zero. The P1 position is near the front line of the shock-expelled range, and P3 is at the throat, which is the rear limit of terminal shock at the supercritical condition. Because the pattern of recorded pressure histories at P1 and P2 are almost the same, pressure data at P1 and P3 are presented. The frames from T1 to T8 are a sequence of a pressure oscillation cycle. At the beginning of the cycle, T1, it is a supercritical condition, and internal pressure is increasing because of the blocked exit (T.R is 0). The high pressure region, therefore, is expanded upstream-wise, and by the time it reaches the cowl lip, the flow regime suddenly switches from a supercritical to a subcritical condition, as shown in Fig. 34, T2. During the time interval of T3 to T4, the shock passes the sensor position with a step-like pressure jump. The shock moves so fast that the flow regime instantly switches from a supercritical to a subcritical state. In the subcritical condition, the back-pressure wave is still moving upward, and the

oblique shock and the bow shock interact with each other. After all, the bow shock is detached from the tip of the center-body cone. During this shock forwarding process, from T1 to T4, the captured ratio is decreased, and high back-pressure is relieved with emission by reversed flow. The next stages from T5 to T8 are the shock retreat process. The captured area increases as the shock moves downstream and the flow regime returns to the supercritical condition. From T8, after a while, the internal pressure rises, and the flow structure becomes that in T1 again; therefore, one pressure oscillation cycle is over and then repeats itself. . Though this flow oscillation is brought about by the small throttling ratio (mass flow rate condition) without viscous effect, its behavior is similar to the general inlet pressure oscillation sequence that has been well documented in previous studies.

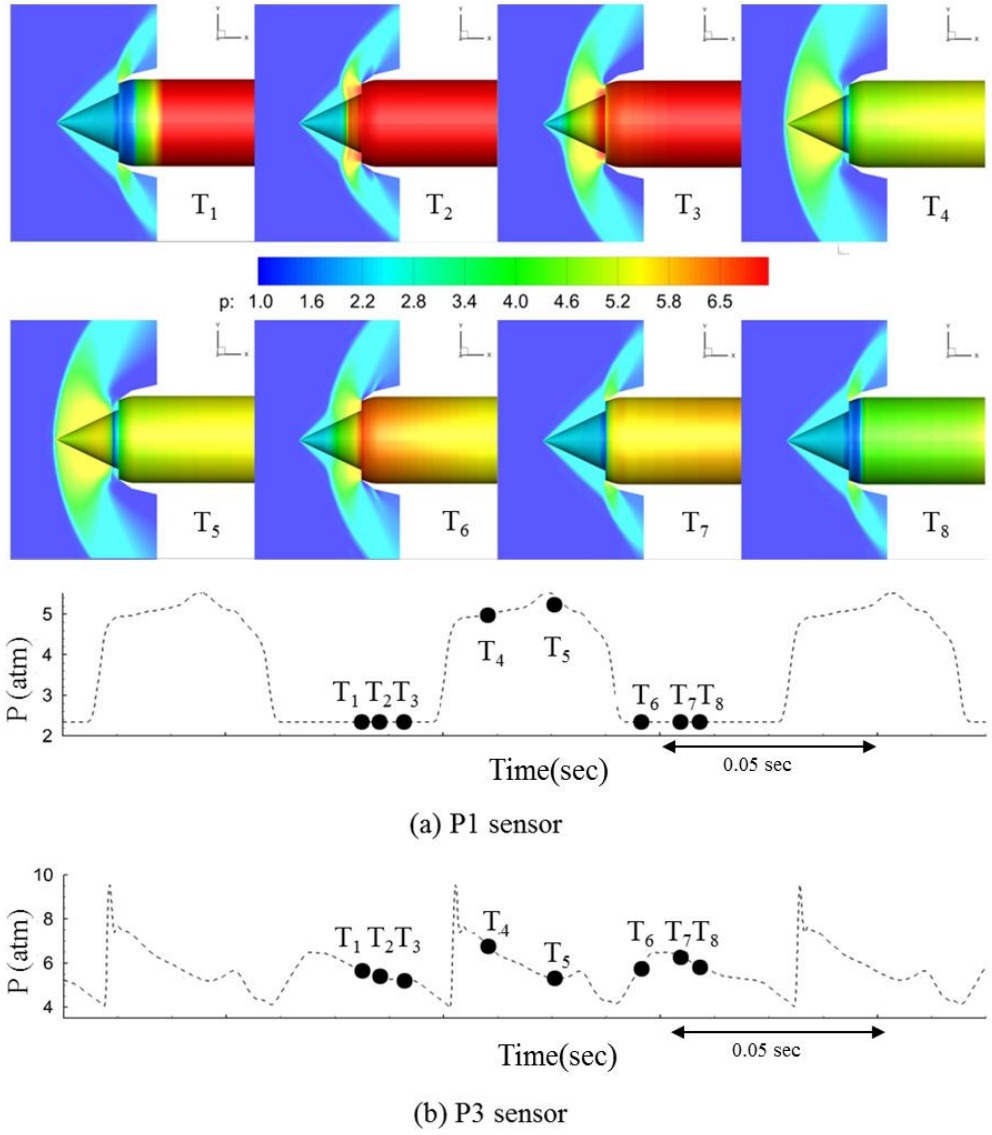

Fig. 34 Pressure oscillation sequence in the pressure oscillation cycle and pressure history at P1 and P3 sensors

Figure 35 depicts the dominant frequency variation with different throttling ratios. The variation is compared to the experiment and turbulent flow simulation results [25]. Current inviscid results show that steady state of inlet flow at the throttling ratios that are larger than or equal to 0.79. Because there is

no boundary layer, the effective area of inlet internal is larger than the real area. When the throttling ratio is 0.67, the throttling exit is choked. From here, the phase of charging the mass flow inside the inlet with rising chamber pressure and emission phase repeats alternately. The predicted dominant frequencies distribute at the range from 120Hz to 133Hz, and it is much lower than the viscous simulation and the dominant frequency. The frequency coincides with the fundamental mode of frequency estimated by Eq. 4.4. Because there is not a pressure disturbance source, such as a shock induced vortex in viscous simulation as mentioned at section IV, the frequency stays around 130Hz without any excitation.

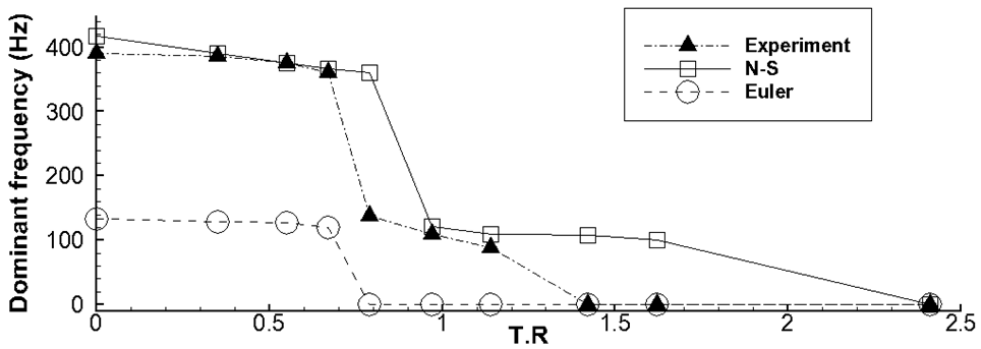

Fig. 35 Variation of dominant frequency along the throttling ratio.

The comparison studies between inviscid and turbulent flow simulations show that although there are some quantitative differences, inviscid flow calculation predicts well the external shock structure and the tendency of pressure oscillation frequency. In the meantime, the turbulent flow simulation takes approximately 10 to 20 times more computational cost than the inviscid one. Thus, in the next step, we decided to perform inviscid flow calculations to

study the qualitative flow behavior around the inlet. In fact, it was found that the inviscid calculation was efficient to examine the basic characteristics of asymmetric oscillating flow with a non-zero angle of attack.

5.3 Inlet Pressure Oscillation Simulation with Moderate Angle of Attack

In this section, the effects of different attack angles on the pressure oscillation phenomenon are studied. The attack angles of 3°, 5°, 7°, and 10° are chosen. Table 11 lists the dominant frequencies varying with different angles of attack. Although the attack angle increases, the frequency is nearly stationary at around 133Hz, thus the pressure oscillation frequency is also not that sensitive to the attack angle. This tendency has already been reported by precedent experimental studies (4, 33, 34, and 35). Figure 36 shows the sequence frames in a pressure oscillation cycle at a 10° angle of attack and a 0 throttling ratio. The sequence is similar to Fig. 34 when the asymmetric shock structure is observed.

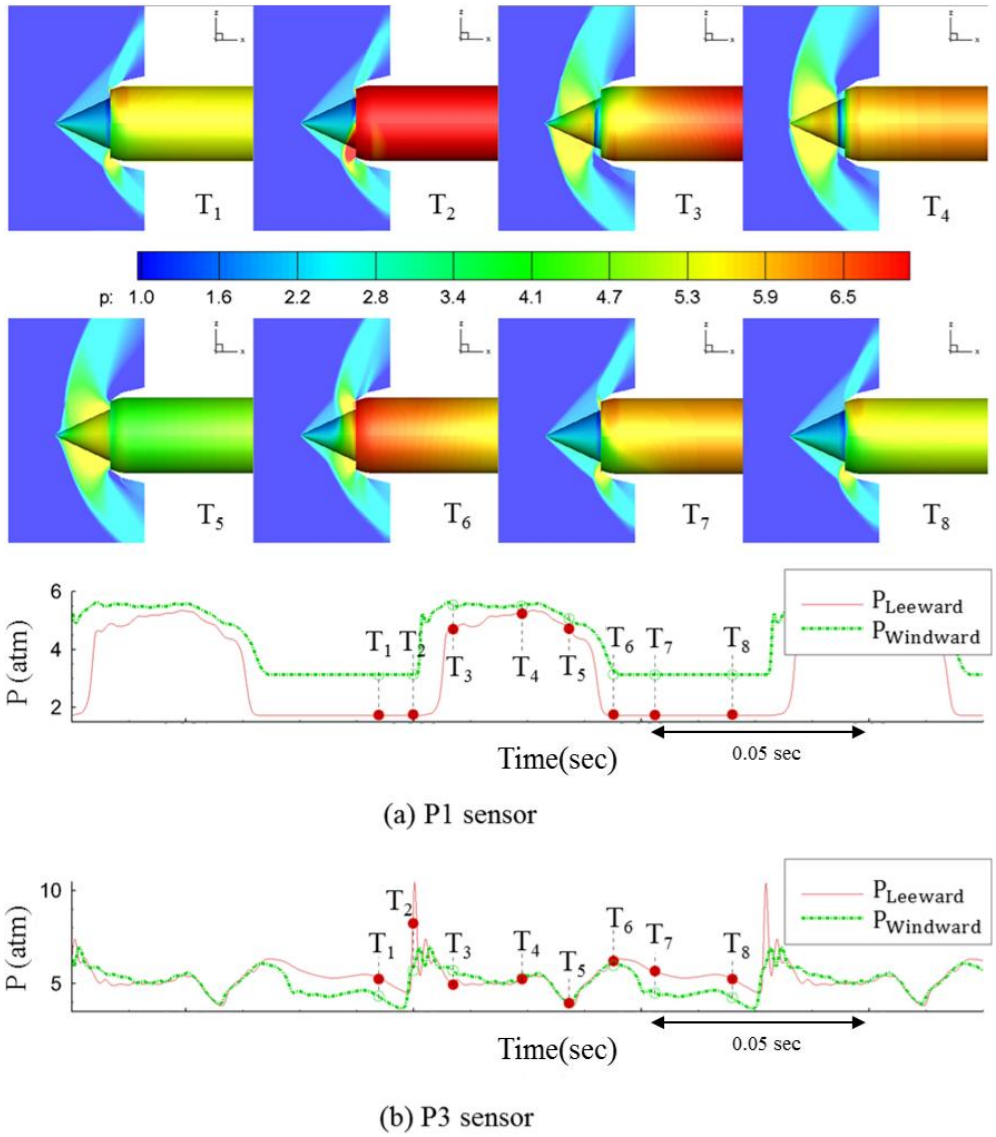

Fig. 36 Pressure oscillation sequence in the pressure oscillation cycle and pressu re history at P1 and P3 sensors of wind/leeward side (Mach 2.0, T.R=0, AOA= 10°).

Table 11. Dominant frequency variation along the angle of attack at throttling ratio 0.

		AOA				
		0°	3°	5°	7°	10°
T.R = 0	Frequency (Hz)	133.606	133.892	133.391	133.035	133.248

Because the oblique shock strength at the windward side (lower half) is stronger than the leeward side (upper half), pressure at windward rises greater than it does on the other side. It is supported by pressure history curves at the bottom of Fig. 36, which are measured at the P1 and P3 position. In the shock forwarding process (T1 to T4), the shock in the leeward side moves out later than the shock in the other side. Using the Taylor-Maccoll [36] equation, asymmetric oblique shock angles can be predicted. However, the asymmetric bow-shock structure in the T4 frame of Fig. 36 and desynchronized shock oscillation need to be explained further. Figure 37 presents the Mach contours and stream lines at a critical condition when there is no angle of attack (T7 frame in Fig. 36) and when the throttling ratio is 0, which is T7, one of the frames in Fig. 36. The normal shock remains at cowl lip in both the windward and leeward side. On the other hand, Fig. 38 shows the asymmetric shock structure. This is from the T7 time frame in Fig 36.

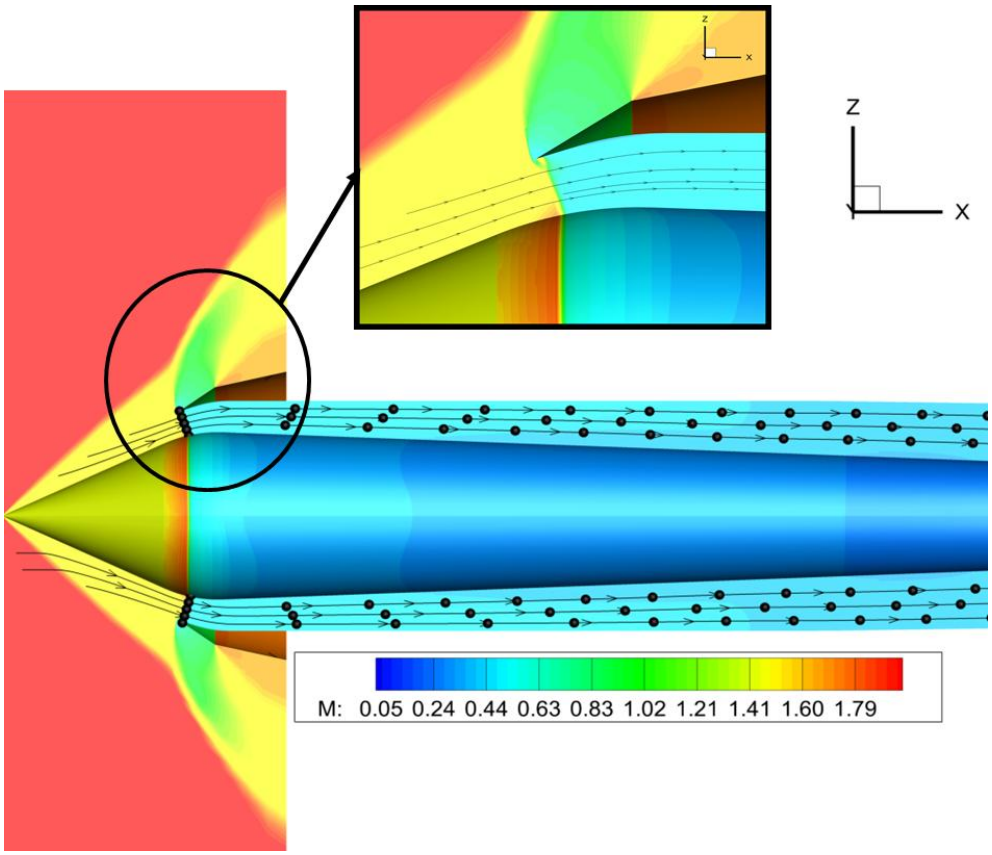

Fig. 37 Mach contour and stream line at the T7 frame in Fig. 6 (Mach 2.0, T. R=0, AOA=0°).

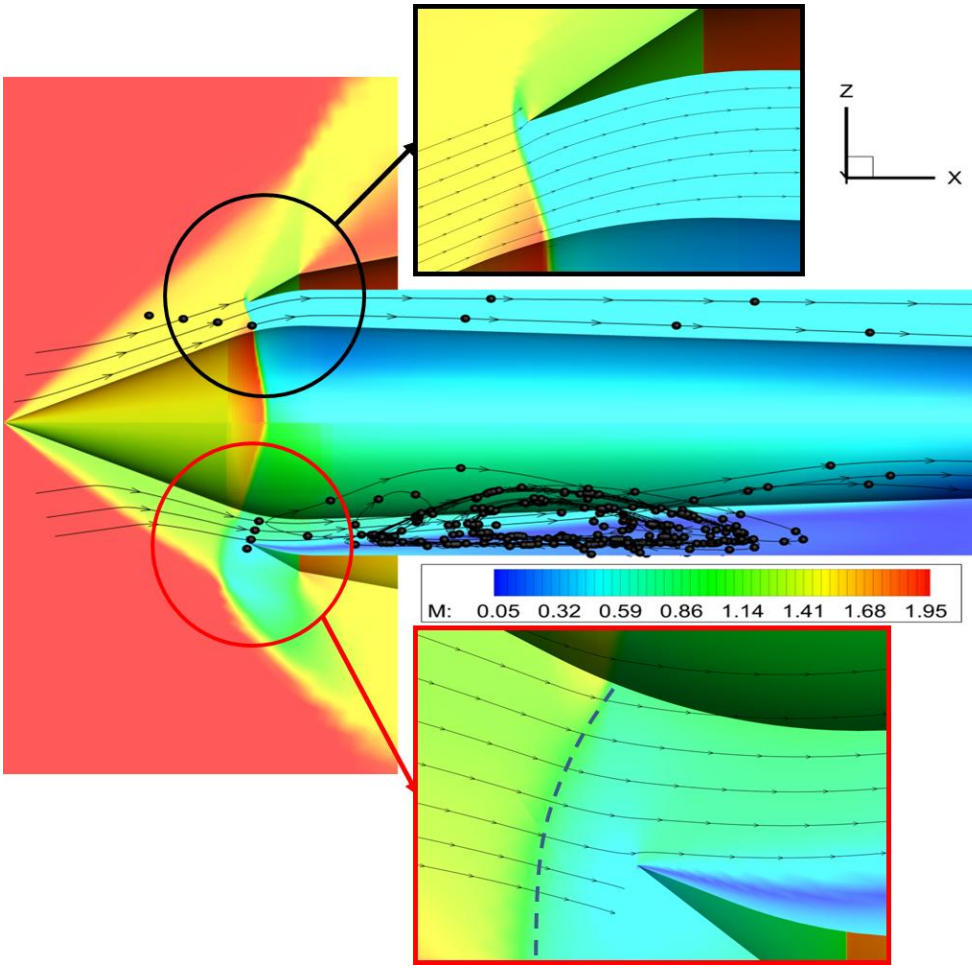

Fig. 38 Mach contour and stream line at the T7 frame in Fig. 9 (Mach 2.0, T.R=0, AOA=10°).

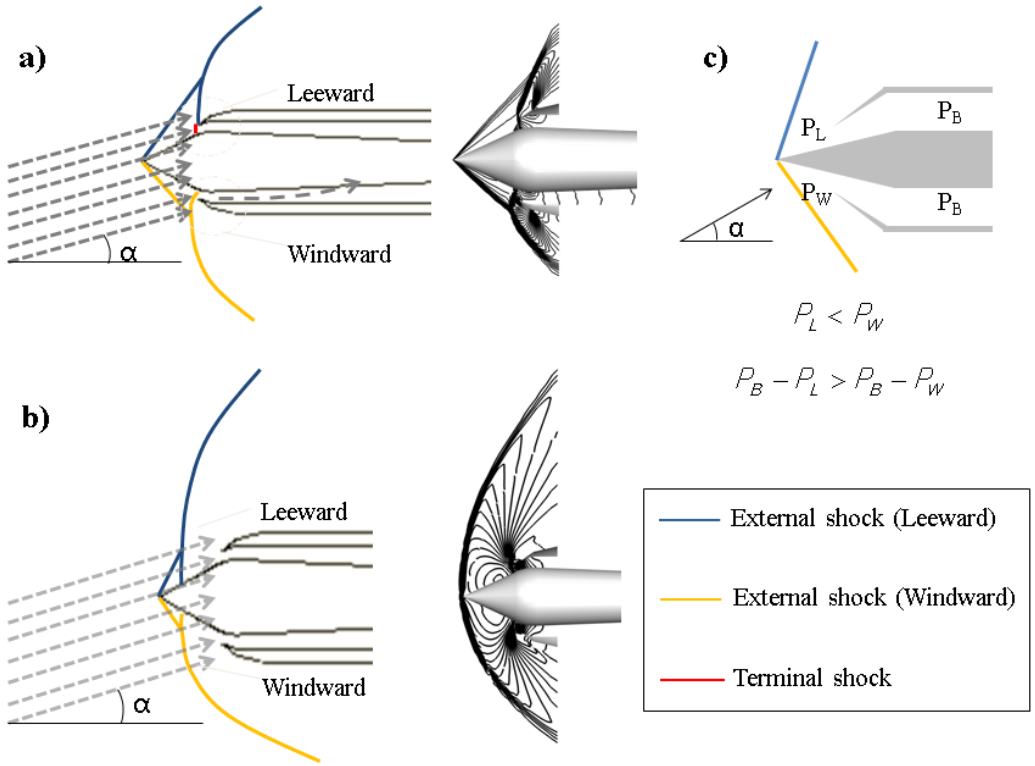

Fig. 39 Schema of asymmetric flow characteristics with attack angled flow and iso-pressure line contour (a: nearest critical condition in Fig. 9 T7, b: subcritical condition with upstream limit shock in Fig. 9 T4).

Furthermore, bow shock (dashed line in Fig. 38) occurs at the windward side, and a slip line is generated from the cowl lip (dashed curve arrow line in Fig. 39a). Because of the windward bow shock, the direction of the flow stream is changed not to align with the inner cowl surface. For this reason, local effect of windward cowl lip on inflow, there is a large difference in the velocity between the mainstream and the flow near the inner cowl surface; however, there is very little pressure gradient across this slip line, which is one of the sources of distortion, although one experiment reported that flow separation occurred at the windward cowl lip [29].

During the shock retreat process from T5 to T8, pressure on the leeward side is higher than the windward side at P3 because the pressure discontinuity surface leans upstream at the leeward side as depicted in Fig. 36 T6, T7 frames. This shock-leaning behavior becomes more visible as the throttling ratio increases (see Fig. 40 T6, T7). Generally, in an attack angled flow field, the effective angle of incidence increases at the windward compression side but decreases at the other side. The leeward oblique shock strength, therefore, is weaker than the no attack angled case, and the pressure rise is not noticeable after the oblique shock. In Fig. 38, because back pressure is relatively much higher than the pressure after the oblique shock at the leeward side, the shock is eventually pushed out of the inlet. Two time frames for the non-zero angle of attack case are depicted schematically in Fig. 39.

The frame in Figure 38 (T7) is simplified in Fig. 39a. At this moment, the leeward terminal shock moves to a more upstream position from the zero angle of attack case (Fig. 37) because of a weaker leeward oblique shock. Meanwhile, in the windward side, a stronger oblique shock was expected to create the supercritical condition with the terminal shock residing inside. However, a bow shock is generated in front of the cowl lip because of the increased bluntness of the windward cowl lip developed in the cowl lip because the bow shock makes the windward inflow direction curved as shown in Fig. 38. Figure 39-(b) shows that when the shock is pushed out to the upstream limit in Fig. 36, T4. The shock angle depends on three conditions: free-stream Mach number, compression surface angle, and back pressure. As shown in Fig. 39b, the after-shock pressure on the leeward side is lower than the windward side even when the back pressure is equal and high on both sides. As a result, the back pressure on the leeward side expels the leeward shock more strongly, and

thus the leeward bow shock angle is larger than the windward side in the subcritical condition. During the process of Figs. 39a and b, the inlet captured area keeps being asymmetric and varies in a pressure oscillation cycle. As a result, this transient behavior makes the dynamic distortion of the total pressure at the inlet cross section.

When the throttling ratio is increased, shock movement at the windward and leeward sides is even more desynchronized with each other compared to the zero throttle-area case. As shown in Fig. 40, during shock forwarding (T1~T4), process, shock positions at the windward and leeward side have more different features from the previous case (Fig. 36). Also, Fig. 40 shows that windward pressure at the P1 sensor increases before T2, which is earlier than the zero throttle-area case.

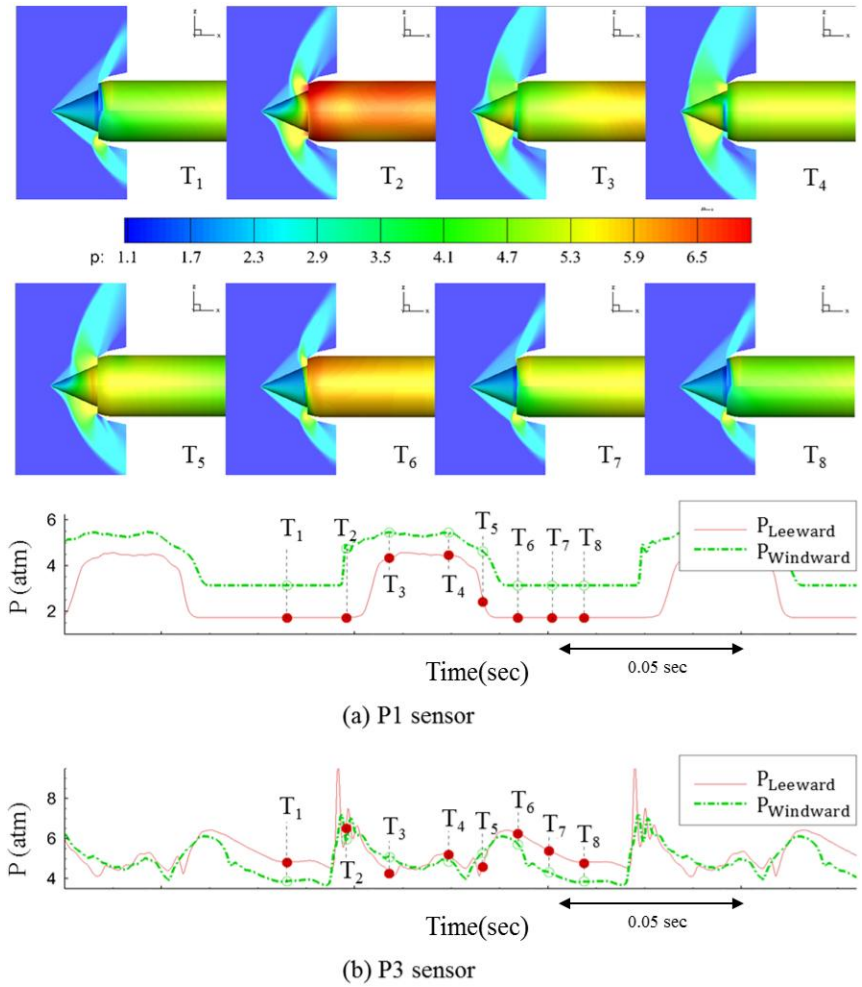

Fig. 40 Pressure oscillation sequence in the pressure oscillation cycle and pressure history at P1 and P3 sensors of wind/leeward side (Mach 2.0, T.R=0.35, AOA=10°).

As mentioned earlier, a bow shock is located in front of the windward cowl, and there is always some open space between the shock and the cowl lip. It is easier, therefore, to push flow upstream, and reversing flow has room to escape. It makes the windward shock move upstream earlier. The leeward side, on the other hand, requires higher back pressure for a transition to subcritical because

the shock at the cowl lip should be pushed away first. Only then, can the flow be emitted out of the inlet. Because pressure rises slower as the throttling ratio increases, the leeward side shows slower transition to the subcritical state, which results in even more severe desynchronizing with the other side.

5.4 Angle of Attack Effects on Inlet Pressure Oscillation

5.4.1 Pressure oscillation transition from small to big amplitude

Summarizing the computational results reveals that the angle of attack does not affect the pressure oscillation frequency, but it does affects the amplitude of pressure fluctuation.

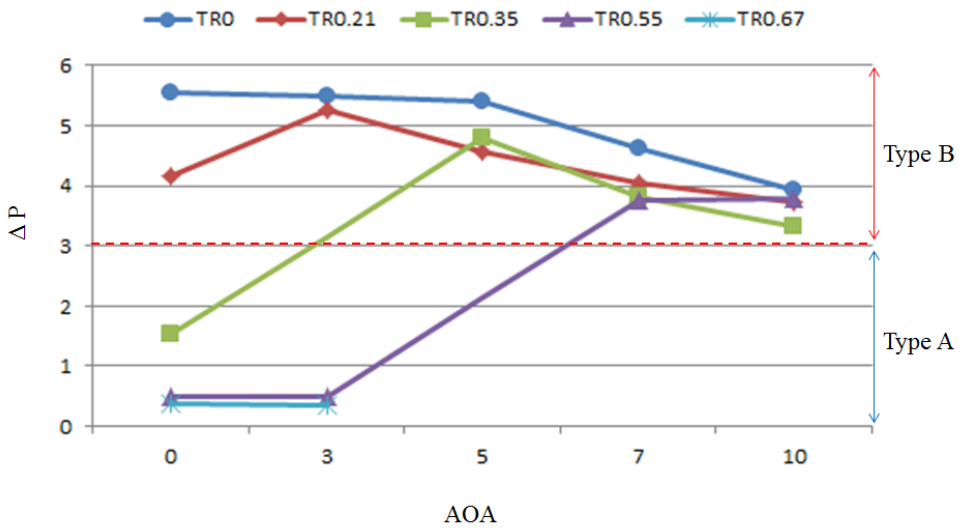

Fig. 41 Magnitude variations of pressure oscillation along the attack angle at each throttling ratio (at P3 sensor).

Figure 41 shows the pressure differences between maximum and minimum pressure in a pressure oscillation cycle at P3 sensor. Interestingly, these pressure difference values are classified in two groups: big and small amplitudes. In this research, they are simply called Type A oscillation (small amplitude) and Type B oscillation (big amplitude). At throttling ratio 0 and 0.21, the pressure oscillates in the big amplitude at all the angles of attack. The amplitude line of T.R = 0.35 in Fig. 41, abruptly rises between at 3˚ and 5˚of incidence angle. In this figure, the amplitude point is at 3˚ of incidence angle, and the 0.35 of throttling ratio is not indicated because it shows irregular amplitude or transition from small to big amplitude. Because the amplitude at the transition point shows random behavior, all the transition amplitude in not indicated in the other throttling ratios. As the throttling ratio increases, the transition angle of attack is larger. Table 12 indicates the domain of type A , B, and transition.

Table 12. Classification of pressure oscillating pattern.

		T.R					
		0	0.21	0.35	0.55	0.67	0.79
AOA	0˚	**Big (B)**	**Big (B)**	Small(A)	Small(A)	Small(A)	-
	3 ˚	**Big (B)**	**Big (B)**	T	Small(A)	Small(A)	-
	5 ˚	**Big (B)**	**Big (B)**	**Big (B)**	T	T	-
	7 ˚	**Big (B)**	**Big (B)**	**Big (B)**	**Big (B)**	T	T
	10 ˚	**Big (B)**	**Big (B)**	**Big (B)**	**Big (B)**	T	T

Table 12 shows some the tendency of the pressure oscillation type distribution. As the throttling ratio or angle of attack increases, the pressure oscillation has big amplitude and, on the contrary, it has small amplitude at small throttling ratio and angle of attack. In the field of throttling ratio, the attack angle

combination matrix transition points a cut the domain diagonally. From the formation of this table, it is easily predicted that there is an extra transition point between T.R = 0.21 and T.R = 0.35. Especially at T.R = 0.79, the transition pressure oscillation comes up by increasing the angle of attack from a steady state in initial at small attack angle. Figure 42 present a detail of pressure history. The histories at the left are the column of throttling ratios sweep at 3˚of the attack angle, and the columns on the right are the row of attack angles sweep at T.R = 0.35. As the throttle ratio decreases from 0.67 to 0 with 3˚ of attack angle, the amplitude of pressure oscillation increases. On the other hand, as the attack angle increases with throttling ratio 0.35, the amplitude increases also. In both series, there is irregular pressure oscillating case, as shown in Fig. 42, when the throttling ratio is 0.35 and attack angle is 3˚. This condition is a transition point. By passing this temporal, irregular, transitional process the pressure oscillation is much amplified, and after crossing this point, it has a stronger magnitude with a further oscillatory pattern. Therefore, the cases could be classified in three groups: small amplitude oscillation group (A), big amplified oscillation group (B), and transition group (T) as shown in Fig. 42.

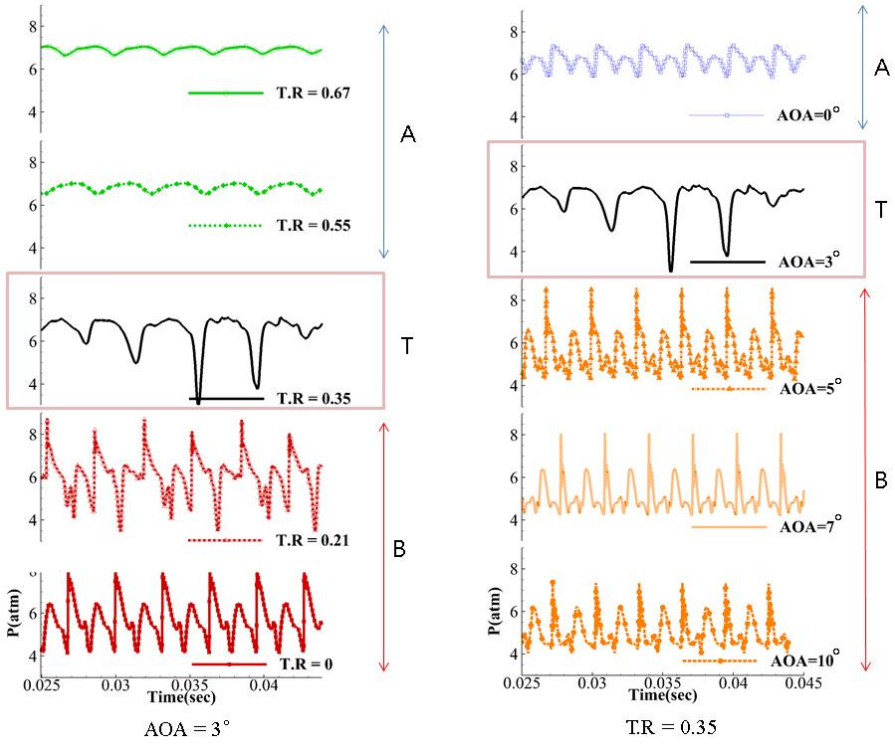

Fig. 42 Pressure history curves at P3 at various throttling ratio with constant angle of attack (left) and at various angle of attack with constant throttling ratio (right).

Figure 43 shows how up and down stream limits of shock travels in a pressure oscillation cycle. As the throttling ratio decreases, the upstream limit moves forward while the downstream limit moves backward; therefore, the shock travel range widens. It is noticeable that the terminal shock enters an inlet internal at two cases of throttling ratios, 0.0 and 0.21. These two throttling ratios at the zero angle of attack belong to the type B oscillation criteria. Extending this coincidence to the other angles of attack cases, it shows that the oscillation of type B arises when the terminal shock enters inlet internal. This coincidence

implies that transition of pressure oscillation has a strong relation with shock moving in and out of the inlet.

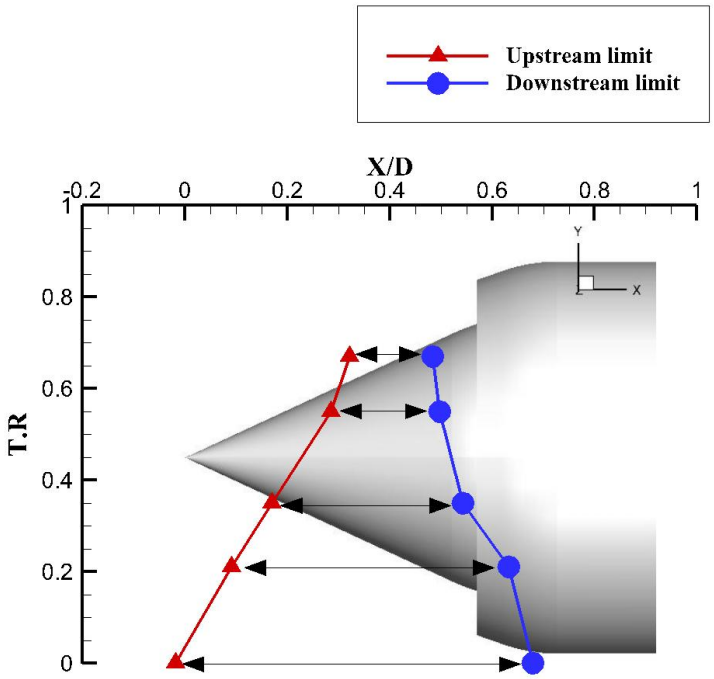

Fig. 43 Up and downstream limits of shock travel under various throttling ratio (inviscid, M = 2.0, AOA=0˚)

By this shock moving in and out, the rate of captured ratio changing, entering mass flow rate, and shock instability are increased. With the angle of attack condition, the terminal shock is generated in front of at both of windward and leeward sides. It means that the super-critical condition is changed to sub-critical condition by the attack angle so that the shock becomes more unstable; thus, the terminal shock moving in and out of the inlet is one of the oscillation transition triggers. At the transition point, the terminal shock enters the internal

inlet intermittently because it doesn't have enough momentum to swing full in and outside of the inlet. So far, the simulation results show that the pressure oscillation could be amplified by a shock entering condition.

5.4.2 Dynamic Distortion

In general, a ramjet with an angle of attack has an internal distortion problem in which pressure distribution reaction amount are significantly irregular. This irregularity becomes severe as the angle of attack increases. In particular, the inlet pressure oscillation with an angle of attack incurs dynamic distortion. The distortion coefficient (DC) is defined as follows [31]:

$$DC = \frac{\max P_t - \min P_t}{\overline{P}_t}, \tag{5.1}$$

($\overline{P}_t$: averaged total pressure, P_t : maxim or minimum total pressure at the cross section)

Time indices in Fig. 44 are from Fig. 36, and the DC is written in percent units in the figure. DC is higher during the back pressure recovery stage (T1, T2, T6, and T8). During these times, the terminal shock remains near the cowl lip, and the throat section is exposed to a high Mach number and low pressure flow. Asymmetric resources, such as a slip line from the windward cowl lip in Fig. 38 ,and reversed flow desynchronizing strongly affect distortion. Figure 45a shows the time averaged distortion coefficient for different throttling ratios. It appears that the throttling ratio does not affect the distortion much; however, the angle of attack is found to influence the distortion significantly. As is shown in Fig. 45-(b), the DC increases nearly in proportional to the attack angle. Although

the averaged distortion coefficient is less than 0.1, the instantaneous peak is about 0.2, 3 to 7 times higher than the averaged DC.

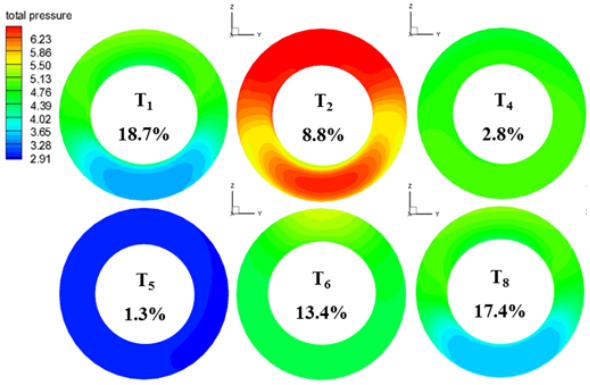

(a) Total pressure distribution

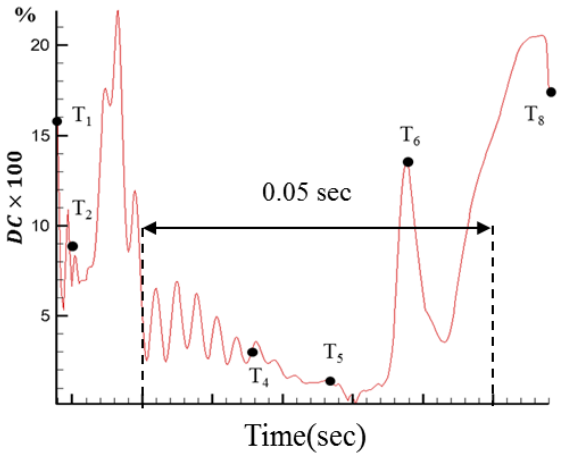

(b) Distortion history at P4

Fig. 44 Total pressure distribution and distortion history at P4 (Mach 2.0, T.R=0, AOA=10°)

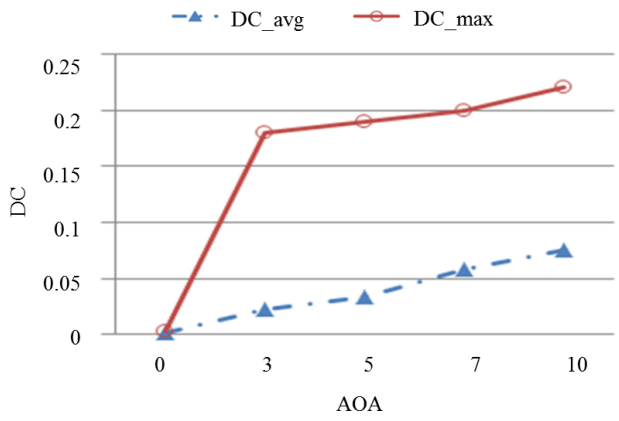

(a) Distortion coefficient variation

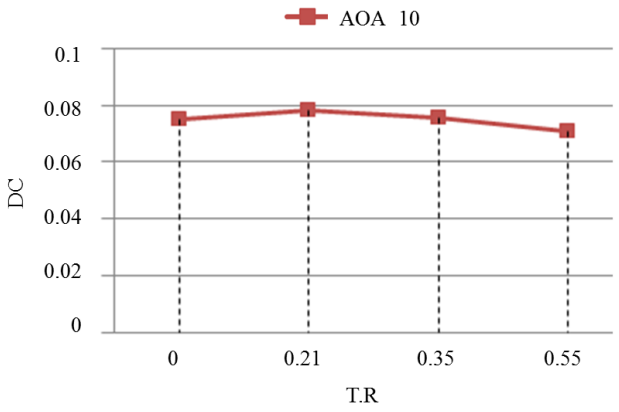

(b) Averaged distortion variation

Fig. 45 Averaged and maximum distortion coefficient variation along the attack angle (left, Mach 2.0, T.R=0) and averaged distortion along the throttling ratio (right, Mach 2.0, AOA=10°)

Chapter VI
Concluding Remarks

In this dissertation, two primary topics were discussed: the hysteresis of inlet buzz with mass flow control and the effect of angle of attack on inlet buzz.

The present computational study aims to understand the two different buzz transition characteristics that were partially observed at previous experimental studies [2, 4]. One is to examine the inlet buzz behavior under varying mass flow conditions, and the other is to explain the hysteresis characteristic of the inlet buzz. To realize the objective, three cases of computations are conducted. For Case 1 with the inlet geometry without center body, grid refinement and time step sensitivity tests are conducted. The computed dominant frequency agrees well with the experimental result. Because the center body is not included in Case 1, the shock-induced vortex does not appear in the inlet front, and the dominant frequency is relatively low, which is mode 1 (100~150Hz).

For Case 2 with the full geometry, including center body, the shock-induced vortices appear and decay more frequently as the mass flow rate decreases, which leads to the buzz of mode 2. The sudden buzz transition from the mode 1 of low frequency (100~150Hz) to the mode 2 of medium frequency (350~400Hz), observed in Nagashima's experiment [4], was successfully reproduced in this computational study. The overall qualitative tendency of the inlet buzz and the quantitative results at most of mass flow conditions agree with the experimental data. At the beginning of the increasing mass flow rate, another buzz transition from the mode 2 of medium frequency (350~400Hz) to

the mode 3 of high frequency (600~700Hz), which was briefly reported by Dailey's experiment [2], was also captured by the simulation of Case 3. In spite of the increasing mass flow rate, the high buzz frequency in mode 3 is maintained until the throttling ratio reaches a high mass flow rate condition of T.R = 0.97~1.14. If the mass flow rate increases further, the dominant buzz frequency drops from the mode 3 to the mode 1. As a result, the buzz frequency and the total pressure recovery of Case 3 under the increasing mass flow rate from T.R = 0.0 to 2.41 are quite different from those of Case 2 under the decreasing mass flow rate from T.R = 2.41 to 0.0.

In other words, the computational study shows the hysteretic buzz behavior dependent on the mass flow rate change with three kinds of buzz transitions. Furthermore, four different vortices – throat vortex, inner cowl vortex, compression surface vortex, and outer cowl vortex – induced from the shock-boundary layer interaction play a significant role in promoting and maintaining the buzz resonance by providing acoustic disturbances, like an edge tone in musical instruments. Based on the similarities observed between the hysteretic inlet buzz behavior and the sound generation mechanism of musical instruments, it is explained that the inlet buzz transition can be regarded as a kind of overblowing phenomenon triggered by shock-induced vortices, and the interaction between the shock-induced vortices and the inlet diffuser results in the hysteretic behavior.

In the second part of this study, inviscid computations were conducted to reduce computational resources and time cost. The inlet pressure oscillation to mimic inlet buzz was numerically simulated with controlling the throttling ratio from 0 to 0.67 and the angle of attack from 0° to 10°. When there is no angle of attack, the inviscid simulation predicted a dominant frequency as the

fundamental mode of frequency, while lower than the viscous simulation and experimental result shows the 3rd mode of the frequency estimated from Eq. 4.4. The asymmetric shock structure and flow physics appear when the angle of attack exists. Because of a weaker shock strength, back pressure pushes leeward the terminal shock to a more upstream location. In the windward side, a bow shock appears in front of the windward cowl caused by the increased bluntness of the cowl lip. Because the stream line is curved by the bow shock, a slip line is generated from the windward cowl lip. Furthermore, the moment of reversed emission at the windward and leeward sides is desynchronized as the throttle ratio increases.

These asymmetric physics at the angle of attack condition dominantly affect distortion. For this reason, the angle of attack is the determinant in regards to distortion while the throttling ratio is a minor element. The pressure oscillation initiation and transition are generated by decreasing the throttling ratio or increasing the attack angle process. In this process, external shock enters the internal inlet so that shock instability is increased, and the captured ratio changed discretely. It is the main source of amplifying the pressure oscillation amplitude. It seems that if the viscous effect intervenes, initiation and transition of pressure oscillation are triggered earlier because of shock-shock interaction and shock - boundary layer interaction.

Although the present result shows some quantitative difference from the experimental data, it reasonably predicts the effect of the angle of attack on the pressure oscillating frequency, shock structure and distortion coefficient. This information allows us to understand the fundamental aerodynamic characteristics, such as pressure oscillation behavior and inlet performance, of target geometry

within a limited range of angle of attack. Moreover, the computed results can be used for preliminary design and identifying a feasible range of inlet operations.

6.1 Future Works

Base on the present observation and analyzing, effort is in progress to investigate as follows:

To examine the effect of four vortices on the inlet buzz in detail

To check on the four vortices roles on inlet buzz and determine if it requires more number of sensors. By installing more sensors at the locations where the vortices are generated, sufficient data will be given to explain the contribution of the vortices to the inlet buzz frequencies and the transitions.

To examine the effect of throttling ratio changing speed

To check up the effect of throttling ratio changing speed, the speed will be controlled higher or lower than the present research. The examination will show a tendency of inlet buzz character according to the throttling speed.

Fluid-Structure interaction(FSI) analysis on supersonic inlet

To investigate the inlet buzz effect on the inlet structure. It requires FSI analysis between pressure fluctuation and the inlet structures such as the cowl and the center body.

Three-dimensional turbulent computation for angle of attack condition

To investigate the effects of shock boundary interaction on asymmetric characteristics during inlet buzz. It is required to simulate three-dimensional turbulent flow for supersonic inlet at angle of attack condition.

References

[1] Oswatitsch, K., "Pressure Recovery in Missiles with Reaction Propulsion at High Supersonic Speeds (the Efficiency of Shock Diffusers)," NACA TM-1140, 1947.

[2] Dailey, C.L., "Supersonic Diffuser Instability," *Journal of the Aeronautical Sciences*, Vol. 22, No. 11, 1955, pp. 733, 749.

[3] Ferri, A., and Nucci, R. M., "The Origin of Aerodynamic Instability of Supersonic Inlets at Subcritical Conditions," NACA RM-L50K30, Jan. 1951.

[4] Nagashima, T., Obokata, T., and Asanuma, T., "Experimental of Supersonic Air Intake 0," Institute of Space and Aeronautical Science of Tokyo, JAPAN, Rept. 481, May 1972.

[5] Newsome, R. W., "Numerical Simulation of Near-Critical and Unsteady, Subcritical Inlet Flow," *AIAA Journal*, Vol. 22, No. 10, 1984, pp. 1375, 1379.

[6] Lu, P., and Jain, L., "Numerical Investigation of Inlet Buzz Flow," *Journal of Propulsion and Power*, Vol. 14, No. 1, 1998, pp. 90, 100.

[7] Hankey, W.L., Shang, J.S., "Analysis of Self-Excited Oscillations in Fluid Flows," AIAA 13th Fluid&Plasma Dynamics conference, Snowmass, Colorado, 1980.

[8] Trapier, S., Deck, S., and Duveau, P., "Detached-Eddy Simulation and Analysis of Supersonic Inlet Buzz," *AIAA Journal*, Vol. 46, No. 1, 2008, pp. 118, 131.

[9] Hall, D. E., *Musical Acoustics*, 2nd ed., Brooks/Cole Publishing Company, California, 1991, Ch. 12, 13

[10] Benade, H., *Fudamentals of Musical Acoustics*, 2nd ed., Dover Publications, New York, 1990, Ch. 22

[11] Askill, J., Physics of Musical Sound, 1st ed., D. Van Nostrand Co., 1979, p.121

[12] Coltman, J.W., "Jet Drive Mechanisms in Edge Tones and Organs Pipes", Journal of the Acoustical Society of America, Vol.60, 1976, pp725-733.

[13] Kim, K. H., Kim, C., and Rho, O. H., "Methods for the Accurate Computations of Hypersonic Flows, Part 1: AUSMPW+ Scheme," *Journal of Computational Physics*, Vol. 174, No. 1, 2001, pp. 38, 80.

[14] Van Leer, B., "Towards the Ultimate Conservative Difference Scheme. V. A Second Order Sequel to Godunov's Methods," *Journal of Computational Physics*, Vol. 32, No. 1, 1979, pp. 101,136.

[15] Yoon, S., and Jameson, A., "Lowe-Upper Symmetric-Gauss-Seidel Method for the Euler and Navier-Stokes Equations," *AIAA Journal*, Vol. 26, No. 9, 1988, pp. 1026,1026.

[16] Menter, F. R., "Two-Equation Eddy-Viscosity Turbulence Model for Engineering Applications," *AIAA Journal*, Vol. 32, No. 8, 1994, pp. 1598, 1605.

[17] Biedron, R. T., and Thomas J. L., "A Generalized Patched-Grid Algorithm with Application to the F-18 Forebody with actuated control strake," Computing System in Engineering, Vol. 1, No. 4, 1990, pp 563-576

[18] Chima, R.V., "Analysis of Buzz in a Supersonic Inlet", NASA TM-217612, 2012

[19] Harner, K.I. and Patrik, J.P., "Control System Requirements for Advanced Ramjet Engines," AIAA/SAE 14th Joint Propulsion Conference, Las Vegas, Nev., 1978, AIAA, 12P.

[20] Bendot J. C., Heins Jr., A. E. and Piercy, T. G., "Ramjet Air Induction system design for Tactical Missile Application," AGARD Lecture Series No. 136, 1984.

[21] Orlin W. J. and Dunsworth, L. C., "A Criteria for Flow Instability in Supersonic Diffuser Inlets," Marquardt Report No. 5144, 1951.

[22] Cummings, R. M., Morton, A.M. and McDaniel D.R., "Experiences in accurately predicting time-dependent flows," *Progress in Aerospace Science*, Vol.44, 2008, pp241-257.

[23] Tan, H., Sun, S. and Yin, Z., "Oscillatory Flows of Rectangular Hypersonic Inlet

Unstart Caused by Downstream Mass-Flow Chocking," *Journal of Propulsion and Power*, Vol.25, 2009, pp138-147.

[24] Park, I.S., Ananthkrishnan, N., Tahk, M.J., Vineeth, C.R. and Gupta, N.K., "Low-Order Model for Buzz Oscillations in the Intake of a Ramjet Engine," *Journal of Propulsion and Power*, Vol.27, No.2, 2011, pp503-506.

[25] Hong, W. and Kim, C., "Numerical Study on Supersonic Inlet Buzz under Various Throttling Condition and Fluid-Structure interaction," 29th AIAA applied Aerodynamics Conference, Honolulu, Hawaii, 2011.

[26] Kwak, J.Y., Hong, W., Shin, S. J., Lee, I., Yi, J.S., and Kim, C., "Transient Time Aero-elastic Analysis of a Supersonic Flight Vehicle with a Ramjet Engine," AIAA Fluid Dynamics and Co-located Conference and Exhibit, New Orleans, Louisiana, U.S., 2012.

[27] Howe, M.S., "Contributions to the theory of aerodynamic sound, with application to excess jet noise and the theory of the flute," Journal of Fluid Mechanics, Vol. 71, part 4, 1975, pp.625-673.

[28] Colonius, T., Lele, K.S. and Moin, P., "The scattering of sound waves by a vortex: numerical simulations and analytical solutions," Journal of Fluid Mechanics, Vol.260, 1994, pp.271-298.

[29] Goldsmith, E.L., "Some Aspects of Engine and Airframe Integration for Ramjet and Ramrocket powered Missiles," Ramjet and Ramrocket Propulsion System for Missiles, *AGARD* Lecture Series No.136, 1984, ISBN 92-835-0360-0

[30] Connors, J.F., "Some Aspects of Supersonic Inlet Stability," *NACA* RM-E55L16a, 1956.

[31] Schueller., C.F. and Stitt, L.E., "An Inlet Design Concept to Reduce Flow Distortion at Angle of Attack," *NACA* RM-E56K28b, 1957

[32] Hong, W. and Kim, C., "Numerical Study on Supersonic Inlet Buzz under Various

Throttling Condition and Fluid-Structure Interaction," 29th *AIAA* applied Aerodynamics Conference 27-30 June 2011, Honolulu, Hawaii

[33] Soltani, M.R., Farahani, M. and Asgri Kaji, M.H., "An Experimental Study of Buzz Instability in an Axisymmetric Supersonic Inlet," *Scientia Iranica B,* Vol. 18(2), 2011, pp. 241-249.

[34] Soltani, M.R., Farahani, M., "Effects of Angle of Attack on the Inlet Buzz," Journal of Propulsion and Power, Vol.28, No.4, 2012, pp. 747-757.

[35] Lee, H.J. and Jeung, I.S., "Experimental and Numerical Investigation on the Supersonic Inlet Buzz with Angle of Attack," *Shock Waves*, Part XVI, 1111-1116, 2009, DOI: 10.1007/978-3-540-85181-3_51

[36] Kopal, Zdenek., "Tables of Supersonic Flow Around Cones of Large Yaw," Massachusetts Institute of Technology, Technical report No.5, 1949.

[37] Wilcox, D. C., "Turbulence Modeling for CFD," DCW Industries, Inc., 5354 Palm Drive, La Canada, CA, 1993, pp. 73-17.

[38] Wilcox, D. C., "Formulation of the k-omega Turbulence Model Revisited," *AIAA Journal*, Vol. 46, No. 11, 2008, pp. 2823-2838.

[39] Menter, F. R., Kuntz, M., and Langtry, R., "Ten Years of Industrial Experience with the SST Turbulence Model," *Turbulence, Heat and Mass Transfer 4*, 2003, pp. 625-632.

[40] Roe, P. L., "Approximate Riemann Solver, Parameter Vectors, and Difference Schemes," *Journal of Computational Physics*, Vol. 43, 1981, pp. 357-372.

[41] Kim, S., Kim, C., and Rho, O.-H., and Hong, S. K., "Cures for the Shock Instability: Development of a Shock-Stable Roe Scheme," *Journal of Computational Physics*, Vol. 185, No. 2, 2003, pp. 342-374.

[42] Kim, K. H., and Kim, C., "Accurate, Efficient and Monotonic Numerical Methods for Multi-Dimensional Compressible Flows. Part II: Multi-Dimensional Limiting Process," *Journal of Computational Physics*, Vol. 208, No. 2, 2005, pp. 570-615.

국문초록

본 논문은 흡입구 버즈라고 불리는 초음속 흡입구 주위의 공력불안정성에 대해 수치적 연구로 접근한 내용을 다루고 있다. 이미 알려진 바와 같이 유동조건이 점진적으로 변하더라도 흡입구 버즈는 불연속 적이고 이력적(hysteretic)인 특성을 보인다. 흡입구 버즈의 불연속 적이고 이력적 특성을 해석하기 위해 유량조건과 받음각 조건을 변화시켜가며 수치해석을 수행하였다. 유량조건은 출구부분에 위치한 플러그를 전진 혹은 후퇴 시켜가며 출구면적을 조절함으로서 제어하였다. 또 받음각 효과를 알아보기 위한 수치실험의 경우 3차원 비점성가정의 계산을 수행하였다.

먼저 유량조건을 조절한 수치실험을 수행하였는데 여기에서는 유량에 따른 흡입구 버즈의 이력특성을 관찰하는데 초점을 두었다. 흡입구 유량을 감소시키는 계산을 먼저 수행하였고 이 과정에서 1차 모드의 낮은 진동수가 2차 모드의 보다 높은 진동수로 천이되는 것이 관찰되었다. 그 다음으로 출구가 막힌 흡입구에서부터 조금씩 유량을 조금씩 증가시키는 동안 흡입구 버즈 거동을 관찰하였다. 이 경우 입출구비가 확장되는 순간부터 2차에서 3차 모드의 더 높은 진동수로의 천이가 한 번 더 발생하였고 이 경우 앞선 출구유량을 감소시키는 실험과 동일한 유량조건이 되는 순간에도 그때와 다른 진동수를 가지는 것을 확인하였다. 이와 같은 현상은 스스로 진동이 증폭되는 메커니즘(self-excited mechanism)과 오버블로윙(over-blowing)과 같은 파이프 형태의 악기가 소리를 내는 음향학적 원리와 유사점을 공유한다. 이러한 유사성을 염두하면서 음향학적인 측면에서 흡입구 버즈의 이력특성을 설명하였다.

그 다음으로 3차원 비점성 유동 해석을 통해 흡입구 압력진동 현상에 대한 받음각 효과를 알아보았다. 비점성 상태에서의 압력진동의 패턴과

흡입구 안팎의 유동분포가 실제 실험과 정성적인 유사성을 가지고 있는 부분에 초점을 맞췄다. 받음각은 압력진동의 패턴과 유동뒤틀림(distortion) 및 충격파의 비대칭적인 분포를 발생시키고 심화시켰으나 기존 압력진동의 진동수를 변화시키지는 않았다. 그러나 받음각이 없거나 작은 정상상태 흡입구에 전방유동의 받음각이 증가하게 되면 새로운 유동진동이 발생하였다.

주요어: 전산유체역학, 흡입구 버즈, 충격파 불안정성, 이력특성(hysteresis), 입출구비, 받음각, 천이

학 번: 2007-30127

이 름: 홍 우 람